Extreme ultraviolet high harmonic generation and spectroscopy in solids

Tran Trung Luu

München 2015

Extreme ultraviolet high harmonic generation and spectroscopy in solids

Tran Trung Luu

Dissertation
an der Fakultät für Physik
der Ludwig–Maximilians–Universität
München

vorgelegt von
Tran Trung Luu
aus Thai Binh, Vietnam

München, den 18.03.2015

Erstgutachter: Prof. Dr. Ferenc Krausz
Zweitgutachter: Prof. Dr. Joachim Burgdörfer
Tag der mündlichen Prüfung: 27.04.2015

Dedicated to my wife Hong Hoa and my son Duc Minh

Zusammenfassung

Die Manipulation der Dynamik von Elektronen im Mikrokosmos setzt die präzise Erzeugung von elektromagnetischen Feldern voraus. Dies wurde vor kurzem durch die Lichtfeld-Synthese ermöglicht.

In meiner Doktorarbeit demonstriere ich erstmals die Erzeugung von kohärenter hochharmonischer Strahlung im extem ultravioletten Spektralbereich mit Photonenergien von bis zu $\sim$ 40 eV durch die Interaktion von ultrakurzen elektrischen Feldern mit dünnen SiO_2-Schichten.

Die Analyse der Wechselwirkung mit intensitäts-und schwingungsverlaufsgeregelten elektrischen Feldern gibt einen detaillierten Einblick in die Physik hinter der Emission und ermöglicht es die erzeugte Strahlung mit elektrischen multi-Petahertz Strömen in Beziehung zu setzen, welche im SiO_2-Kristall durch das ultraschnelle treibende Feld des erzeugenden Laserpulses induziert werden. Desweiteren wurde hierdurch die erste Sondierung der feinen Details des Energie-Dispersions Profils des Leitungsbands eines Nichtleiters ermöglicht, welche bisher durch Standardelektronspektroskopie nicht zugänglich waren. In dieser Arbeit werden weiterhin die ersten Schritte zur Erforschung des neuen Gebiets der Festkörperphotonik im extem ultravioletten Spektralbereich getan.

Diese Doktorarbeit beschreibt auch wie optische Attosekundenpulse neue Möglichkeiten zur Kontrolle gebundener Elektronen auf sub-fs Zeitskalen, über das "Strong Field Ionization Regime" hinaus bietet.

Durch die Messung der Vakuumultravioletstrahlung von elektrischen, präzise einstellbaren Feldern ausgesetzten Krypton Atomen zeige ich Zugang zur nichtinstantenen, nichtlinearen, elektrischen Erregungsantwort von gebundenen Elektronen.

Zusätzlich zur Untersuchung der feldgetriebenen Elektronendynamik in Materie widmet sich ein Teil dieser Doktorarbeit dem Design und der Umsetzung einer neuen Generation von Lichtfeld-Sythesizern welche die Lichtfeld-Synthese auf Terawatt Leistungsniveau ermöglichen sollen.

Abstract

Manipulating electron dynamics in the microcosm requires precisely engineered electromagnetic fields. Such fields have been recently brought to life by virtue of light field synthesis.

I demonstrate in this thesis that the interaction of ultrashort electric fields with thin films of SiO_2 enables the generation of coherent high order harmonic radiation in the extreme ultraviolet ranging up to ~ 40 eV for the first time.

Study of the interaction with intensity and waveform controlled electric fields provides detailed insight into the physics of the emission and allows relating the emitted radiation to multi-petahertz electronic currents induced in the bulk of SiO_2 by the ultrafast driving field. Moreover it allowed, for the first time, the probing of the fine details of the energy dispersion profile of the conduction band of an insulator, previously inaccessible by standard electron spectroscopies. This work also takes the first steps towards exploring the new area of solid-state photonics in the extreme ultraviolet region.

The thesis also details how optical attosecond pulses can now offer new capabilities for controlling bound electrons on sub-fs time scales, beyond the strong field ionization regime.

Recording the vacuum ultraviolet emission of Krypton atoms exposed to precisely tunable electric fields I demonstrate access into the non-instantaneous nonlinear electronic response of bound electrons.

In addition to investigating field driven electron dynamics in matter, part of the thesis is devoted to design and implementation of a new generation light field synthesizer apparatus aiming at the advancement of light field synthesis at the terawatt power level.

Contents

Introduction

A vast majority of physical phenomena are manifestation of electron dynamics in the microcosm. Because electromagnetic fields can apply forces to electrons they offer the potential to control their dynamics and therewith other physical processes that are ensuing the electronic excitation of matter. Therefore by using light fields, one can be actively involved in steering microscopic processes by manipulating the electromagnetic field acting on them. In turn, manipulation of the electromagnetic field requires knowledge of light-matter interactions, thus a complete control of electrons and related processes requires a complex combination of knowledge on both fundamental as well as technological aspects.

Linear interactions between light and matter are processes easily encountered in daily life. Phenomena as reflection, refraction, dispersion, absorption, diffraction are some of the most important ones. Understanding of linear interaction has been pursued since the beginning of human evolution to the foundation of the Snell-Descartes law and till today. Knowledge of linear interaction between light and matter is of utmost importance in modern technologies and sciences (for instance, development of sophisticated multilayer optics [1] and photonic devices).

In contrast, nonlinear optical interactions are not commonly observed because usually the intensity of conventional light sources is too weak and the light sources are not coherent. With the invention of the laser [2], intense coherent light bursts of radiation have opened the era of nonlinear optics [3] and control of matter. Rapid development of tools has allowed the possibility to following light matter interactions in real time.

During the last decades, by capitalizing on nonlinear interactions, it has been possible to generate extremely short laser pulses, reaching femtosecond time scale (1 fs = 10^{-15} seconds) and since last decade also the attosecond time scale [4]. Owing to the unique properties of these pulses such as high temporal and spatial resolution, they are extensively utilized for applications in ultrafast spectroscopy [5], laser-controlled chemistry [6], frequency metrology [7], optical communications [8], biomedical applications [9], material processing [10], etc. In physical sciences, ultrashort laser pulses are now serving as a basic tool in investigating ultrafast phenomena, opening a new era of femtosecond spectroscopy for which the field of ultrafast science has been awarded a Nobel prize.

Controlling and probing electrons have significantly benefited from generation of ultrashort laser pulses and their high time resolution. Yet ultrashort laser pulses are not the fastest. In fact, light field exhibits a much steeper gradient than that of the cycle-averaged quantity. By introducing controlled few cycle laser pulses, one can exert a controlled, variable force on the electrons on the electronic time scale (attoseconds). This signaled the new era of attosecond control and measurement [4].

Controlled electromagnetic forces, strong enough to trigger nonlinear interactions,

induce electronic motion which can give rise to coherent extreme ultraviolet pulses (EUV), a feat that can be attributed to modern attosecond science. Since the emitted pulses are precisely synchronized to the incident laser pulses, they can be used in pump-probe experiments, triggering and probing ultrafast dynamics. This marks a radically new scientific possibility which is referred to as *light wave electronics* [11].

With the advent of light wave electronics, electronic wavepackets in atoms molecules plasmas or solids can now be controlled with unprecedented resolution. By steering the electronic wavepacket [12] (i.e. through the means of strong field ionization [13]), one can control their *classical* trajectories such that their re-collision to parent ions enables one to harvest detailed information related to the electronic structure [14] and the resultant emitted light characteristics [15, 16].

All of above achievements have been possible by the use of high power few-cycle laser pulses [14–16]. In order to reach even higher temporal precision and control, the most direct way (not necessarily the most convenient) is to pursue shorter laser pulses in optical frequencies also. Shorter laser pulses implies control over a considerably broader spectral range and at the same time, superior spectral phase control. These scientific and technical challenges have been recently addressed and have recently lead to the generation of optical attosecond pulses [17].

EUV generation and spectroscopy

The nonlinear frequency conversion of light, based on intense nonlinear interactions of light and matter, has formed the basis for extending applications of modern photonics and spectroscopies to ranges of the electromagnetic spectrum that are typically inaccessible using conventional optical technologies. Researchers can now routinely use laser-driven, solid-state nonlinear devices to produce radiation in the terahertz (THz) [18], deep or vacuum ultraviolet ranges [19], harnessing a great range of practical applications or fundamental studies of laser-matter interactions; however, to reach coherent EUV and X-ray frequencies, researchers must rely on gas-phase media [12, 20–23] and surface plasmas [24–28].

The laser-based generation of coherent EUV radiation from the bulk of solids could open the way to the development of compact and potentially practical sources or devices by benefiting from the properties of light in this spectral range. Moreover, and equally importantly, such sources could be the basis for the extension of techniques of attosecond measurement and strong-field control, currently revolving around broadband gas-phase EUV emission [12, 14, 20, 29–32], into the condense phase. The laser-based generation of EUV radiation would also enable the advancement of nonlinear microscopy [33], for which the spatial resolution can benefit from the nanometer spectral range of the generated photons or the ultrafast duration sustainable in this spectral range [30, 34–39]. Advances of this type would be of particular importance for real-time measurement and control of electronic and structural dynamics in condensed phase systems with unprecedented resolution; however, in the absence of methods permitting the generation of coherent, broadband EUV radiation in the bulk of solids, these possibilities have remained elusive.

Predicted in studies of nonperturbative laser-matter interactions [40, 41], high har-

monic generation in bulk media was recently explored in crystalline semiconductors using mid-infrared [42] and THz [43] driver fields, yielding coherent radiation covering the visible, deep and vacuum ultraviolet parts of the electromagnetic spectrum. Although extension to the extreme ultraviolet frequencies is supported by theoretical predictions [41], it is experimentally constrained by material damage induced by intense laser drivers. Semiclassical models [44] extended to these spectral ranges [42, 45–48] or more sophisticated quantum mechanical treatments [43, 49] highlighted the role of intraband, laser-driven dynamics such as the acceleration and nonlinear scattering of carriers in the extreme-nonlinear response of solids and offered important first insights into the physical processes underlying these experiments.

Although the above efforts comprise essential steps towards nonperturbative, femtosecond controlled light sources, these efforts have not yet resulted in the broadband generation of coherent EUV radiation in the bulk of solids and its attosecond control, leaving this spectral and temporal regime beyond the reach of modern solid-state laser technologies and spectroscopies.

Bound electron control

The attosecond response of bound electrons to electromagnetic fields, which is implied by the energy (< 10 eV) required for a typical bound-state electronic excitation, represents a natural frontier for dynamic control of matter. Exploration of ultrafast control of bound electrons in the vicinity of this frontier requires electromagnetic fields with well defined characteristics: (i) the spectral response of the electrons is below the first ionization energies (there is no ionized electrons), this also means the order of the interaction has to be low; (ii) the incident electric fields have to be sufficiently intense to activate nonlinear responses but also weak enough not to cause ionization; (iii) the consequent nonlinear response has to be confined and be controllable within the attosecond time interval. Because they naturally fulfill (ii) and (iii), laser pulses generated at optical and nearby ranges have yielded spectacular examples of real-time measurements of femtosecond atomic-scale dynamics [6], nonlinear control of such dynamics [50, 51] and even photonics devices [52] that operate at femtosecond scales, but they have not yet attained attosecond manipulation of bound-state electrons or the concomitant phenomena.

Direct extension of optical, laser-based control of bound-electrons from the femtosecond to the attosecond domain requires synthesis of intense attosecond pulses that extend over several octaves in optical and nearby frequencies, but such pulses have hitherto remained beyond the reach of modern laser technologies until [17]. Coherent superpositions of discrete spectral bands that span the above spectral range have enabled synthesis of periodic, sub-fs-sculpted optical waveforms [53, 54] and thereby implementation of waveform-sensitive quantum control [55] schemes of ultrafast manipulation of microscopic process [56, 57]. However, their temporal resolution is constrained by the nanosecond-to-femtosecond temporal envelope that is associated with the constituent bands. Recent efforts in multi-octave synthesis based upon coherent supercontinuum sources have advanced the temporal confinement and control of isolated laser pulses into the single- and sub-cycle domains [58, 59], but they have not yet reached the attosecond frontier.

In the absence of attosecond optical lasers, attosecond science has capitalized on the extreme nonlinearity of strong fields [12, 13, 60], typically ionizing processes [13] driven by multi- or few-cycle pulses, to attain attosecond resolution and to demonstrate its basic concepts [61]. Waveform-tailored, intense, few-cycle pulses have been used to attain sub-femtosecond control [29] and measurement of electrons liberated by the field in the ionization continua of atoms or molecules in the gas phase and the conduction bands of solids [62] and the motion of electrons in atomic or molecular ions [14, 32, 58, 63–65]. Although these developments represent novel realms of electronic manipulation, they have failed to implement attosecond control under perturbative or at least non-ionizing regimes, which is required to extend attosecond science to a broad class of quantum systems, such as atoms, molecules or solids in their neutral state, where femtosecond science flourishes.

Attosecond extreme ultraviolet (EUV) pulses [30, 35–38, 66–68] that emerge in strong-field processes are ideal for probing sub-cycle dynamics repetitively induced by optical fields [58, 69, 70] over femtosecond ranges and for ultrafast attosecond triggering of electron dynamics [71–73], but their constrained waveform tunability, limited intensity, and high (> 15 eV) central photon energy prevent them from being established as generic tool for bound-state electron control of matter.

The thesis

In this thesis, my main contributions to proof-of-concept experiments in generation and spectroscopy of EUV in solids, attosecond control of bound electrons, and laser developments are described below:

- In this work, I have shown that thin films of SiO_2 exposed to intense, few-cycle to sub-cycle pulses give rise to wideband coherent EUV radiation extending in energy to ~ 40 eV. A systematic investigation of the semiclassical model, a quantum-mechanical model and their comparison to the experimental data is carried out. It reveals the close relation of the emitted EUV radiation to induced intraband currents of multi-petahertz (PHz) frequency in bandwidth, in the lowest conduction band of SiO_2. To demonstrate the applicability of high-harmonic spectroscopy to solids, we exploit the EUV spectra to gain access to fine details of the energy dispersion profile of the conduction band that are as of yet inaccessible by photoemission spectroscopy in wide-bandgap dielectrics. In addition, we use the EUV spectra to trace the attosecond control of the intraband electron motion induced by sub-cycle optical transients. The generation of broadband EUV radiation by driving the coherent nonlinear motion of electrons in solids not only advances high order harmonic spectroscopy to the condensed phase but also promotes solid-state laser photonics and electronics to a new frequency regime where they can find a great deal of practical applications.

- We have made it possible to generate sub-cycle laser pulses whose duration is less than one period of their carrier wave [58]. These pulses are still not short enough to provide attosecond confinement and control. Ultimately, by utilizing sophisticated spectral shaping together with the addition of the deep ultraviolet channel to the existing synthesizer and related advancements, attosecond confinement and

control of laser pulses have become real. Bound electrons have been controlled by unprecedented degree of freedom through manipulation of these optical attosecond pulses.

Furthermore, careful inspection of the vacuum ultraviolet spectra generated by the medium under influence of the optical attosecond pulses shows indication of the non-instantaneous optical response. By utilizing the numerical solution of a three dimensional time dependent Schrödinger equation [74] as a benchmarking tool, a great applicability of the developed models has been observed. Consequently, by applying the models to the experimental spectrograms, we have unambiguously showed that the reconstructed nonlinear polarization response is delayed with respect to the instantaneous nonlinear response.

This application demonstrates the power of attosecond steering and probing of electrons together with attosecond metrology [34]. Although our studies were limited to Krypton atoms under a simplified model, attosecond non-instantaneity in the optical response of bound electrons is to be explored in a broader range of bound electronic systems because of the vast similarities in their electronic structures.

- Lastly, I have worked on a next-generation synthesizer that aims at advancing optical attosecond pulse technology to the TW scale. Several technical advancements have been made to improve even further the state-of-the-art of the pulse synthesis. Highly efficient direct second harmonic generation ($> 50\%$ for ~ 23 fs incident pulses) which is very close to the theoretical limit calculated by nonlinear propagation has been demonstrated. The resultant second harmonic pulses were compressed to their Fourier limit of ~ 13 fs. These high power (energy per pulse > 1.5 mJ), short pulses are of great interest for ultrafast sciences. Furthermore, a broadband supercontinuum ($\sim 220 - 500$ nm) generation through a hollow core fiber has been demonstrated, to the best of my knowledge, the broadest ever using the above second harmonic pulse as input of hollow core fiber. All of these advancements contribute to an ever more elaborate attosecond waveform synthesizer that should help driving experiments in atomic and molecular physics for years to come.

Structure of the thesis

- *Chapter 1*: Short introduction to light-matter interactions and overview of the theory as well as some theoretical models utilized.

- *Chapter 2*: The experimental setup is described. Generation of optical attosecond pulses.

- *Chapter 3*: Motivation towards developing TW scale waveform synthesizer and introduction to supercontinuum generation, practical design as well as implementation of the synthesizer are shown. The results of highly efficient direct second harmonic generation are reported and compared to simulations. Supercontinuum generation and its subsequent spectrum division to five channels are also demonstrated. Compression of pulses in some channels is shown.

- *Chapter 4*: Short introduction and description of the experimental setup to generate EUV from solids. Measured results are reported extensively in several aspects. Development of the semiclassical and quantum-mechanical model and their applications in interpreting the experimental data. Comparison to experimental results is presented and an application to spectroscopy is derived.

- *Chapter 5*: Bound electron spectral responses of Kr under interaction with synthesized light transients are recorded and showed. Several models describing the phenomena are presented. Insight into non-instantaneous response is illustrated.

- *Chapter 6*: Conclusions.

List of publications directly related to this thesis

- **T. T. Luu***, M. Garg*, S. Y. Kruchinin, A. Moulet, M. T. Hassan, and E. Goulielmakis. *Extreme ultraviolet high-harmonic spectroscopy of solids.*
  Nature, vol. **521**, no. 7553, pp. 498-502, 2015.

- M. T. Hassan*, **T. T. Luu***, A. Moulet, O. Razskazovskaya, P. Zhokhov, M. Garg, N. Karpowicz, A. M. Zheltikov, V. Pervak, F. Krausz, and E. Goulielmakis. *Attosecond optical control of bound electrons.*
  Nature, *submitted.*

- O. Razskazovskaya*, **T. T. Luu***, M. Trubetskov, E. Goulielmakis, and V. Pervak. *Nonlinear absorption in dielectric multilayers.*
  Optica, submitted.

Further publications within the framework of the author's dissertation

- M. T. Hassan, A. Wirth, I. Grguras, A. Moulet, **T. T. Luu**, J. Gagnon, V. Pervak, and E. Goulielmakis. *Invited article: Attosecond photonics: Synthesis and control of light transients.*
  Review of Scientific Instruments, vol. **83**, no. 11, 2012.

- A. Wirth, M. T. Hassan, I. Grguras, J. Gagnon, A. Moulet, **T. T. Luu**, S. Pabst, R. Santra, Z. A. Alahmed, A. M. Azzeer, V. S. Yakovlev, V. Pervak, F. Krausz, and E. Goulielmakis. *Synthesized light transients.*
  Science, vol. **334**, no. 6053, pp. 195-200, 2011.

Chapter 1

Light matter interactions: a few elements

1.1 Weak field regime

1.1.1 Nonlinear polarization and nonlinear optical susceptibilities

Media interact with an incoming light field depending on the field strength. If the light field is weak (at the order of 10^{10} W/cm^2 or less in terms of peak intensity - from now on until the end of the thesis, peak intensity is regarded to the maximum instantaneous peak intensity $I = \epsilon_0 c E_0^2$, not the cycle-averaged intensity $I = 1/2\epsilon_0 c E_0^2$ as people usually use), the response of the medium appears to be independent of the light intensity, but when the incident peak intensity approaches the order of 10^{13} W/cm^2 or less (thanks to the invention of lasers [2]), the medium response will start to behave strongly dependent on the field strength. At this regime of interaction, the medium will act as a catalyst, stimulating the exchange of light waves' momentum and energy, resulting in a creation of new light waves at different frequencies (energy and momentum). The strength of this mixing process depends on the medium and it can be derived from the time dependent perturbation theory as in [75]. The medium's polarization can be approximated as a power series of the incident electric field (more details on the derivation can be found in [75], Section 3.2):

$$\mathbf{P}(t) = \epsilon_0 \left[\chi^{(1)}\mathbf{E}(t) + \chi^{(2)}\mathbf{E}(t)^2 + \chi^{(3)}\mathbf{E}(t)^3 + \chi^{(4)}\mathbf{E}(t)^4 + \chi^{(5)}\mathbf{E}(t)^5 + \dots \right] \tag{1.1}$$

This polarization defines current density $\mathbf{J} = \partial\mathbf{P}/\partial t$ which is included in the Maxwell's equations. Therefore this polarization shapes how the generation of the new photons (or mixing of incident photons) will be and hence it plays a crucial role in describing light matter interaction.

In addition, the above equation shows the nonlinear polarization as a contribution of all order terms together with the corresponding susceptibilities χ^n. The strength of χ^n defines effectively which order of interaction should be taken into account for a particular electric field strength.

1.1.2 Nonlinear processes

For media that do not have inversion symmetry, all $\chi^{2\cdot m}$ terms (m is an positive integer) exist. If a medium posses significantly high χ^2 such that it dominates all other higher order terms, this medium is responsible for all second order processes, for example, sum- (second harmonic generation in particular) and difference- frequency generation and optical parametric amplification. Among these processes, second harmonic generation will be studied in details in Chapter 3.

On the other hand, once a medium has an inversion symmetry, effectively there are no $\chi^{2\cdot m}$ terms, only the odd terms $\chi^{2\cdot m+1}$ remain in the Eq. 1.1. In the lowest order consideration of the available nonlinear term, χ^3 is responsible for third order processes: third harmonic generation, self- and cross- phase modulation and general four wave mixing. Applications of these processes are utilized in Chapter 5.

1.2 Strong field laser physics

When the electric field intensity approaches 10^{14} W/cm^2 or higher, the electric field strength is comparable to the Coulombic fields and modifies strongly electronic dynamics in atoms and molecules. In the other words, the electric field is strong enough so that it bends the potential significantly, leaving the electrons high possibility to tunneling out from the potential or in the extreme case; just leaving the potential directly. Due to the oscillatory nature of light waves with cycles (possibly few) of oscillation, there are possibilities that the electrons could be driven back to collide with the core, making elastic or inelastic scattering. It is this regime of intensity that triggers many interesting physics [76, 77] some of which are briefly reviewed below.

1.2.1 High order harmonic generation from gas targets

Although there are extensive reviews of HHG [78–80] and a detailed comprehensive tutorial [81] was given, I attempt to outline some key developments in this area of research:

- **First observations of HHG:** McPherson *et al.* [82] and Ferray *et al.* [20] were the first to report HHG spectrum generated from KrF* at 248 nm and Nd:YAG lasers at 1064 nm up to the 17^{th} (14.6 nm) and 33^{rd} harmonics (32.2 nm) respectively. Surprisingly, instead of a fast decreasing intensity expected from perturbative harmonics at high order (more than 5), a formation of a plateau spectrum was observed by exposing rare gases under these strong laser pulses.

- **Simple man's theory:** One of the first numerical simulations trying to shed light on this topic was the works of Kulander *et at.* [83] using the method previously published [84]. By solving the 3D-TDSE numerically, the single atom response spectrum can be evaluated from the time-dependent polarization. They showed that the maximum high harmonic energy in the plateau region can be approximated by $E_{\max} \approx I_p + 3U_p$ where I_p is the ionization potential, $U_p = e^2E^2/4m\omega^2$ is the ponderomotive energy of the released electrons with E, ω are the electric field amplitude and carrier frequency. This model has shown significant applicability in HHG: it determines the cutoff energy and its dependence on the ionization potential

(choice of the atoms) and the electric field amplitude and carrier frequency (choice of the laser parameters).
Even though a simple model for the driving of ionized electrons in the long wavelength limit (which causes HHG) was reported earlier [85], it was after the works of Kulander *et al.* that a robust simple man's theory was developed and it is called a three step model [12]: first (ionization step), the electric field is strong enough such that it bends the Coulombic potential, an electron is tunneled out to the continuum state. Secondly (propagation step), the released electron is driven by the electric field and thirdly (recombination step), there are possibilities that the electron can be recombined back to the ground state, generating an XUV photon whose energy is given by I_p plus total ponderomotive energy $\approx I_p + 3.2U_p$.

- **Further developments (simulations and experiments):** Although a full 3D-TDSE has been demonstrated it is too complicated to apply to complex systems. Therefore a quantum theory with an approximation which is called *strong field approximation* (SFA) was developed [23, 86] which not only preserves the ideology behind the three step model but also quantitatively gives good results for the cutoff energy and partially the HHG spectrum.
  Furthermore, from the idea of the three step model, the released electrons may miss the ionized atom in the recombination step if the incident electric field is not linearly polarized. The HHG efficiency is therefore dramatically decreased. This effect has been demonstrated experimentally [87] and investigated theoretically [88].
  In addition, the macroscopic aspects of the HHG have been investigated and improved such as the optimization of the laser parameters, carrier wave, gas medium, temporal and spatial profiles. Due to the fact that the generated HHG are coherent and completely synchronized to the driving electric field, XUV pulses are emitted in the form of a train, each with attosecond duration and they are extremely sensitive to the parameters of the incident electric field. Utilizing these pulses with attosecond time window, electronic processes can be investigated with attosecond resolution.

1.2.2 High order harmonic generation from plasma surfaces

When the laser intensity is strong enough such that most of the atoms (molecules) on the surfaces are ionized, a dense layer of plasma is formed. This usually requires focused intensities larger than 10^{14} W/cm^2 for nanosecond lasers up to more than 10^{16} for femtosecond laser pulses. The first experiment reported the observation of extended harmonic series (2^{nd} to 11^{th}) of the fundamental frequency ($10.6\,\mu$m) down to $0.95\,\mu$m was done by Burnett *et al.* [89] in 1977. Soon, Carman *et al.* using similar techniques had demonstrated HHG up to 29^{th} order [90] and later up to 46^{th} order [91] in 1981. First theoretical description of this HHG was suggested by Carman *et al.* [90] and a theory based on the step like structure of the generated plasmas density was proposed by Bezzerides *et al.* [92]. In this picture, the electron performs an anharmonic motion under influence of the incident electromagnetic field and the step-like plasma density and as a result a series of odd and even harmonics are created.

Thanks to the fast progress in laser development, high intensity, high power laser

systems can be implemented in the table-top scale and first observations of HHG from solid target on a table top system were reported [24, 93]. Although one can choose to perform particle-in-cell simulations [26, 27] to resolve the complex collective electron dynamics under influence of strong field, it is found that a simpler model of *oscillating mirror* provides good agreements to the particle-in-cell simulations [26]. Essentially, there are two assumptions used in the *oscillating mirror* model: firstly, the detailed spatial distribution of the electron density is neglected, the whole electrons can be represented by a characteristic boundary (upon which the incident light is reflected) and the ions are assumed to be fixed as an immovable background. Secondly, the incident electromagnetic field is mostly reflected on this characteristic boundary surface hence the reflected light incorporates the oscillatory motion of this boundary (driven by the electromagnetic field) to its temporal profile as well as its spectrum. Using these assumptions, the motion of a free electron in this characteristic electronic boundary (plasma surface) can be calculated classically in both relativistic and non-relativistic regime [25], thus the spectrum of the reflected light on this plasma mirror can be derived.

1.2.3 Attosecond physics

Emergence of isolated single attosecond pulses from the HHG [30, 34, 36, 66, 94] has opened a new era of ultrafast sciences where steering and probing of the electronic dynamics can be performed in a radically high resolution. From the physical mechanism of the generation of the HHG spectra and their corresponding XUV pulses in gases, one can not only measure the generation of the XUV pulse but also control this process by manipulating the released electrons (and their re-collisions as a consequence) by an engineered electric field [15]. Furthermore, this degree of measurement and control of the generation of attosecond XUV pulses is even extended more such that generation of isolated sub-100 as pulses is possible [30]. The generation of attosecond pulses slowly transformed the ultrafast sciences from femtosecond chemistry (where femtosecond light pulses are used to trace chemical reactions) to attosecond physics (where light pulses as short as attoseconds are utilized to pump and/or probe electronic processes which happen on faster time scales than that of chemical reactions). All the tools, techniques as well as their applications and implications of attosecond physics are thoroughly reviewed by Krausz and Ivanov [4].

1.3 Theoretical consideration

In order to investigate the behavior of a quantum system under interaction with the incident electromagnetic fields, one has to solve the Time Dependent Schrödinger Equation (TDSE) with the interacting electromagnetic field included in the time dependent Hamiltonian $\mathbf{H}$ (which is one of the most important theoretical tools to investigate ultrafast phenomena [80]):

$$i\hbar\frac{\partial\Psi(\mathbf{r},t)}{\partial t} = \mathbf{H}\Psi(\mathbf{r},t) \tag{1.2}$$

From here, one can get the solution of the TDSE as follows:

$$|\Psi(\mathbf{r}, \Delta t)\rangle = \exp\left(-\frac{i\mathbf{H}\Delta t}{\hbar}\right)|\Psi(\mathbf{r}, 0)\rangle \tag{1.3}$$

Knowledge of the temporal evolution of the wave function $|\Psi(\mathbf{r}, t)\rangle$ gives us complete information needed to calculate observables. However, more often than not, the form of the Hamiltonian does not allow one to get the analytical solution thus generally a numerical solution is needed. More specifically, because Eq. 1.3 requires exponential function of the $\mathbf{H}$ operator while the Hamiltonian includes both the potential (whose direct exponent maybe straightforwardly calculated) and momentum operator (whose exponent mostly is problematic) therefore one must follow certain routes in order to evaluate this numerically and efficiently.

Many problems can be treated within the framework of the *single active electron* (SAE) approximation [95] where it is assumed that there is only one electron that is actively interacting with the incident electromagnetic fields and a suitable single-electron potential is selected. This approach has proven to treat well a variety of problems or even multi-electron interactions [80].

Numerical solution of the one dimensional SAE TDSE is well tractable on a modern personal computer for any given approach (see Appendix A.1 for a typical solution using split-operator algorithm for the exponent operator evaluation and Fourier transform for the momentum operator evaluation). The result of this calculation can already give us tremendous amount of information related to the interaction process. From the weak field response to the high order harmonic generation (HHG), etc, they can be captured by this model. Typically one dimensional simulations of this kind could easily overestimate the calculated polarization thus not giving realistic spectra. For a more precise simulation, one needs to evaluate a three dimensional TDSE (still in the SAE approximation) [96]. In this case, most physical processes are taken into account. The calculation naturally explain very well the perturbative response as well as resonant response. However, this approach does pose some disadvantages: it is hard to separate different physical processes, the dephasing time cannot be included as transparently as in the case of the density matrix approach (although this can be included using complex potentials), etc, and finally the calculation time is not as fast as the 1D simulations.

For the sake of having a more accurate tool describing the interaction processes, a multi-electron TDSE or a time dependent density functional theory (TDDFT) [97–99] might be needed. However, invoking such sophisticated calculations also means there is a trade-off with the calculation time. One can get only few representative calculations and it is time consuming to try to match the experimental data quantitatively.

Chapter 2

Experimental setup - synthesis of optical attosecond pulses

In quest to advancing manipulation and control of light pulses from nanosecond [100] to picosecond [101–103], and femtosecond [104, 105] time scale, a great leap has been done by the generation of synthesized light transients [58]. Instead of utilizing conventional pulse shaping techniques (standard pulse shaper [103, 106], phase and amplitude masks [107], spatial light modulators [108–110], acousto-optic modulators (AOM) [104, 111, 111], acousto-optic programmable dispersive filter (AOPDF) [112–114] and others [54, 115, 116]), direct waveform manipulation of light waves was performed with attosecond resolution [117]. Here I will only outline experimental setup and the brief generation and characterization of the attosecond pulses used in this thesis.

2.1 Experimental setup

2.1.1 Femtosecond carrier envelope phase-locked high power laser amplifier

The front end of our experimental setup is a commercial femtosecond phase-locked, high power laser amplifier (Femtopower^{TM} Compact^{TM} Pro HE, Femtolasers GmbH), shown in the left part of Fig. 2.1 which is an upgraded version of previous technologies [118].

A train of ultrashort pulses emerging from a Kerr-lens mode locked oscillator is seeded into the 9-pass amplifier (1st amp) of the two-stage amplifier laser system. The ultrashort pulses then undergo amplification, picking 3 kHz pulses, and are amplified to ~ 1.3 mJ. Because of the AOPDF, one can stretch the pulses to ~ 25 ps using glass blocks without suffering complicated high order spectra phase. Nonetheless, because the Dazzler helped digging the bigger hole and making the broader spectrum, this came at the expense of the amplified pulse's energy. To compensate for that, we intentionally focused the pumping green laser beam harder on the crystal (replacing the 27 cm focal length green lens to 25 cm focal length). This enhanced the amplification and put the crystal more in saturation which stabilized better the pulse to pulse energy. However, the 1st amplifier becomes much more dependent on alignment and ambient temperature, the thermal lensing is more problematic and damage of Ti:Sapphire crystal is more likely to happen. Secondly, the transmission grating compressor has eliminated the problems of the prism compressor:

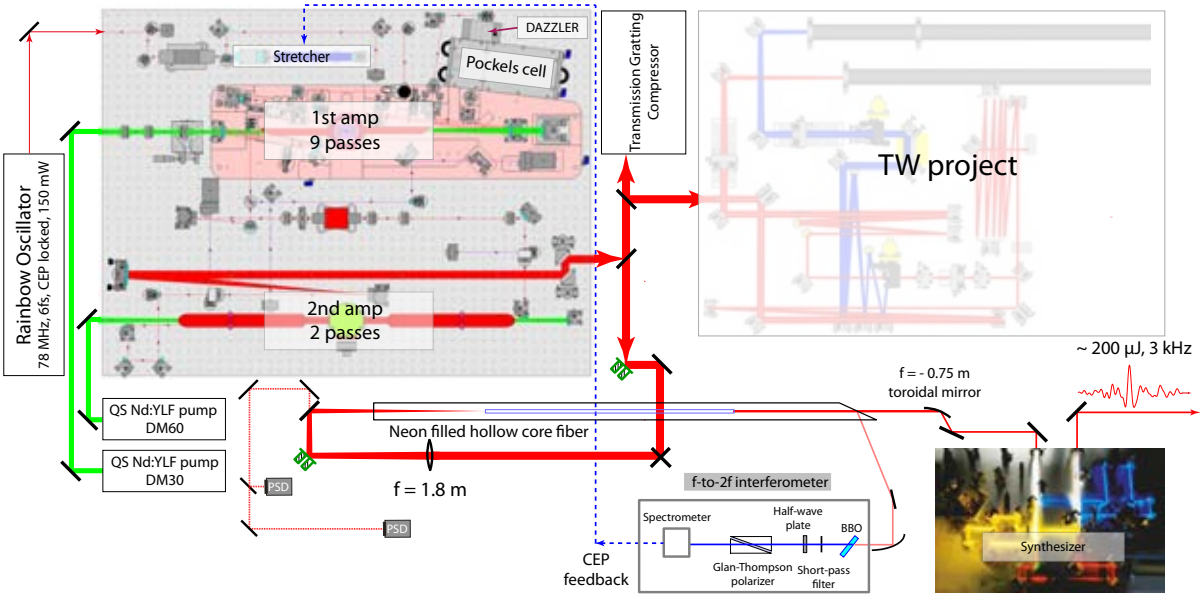

Figure 2.1: Schematic diagram of the laser system in Attoelectronics group.

narrow spectral width, limited compression range and self phase modulation inside the prisms (in the other words: low power threshold). At the exit of the laser amplifier, by measuring the pulses temporal profile with a Self-Referenced Spectral Interferometry device [119] and providing feedback to the grating compressor as well as the Dazzler [120], 1 mJ, $\sim$ 22 fs pulses are obtained on the daily basis which are virtually Fourier limited in duration with a bandwidth of $\sim$ 75 nm at $\sim$ 790 nm.

In the second-stage amplifier (2nd amp), a cryogenic cooling was utilized. For the pumping power of $\sim$ 42 W from the DM60, the chiller (set temperature at $-166\,^0$C) is able to cool the crystal down to $\sim$ 132 K without the seed beam and $\sim$ 127 K with the seed beam on. In order to gain additional amplification while maintaining the pulses peak intensity below the damage threshold of the crystal, the beam size (both seed and pump) on the crystal is significantly enlarged in the 2nd amp ($\sim 800\,\mu$m instead of $\sim 300\,\mu$m in the 1st amp). After the grating compressor, we typically have $\sim$ 3 mJ and average power of $\sim$ 9 W and almost transform limited pulses at $\sim 22-23$ fs. For experiments carried out in chapter 4 and 5, only the 1st amp has been used. For the developments in chapter 3, both amplifiers are used to deliver maximum possible energy/power.

Carrier envelope phase stabilization

CEP stabilization of the oscillator pulses In principle, by utilizing either a f-to-2f [7, 121–123] or a f-to-zero technique [124], the CEP or (CE offset) of the laser pulse train can be obtained. With the help of locking electronics, CEP stabilization can be performed. Eventually phase noise less than 30 mrad in 20 s, with more than $24h$ of CEP locking was demonstrated [125] using feed-forward scheme.

CEP stabilization of the amplified pulses In our lab, the f-to-2f technique is utilized. More details of the implementation can be found in [126].

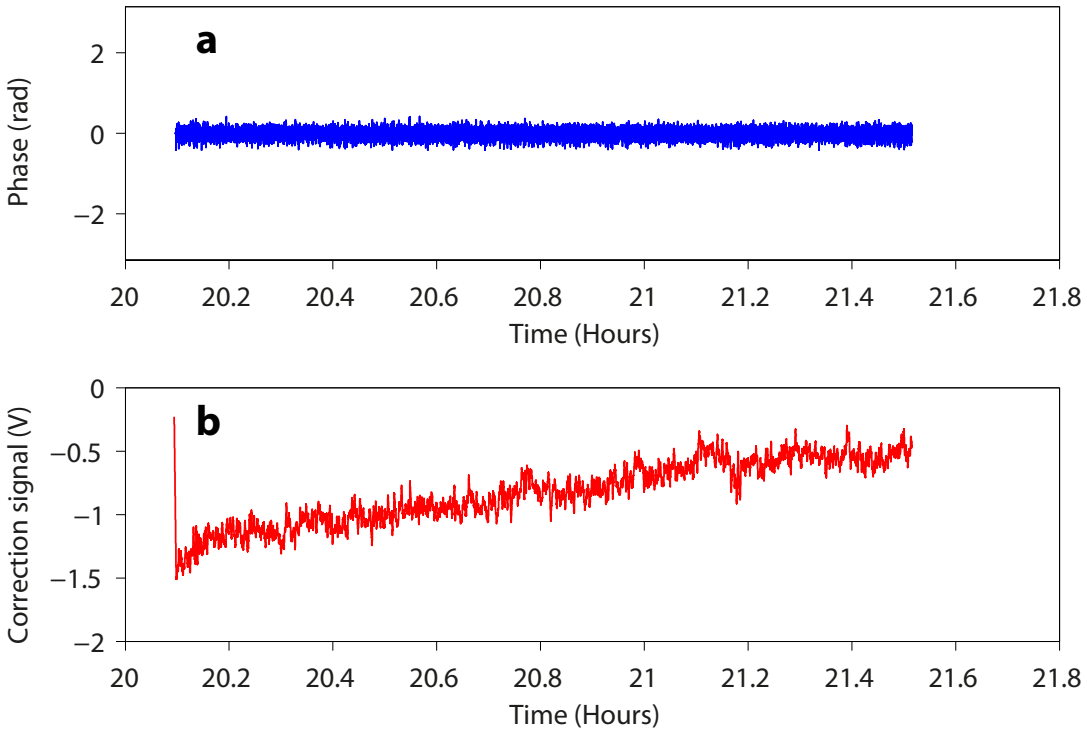

Figure 2.2: CEP stabilization: current status. a, Measured CEP values of the amplified pulses for $\sim$ 2 hours. The standard deviation of the CEP noise is $<$ 100 mrad. **b,** Applied feedback signal measured at the same time as the measurement of the CEPs.

By combining the CEP stabilization of both the oscillator and of the amplified (broadened) pulses, CEP locking of the amplified (broadened) pulses is implemented and a typical stabilization result is shown in Fig. 2.2.

Additional feedback loop It is often the case that the voltage range of the AOM is not sufficient to overcome the long term drift of the pulses' CEP inside the oscillator. As a result, once the limit (voltage compensation range) of the AOM is reached, the wedges were designed to move mechanically to compensate for that and consequently disturb the CEP stabilization loop during its movement. Another feedback loop was implemented in the system. It reads the output of the input of the AOM then depending on its value, it will regulate the pumping power of the oscillator (Verdi V6) via RS-232 communication. This precise and highly applicable approach has improved the long term operation of the CEP stabilization significantly. In principle, as long as the beating signal f_{CEO} (carrier envelope offset frequency) remains within the locking range, the CEP stabilization of the oscillator (hence of the complete system) will be maintained for several hours.

2.1.2 Light field synthesis: principles and implementation

For light field manipulation on picosecond and femtosecond time scales, a standard pulse shaper [103, 106] can be used. It generally comprises of three steps: a device that can

transform the pulse in time into its Fourier counterpart (most frequently being a grating or prism) at which different frequencies are spatially displaced, a device that modulates the different frequencies and a device that converts the pulse back to time domain, which sometimes can be the first device, but aligned such that the pulse travels in opposite direction. However, for broadband, high intensity laser pulses, a grating will have a severe problem when the pulses' spectral bandwidth exceeds one octave and a prism will exhibits nonlinear behavior. Most of these shortcomings have been solved by the use of dispersive optics. These dispersive mirrors have been designed to control the dispersion [127] (chirped mirrors) and they are successfully applied to compress weak short pulses [128] as well as short pulses at high peak power [129]. Supercontinuum generation by focusing intense laser pulses into hollow core fiber together with the use of chirped mirrors have broadened research scope using short pulses, high power laser sciences, eventually gives birth to attosecond physics [4, 34]. Eventually, dispersive optics play an important role in a light field synthesizer [58, 117].

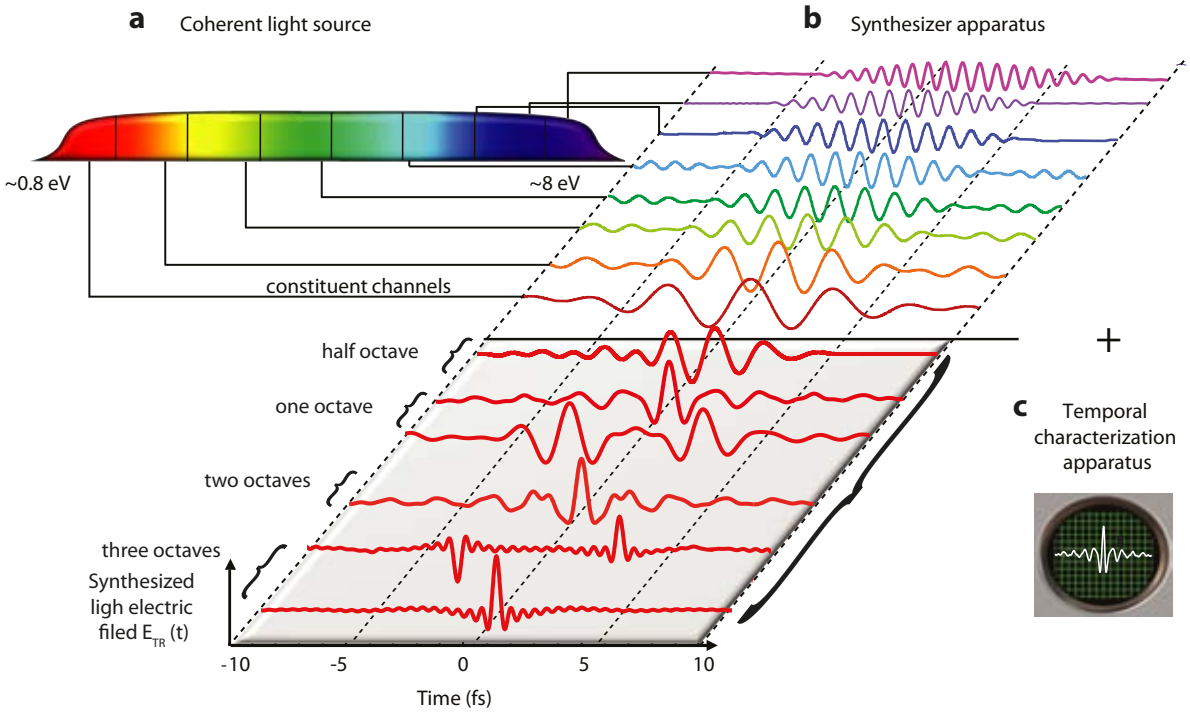

Figure 2.3: Principle of light field synthesis. **a,** A broadband coherent light source is required. **b,** A synthesizer apparatus firstly divides the source into constituent channels (bands). Pulses in each of the channels will be individually compressed and their relative phases will be adjusted. Finally, all the channels are coherently superimposed [spatially and temporally] to create ultrashort synthesized light pulses at the exit of the synthesizer. Possible waveform constructions are showed in the lower half panel given the source bandwidth of half, one, two, or three octaves. **c,** A precise characterization apparatus is required to sample accurately the field waveform and provide feedback to the waveform synthesizer. [Adapted from [117]].

The principle of light field synthesis is illustrated in Fig. 2.3 while a more elaborate discussion on the synthesis, the light field synthesizer as well as the peripheral technologies are detailed in [117]. With the scope of the thesis, I will briefly overview.

The most broadband coherent light source

Practically, in our experimental setup, a coherent broadband source which extends spectrally over more than two optical octaves have been demonstrated [58, 117]. Further improvement of the hollow core fiber setup helped to extend the supercontinuum spectrum down to the deep ultraviolet (DUV) region of the electromagnetic spectrum. Spectral components extending to $\sim$ 200 nm are typically generated by our setup, as shown in Fig. 2.4.

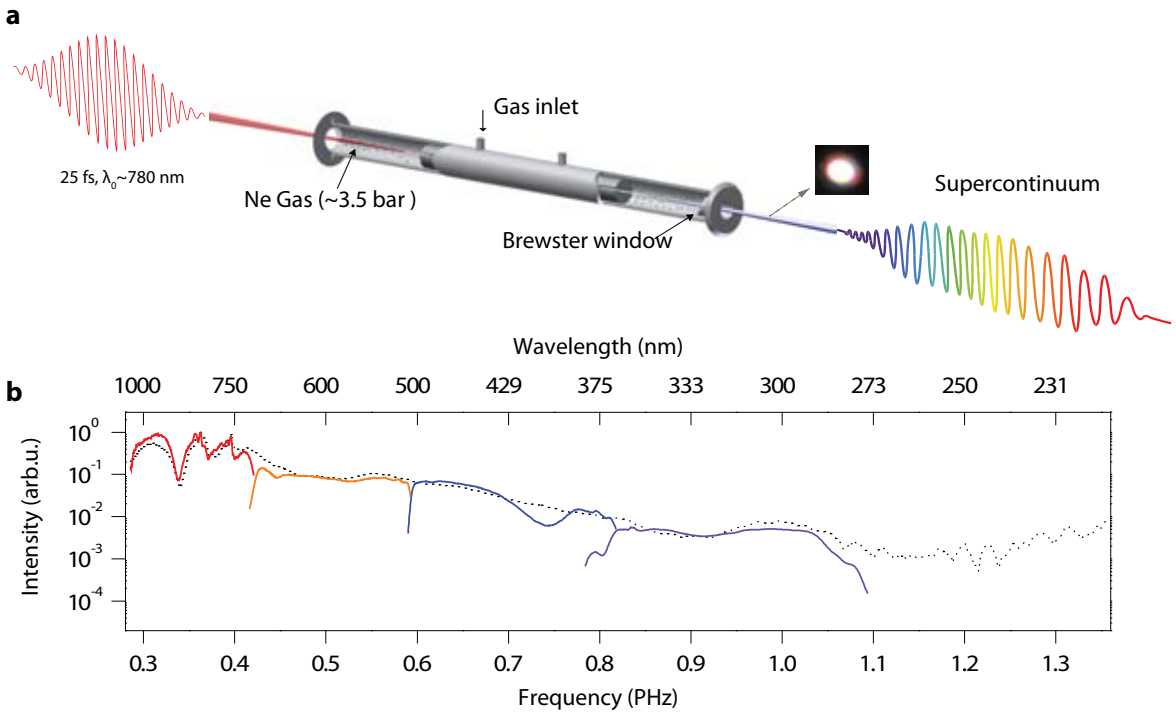

Figure 2.4: Broadband supercontinuum spectra at the exit of the hollow core fiber. **a,** Hollow core fiber setup. **b,** Output spectrum (dashed black line). Spectra of the individual channels are shown in red, orange, blue and violet lines respectively. Adapted from [17].

Synthesizer apparatus

A schematic and a photograph of the light field synthesizer are shown in Fig. 2.5. The main components of this synthesizer are:

- **Division of the incoming pulses into 4 channels:** Broadband dichroic beam splitters play a key role in dividing the pulses. As an extension of the previous work [58, 117], one more channel in the DUV region has been implemented [17]. The total number of channels inside the synthesizer is now 4 with their bandwidth spanning as Ch_{NIR} : 1100 − 700 nm, Ch_{Vis} : 700 − 500 nm, Ch_{Vis-UV} : 500 − 350 nm, Ch_{UV-DUV} : 350 − 270 nm

- **Manipulation of the light pulses in individual channels:** Two mirrors in each channels are put on delay lines controlled by translation stages for coarse and

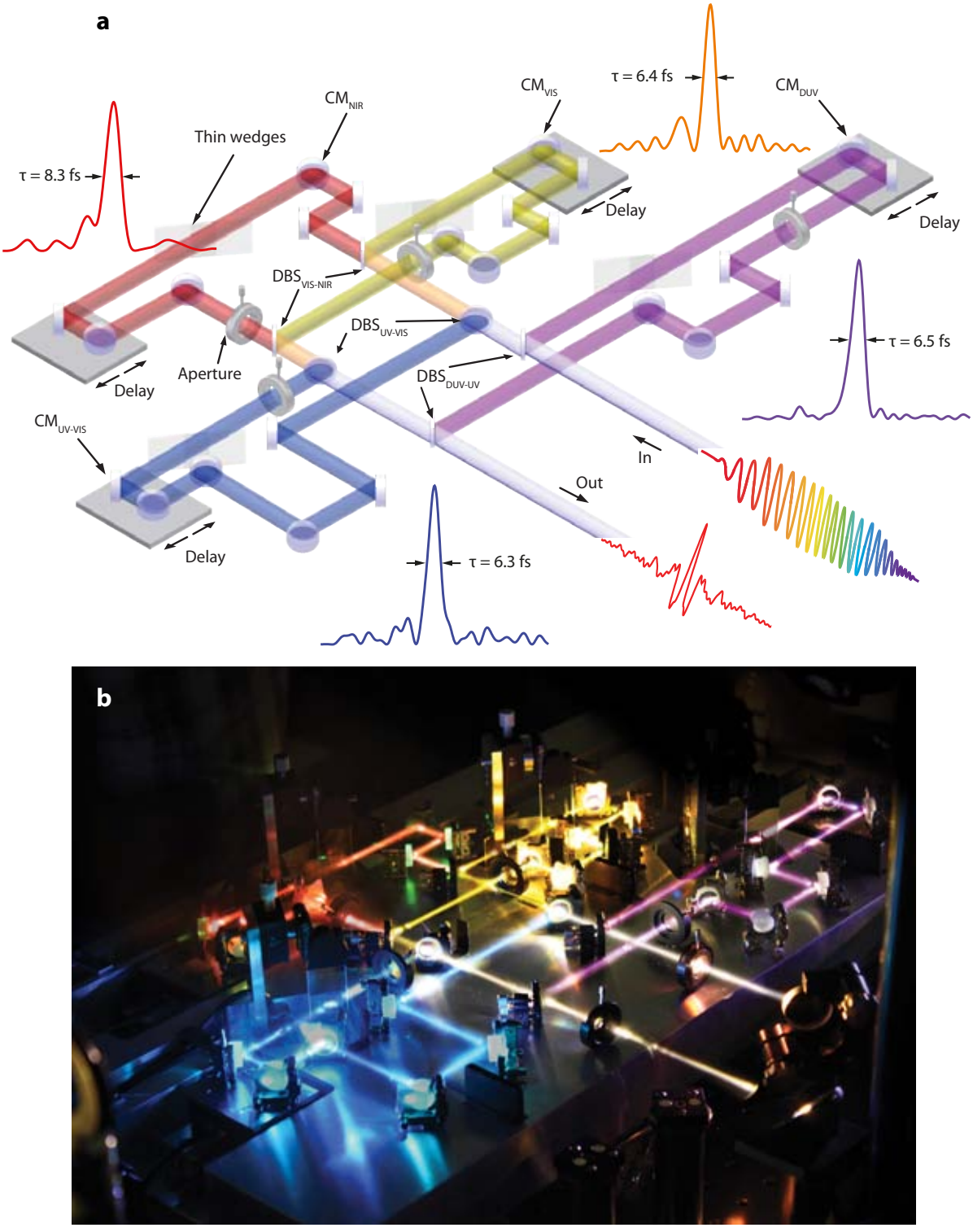

Figure 2.5: Second generation light field synthesizer. a, Schematic representation of the synthesizer. DBS: Dichroic beam splitters; CM: Chirped mirrors. Pulses in each channels are compressed and their temporal profiles are shown accordingly (same color codes). **b,** Photograph (perspective view) of this synthesizer in operation. Adapted from [17].

piezo-electric for fine tuning of relative temporal delays or relative spectral phases. There are apertures, glass windows, and wedge pairs in each channel to adjust their power, dispersion as well as their CEP. Furthermore, all the optics that are used for the transportation of the individual beams inside each arm are dispersive optics and allow compression of these pulses. In order to make sure that pulses in each of the channels are well compressed, a Transient Gating - Frequency Resolved Optical Gating (TG-FROG) apparatus [126] is utilized. The apparatus is based on well known FROG technique [130, 131] and its variant TG-FROG [132]. This apparatus is very universal such that it can be employed to measure the temporal profile of pulses in all the channels without any modification to the setup.

- **Coherent superposition of the pulses temporally and spatially:** After the light pulses in each arm have been well compressed, they are combined into one beam by using the same dichroic beam splitters used for their division. However, special care must be taken to make sure they overlap temporally and spatially.

- **Passive and active path-length stabilization:** Passive stabilization using a cooling circuit made inside the monolithic board helps stabilizing the temperature of the complete optical setup (all optical mounts are mounted directly on the board without any extension posts). Additionally, an active path length stabilization helps maintaining the relative phases between pulses in different channels by providing a slow feedback to piezo-electric stages mounted on the delay lines during experiments.

2.1.3 Generation of isolated attosecond XUV pulses and its characterization by attosecond streaking metrology

In our experimental setup, single isolated attosecond XUV pulses are generated by a combination of a ultrashort laser pulse (preferably ~ 2 cycles or less) and proper spectral filtering of the cutoff region of the HHG spectrum ($80 - 120$ eV).

Characterization of ultrashort laser and attosecond XUV pulses by attosecond streaking

The characterization of attosecond XUV pulses is a considerable challenge. Powerful techniques well developed in the past such as Frequency Resolved Optical Gating [130] (FROG) or Spectral Phase Interferometry for Direct Electric-field Reconstruction (SPIDER) [133] could not immediately be ported to the XUV domain. Attosecond streak camera was suggested by J. Itatani, F. Krausz and P. B. Corkum *et at.* [134] and eventually realized by E. Goulielmakis *et al.* [94] and subsequently by others [36, 66].

In the attosecond streaking apparatus used in this chapter, an XUV pulse and an optical pulse are collinearly focused on a Neon gas target, electrons from the valence shells of Neon atoms will be photoionized by the XUV. The transition amplitude of these electrons from the moment of release to its final continuum state $|\mathbf{v}\rangle$ is described by

[23, 134–136] (in atomic units):

$$a(\mathbf{v},\tau) = -i\int_{-\infty}^{\infty} e^{i\varphi(t)}\mathbf{d}_{\mathbf{p}(t)}\mathbf{E}_{XUV}(t-\tau)e^{i(W+I_p)t}dt \tag{2.1a}$$

$$\varphi(t) = -\int_{t}^{+\infty}\left[\mathbf{v}\cdot\mathbf{A}(t') + \mathbf{A}^2(t')/2\right]dt' \tag{2.1b}$$

where $\mathbf{A}(t)$ is the vector potential of the fundamental field, $\mathbf{v}$ is the final momentum of the electrons, $\mathbf{p}(t) = \mathbf{v} + \mathbf{A}(t)$ is the instantaneous momentum of the electrons, $\mathbf{d_p}$ is the transition dipole matrix element from the ground state to the continuum state $|\mathbf{p}\rangle$, $\mathbf{E}_{XUV}(t)$ is the XUV pulse temporal profile, $W = \mathbf{v}^2/2$ is the kinetic energy of the electrons and I_p is the ionization potential of the streaking gas.

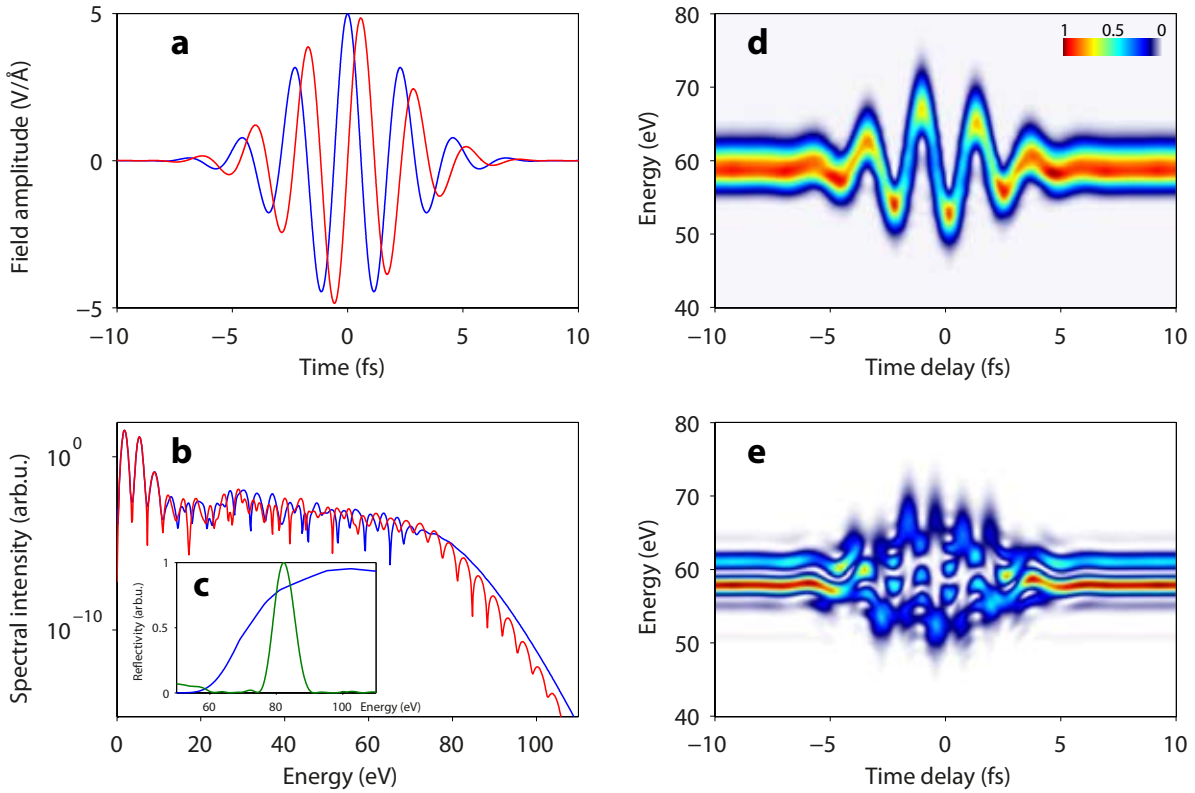

Figure 2.6: Simulated isolated attosecond XUV pulse generation and its attosecond streaking. **a,** Ultrashort laser pulses (Gaussian envelope, $\lambda_{\text{carrier}} = 700$ nm, FWHM = 4 fs) used for generation of single isolated attosecond pulses and attosecond streaking. Two CEP settings are represented: $\varphi_{\text{CE}} = 0$ (solid blue line) and $\varphi_{\text{CE}} = \pi/2$ rad (solid red line) . **b,** HHG spectra calculated from Lewenstein's model for Neon. Same color code applies. **c,** Transmission spectrum of 200 nm Zr filter (solid blue line) and reflection spectrum of the inner mirror (solid green line). Their amplitudes are normalized. **d,e,** Attosecond streaking spectrogram calculated for the filtered attosecond pulses for these two CEP settings and for Neon gas. The streaking field used is 0.5 V/Å.

Figure 2.6a,b show the electric fields and the simulated HHG spectra respectively. Since in the regime of short pulses, there exists CEP at which a broadband supercontin-

uum is observed at the cutoff region of the HHG. Proper spectral filtering of this spectrum (Fig. 2.6c) could lead to the generation of single isolated attosecond XUV pulses.

Fig. 2.6d,e show evidently the difference between a streaking trace of a single isolated attosecond pulse and for the case of a double pulse (assuming that $\mathbf{d_p}$ is constant across the whole photoelectron spectrum). From these streaking traces, a complete reconstruction of attosecond burst is possible through a FROG algorithm specifically tailored for XUV pulses [136] (known as FROG CRAB). Although the technique used in FROG CRAB, Principal Components Generalized Projections Algorithm - PCGPA [137], is very efficient and reliable, it suffers two main drawbacks [138] for attosecond pulse applications: boundary condition is not generally satisfied and impractical grid size requirements. A new attosecond FROG algorithm, Least-Square Generalized Projections Algorithm - LSGPA, was proposed and implemented [138] that addressed above issues and accurately characterized attosecond pulses from streaking measurements.

These above methods deal with the characterization of the fundamental fields as well as the generated attosecond XUV pulses. However, for the purpose of characterizing only the optical fields, provided that the generation of isolated attosecond pulses is guaranteed, a much simpler method using evaluation of center of mass of the photoelectron spectrum to calculate incident electric field was compared with PCGPA and LSGPA and turned out to be accurate enough [117]. Intuitively, one could expect that the main feature of the Fig. 2.6d is the vector potential of the electric field in Fig. 2.6a (blue solid line).

2.2 Optical attosecond pulse generation and characterization

In quest to make ever shorter optical pulses beyond the state-of-the-art 2.1 fs pulses [58] we have to inevitably expand the bandwidth of the laser pulses. Supercontinuum generation from the hollow core fiber in our lab was optimized to support spectral bandwidth ranging from 1100 to 270 nm (or 1.1 to 4.6 eV, Fig. 2.4). However, due to the intrinsic properties of the SPM, the high and low energy spectra are weaker in intensity compared to the central components. Therefore, proper spectra shaping is required and was actually implemented as a special coating on a mirror in Fig. 2.7.

These efforts have eventually lead to the synthesis and generation of optical attosecond pulses whose typical streaking spectrogram is illustrated in top left corner of Fig. 2.7.

In this regime of optical pulse duration, there is only one strong half cycle of the optical field that drives the free electrons significantly compared to other half cycles. In the streaking spectrogram, it shows up as a monotonic rise of the vector potential of the field from the minimum photoelectron energy to maximum values. As a result, the reconstructed electric field comprises of a dominant, nearly isolated, half-cycle peak (centroid wavelength $\sim$ 530 nm) Fig. 2.8a. Its intensity profile (Fig. 2.8b) is roughly 4 times stronger than that of adjacent peaks. Consequently, the main half cycle contains $\sim$ 50 % of the total energy of the pulse. Evaluation of its duration on the basis of the instantaneous intensity profile of the half-cycle peak in Fig. 2.8b yielded a FWHM duration of $\sim$ 400 as, whereas an evaluation based on conventional definition of the intensity envelope yielded $\sim$ 975 as. Light waveforms like the one shown in Fig. 2.8 will be utilized in experiments discussed in later chapters.

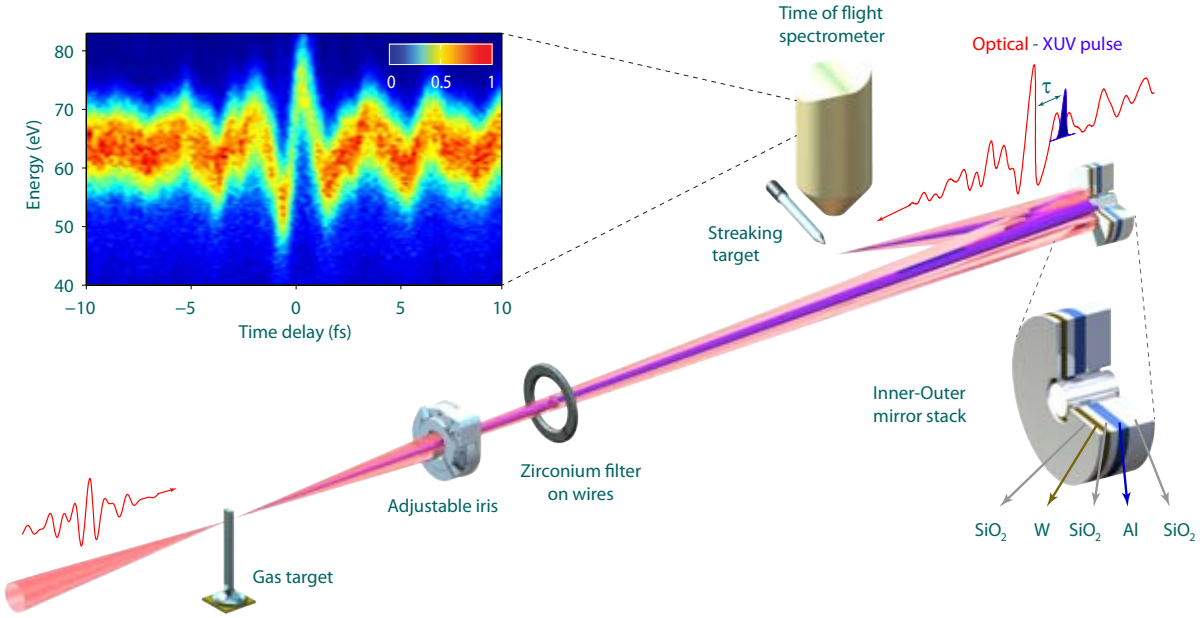

Figure 2.7: Attosecond streaking for optical attosecond pulses generation. Two important modifications of the experimental setup are being shown: metallic filters being hosted on 30 μm tungsten wires and the specific metallic-dielectric-metallic coating on the outer mirror. The outer mirror is cut by its cross section in order to show the structure of the coating layers.

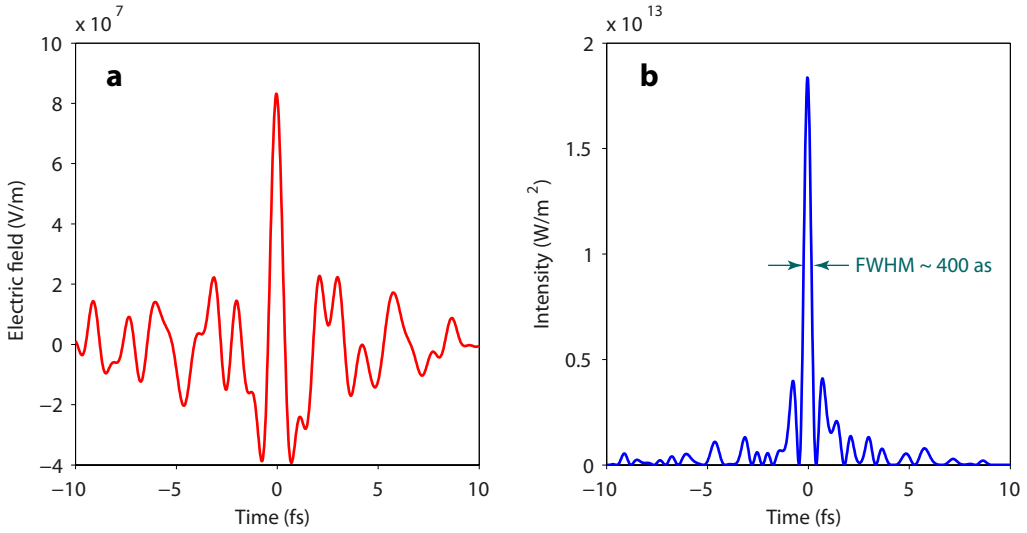

Figure 2.8: Optical attosecond pulses. a, Electric field characterized by the attosecond streaking metrology in Fig.2.7. **b,** Instantaneous intensity of this electric field. The FWHM of it is shown to be $\sim$ 400 as.

Carrier envelope phase decomposition and global phase

Since the concept of CEP is largely understood in the temporal domain, $\varphi_{CE} = \omega_0 \cdot \Delta t_{\text{peak}}$ while Δt_{peak} is time difference between the peak of the envelope and the peak of the

carrier wave of the electric field, the relationship $\mathfrak{F}^{-1}\left[|E(\omega)|\exp(i\cdot(\varphi(\omega)+\varphi_{\omega}^{\text{offset}}))\right] = E_{\text{envelope}}(t)\cdot\cos(\omega_0(t+\Delta t_{\text{peak}}))$ (or $\varphi_{CE} = \varphi_{\omega}^{\text{offset}}$) is true only for pulses longer than ~ 1 cycle. Once the pulses are shorter than ~ 1 cycle, the envelope changes drastically outside the peak so that Δt_{peak} is no longer a good measurement for the phase change of the pulse. As a result, we use from this moment onward the term *global phase* [120, 139] which corresponds to $\varphi_{\omega}^{\text{offset}}$ in frequency domain and holds true for all physical pulses.

Chapter 3

Towards a terawatt scale waveform synthesizer

3.1 Introduction

A lager number of applications in strong field physics would benefit substantially from higher temporal resolution and broader spectral bandwidth of an optical attosecond pulse. However, for applications such as HHG in the keV range, the energy of these pulses must be boosted to the terawatt (TW) levels. Here I discuss efforts toward extension of the light field synthesizer to the TW scale, pushing towards generation of 1 keV photons [140].

3.2 Concept

3.2.1 Supercontinuum generation

Although the topic of supercontinuum generation has been discussed throughly in the book of Alfano [141] and excellent reviews of Dudley *et al.* [142] and Couairon and Mysyrowicz [143], I will only review some important approaches that serve as a foundation for our experiments.

Supercontinuum in hollow core fibers

Generally a broad supercontinuum generation bandwidth ($450 - 2500$ nm, [144] can be obtained from bulk media ([145–152]), filamentation ([143, 144, 153, 154]), conventional fibers and photonic crystal fibers ([142, 155]). Due to nice preservation of the mode, supercontinuum generation in fibers is heavily utilized. However, these techniques are not adequate for intense laser pulses, i.e. the energy of light pulse can be coupled and transmitted is limited to the range of nJ. Therefore, even though short pulses down to 6 fs in 1987 [156] or even 5 fs in 1997 [157] have been demonstrated, their energy was still in the order of nJ.

In order to increase the total output energy as well as to maintain the supercontinuum bandwidth, another technique was put forward 20 years ago. Nisoli *et al.* [158] have demonstrated the generation and compression of 10 fs, 240 μJ from the input pulse of 140

fs, 660 μJ using 140 μm core size, 70 cm long fiber filled with Argon. The idea is that instead of letting the relative weaker pulses to propagate in a solid core (which has very high third order susceptibility), a stronger pulse (which can not be coupled to a medium at the same conditions without causing damage) can be put into interaction with noble gases (a lot less dense - total nonlinearity is less). Moreover, the outer cladding of the fiber serves as a guiding structure. Even though the hollow core fiber does not provide 100 % transmission, one can find out a compromise between the transmitted power and the generated supercontinuum. Because noble gases can sustain very high peak laser pulses, high energy (power) input can be used, thus one can expect high energy (power) output as well. In fact, 5 fs pulses at multi-gigawatt peak power were generated using this technique [128] and eventually our synthesized light pulses [58, 117] benefited heavily from this technique also.

High pulse energy approaches and our selection

However, there is also a limit for the peak energy (and pulse duration) one can use for a hollow core fiber [159]. Generally, the quality of the mode and the transmitted power will degrade if the incident pulse energy is more than 1 mJ. In order to solve this, scientists have implemented another approach where differential pumping scheme [160] is used. Using this technique, pulses with energy $\sim$ 5 mJ (60% conversion efficiency) and a bandwidth of $650 - 900$ nm were generated from $\sim$ 40 fs input pulses and they were compressed to sub-10 fs. Eventually, pulses as short as 3.7 fs (1.2 mJ) were generated using this technique [161].

Nevertheless, the above discussed techniques cannot satisfy the requirements of ultrashort pulses in our experiments: spectrally extending more than two octaves and high power at the same time. In our lab, a hollow core fiber setup without differential pumping has been optimized such that it provides broadest reported spectrum [58, 117] (see chapter 2).

3.2.2 Concept of the TW synthesizer

Figure 3.1 illustrates key ideas of the approach taken here. In the first stage, by setting a goal of getting 50% conversion efficiency for the SHG, the fundamental 3 mJ, 800 nm pulses at $\sim$ 23 fs duration (completely compressed to its Fourier limit, as the leftmost pulse) will be equally divided into two intense pulses, each has $\sim$ 1.5 mJ of energy. Both the fundamental and the second harmonic pulses experience dispersion inside the SHG crystal (BBO in this case), fundamental pulses will be broadened to $\sim$ 28 fs where SHG pulses will be temporally broadened to more than 24 fs, due to the propagation inside the crystal. Because of the limited bandwidth of the SHG conversion (or phase matching curve), the fundamental pulse will experience higher conversion to second harmonic at the center of the spectrum (more depletion at the center rather than on the edges), resulting in a slightly broader effective bandwidth (shorter Fourier limit duration: $\sim$ 22 fs). For the SHG signal, if the fundamental spectrum has a Gaussian shape, one could expect in the weak depletion regime the Fourier limit of the generated SH signals will be $T_{\text{fundamental}}/\sqrt{2}$ where $T_{\text{fundamental}}$ is the Fourier limit of the input pulses. However, since we have a top-hat-like spectrum and the fundamental is strongly depleted, the above rule

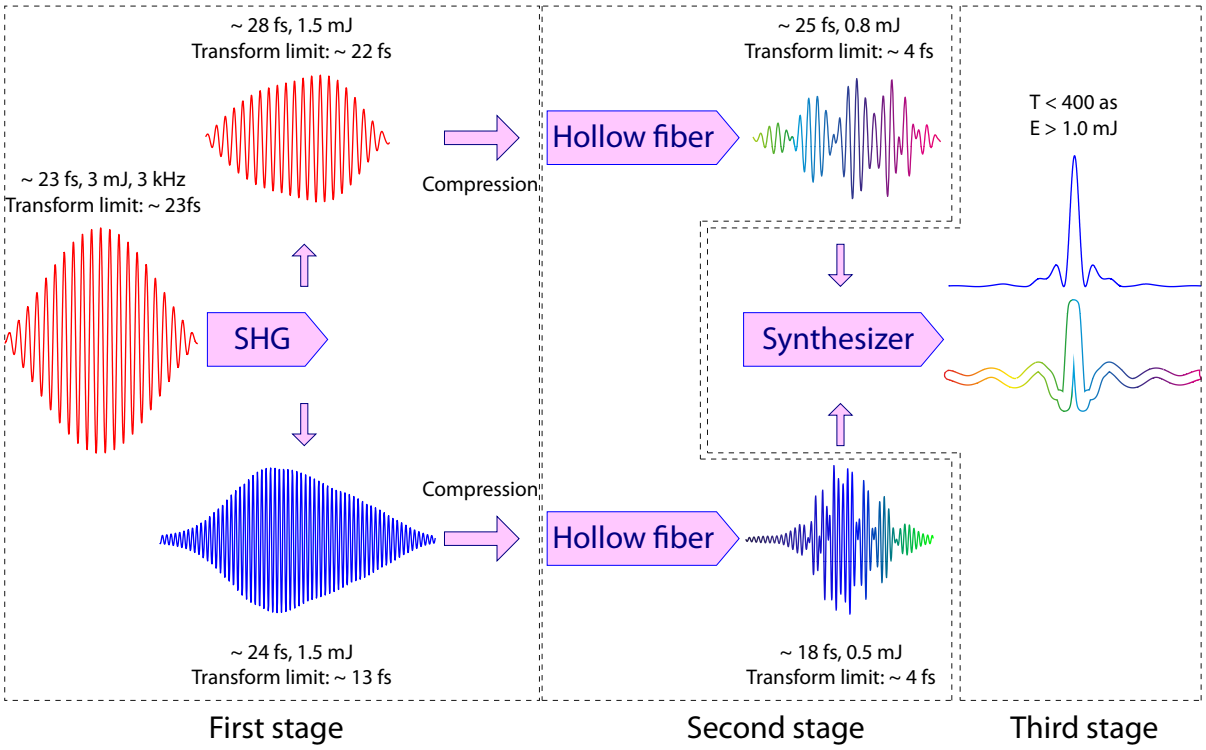

Figure 3.1: Conceptual diagram of the TW light field synthesizer.

does not apply precisely. The resulted SH pulses (bottom left blue pulse) has the Fourier limit of $\sim$ 13 fs.

In the second stage, in order to get an efficient supercontinuum generation from a hollow core fiber, the input pulse must be well compressed. Therefore, two compression stages using chirped mirrors are utilized to this end. After exiting out from the hollow core fibers, since SPM changes instantaneous phase of the electric field without changing its temporal envelope profile, the main part of the generated supercontinuum will have similar temporal duration as the input pulses (close to their Fourier limits).

Finally, in the third stage, the generated supercontinuum pulses from both fibers are fed into the synthesizer. The pulses are divided into different channels and are eventually compressed and merged follow the same methodology as in chapter 2.

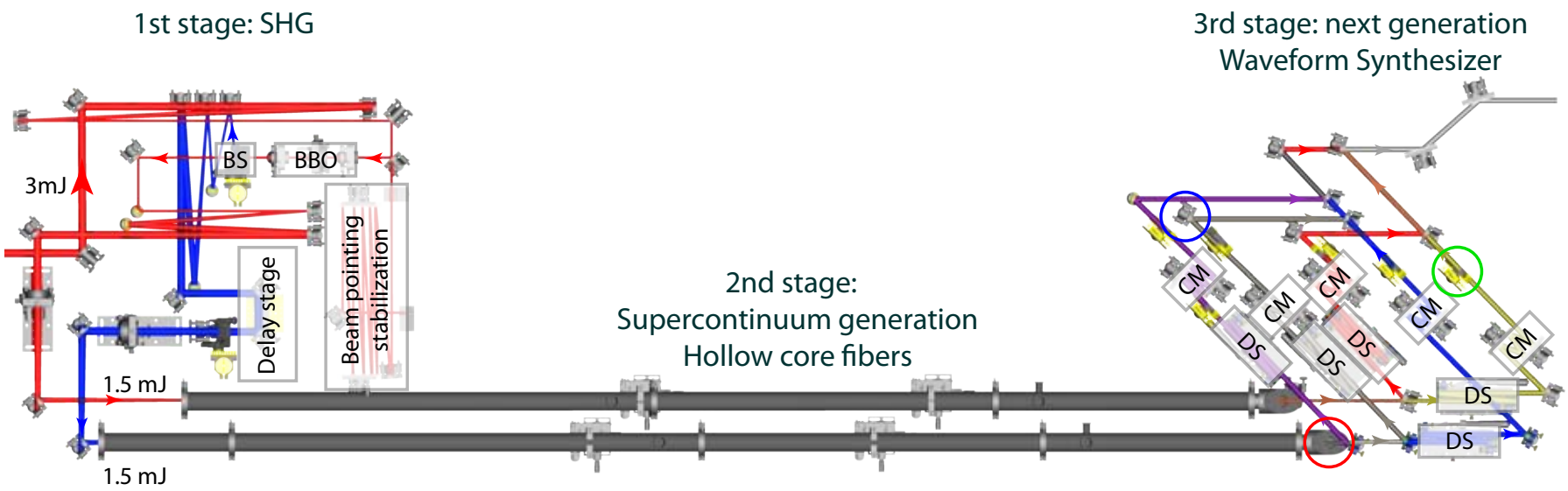

Figure 3.2: 3D mechanical design of the TW light field synthesizer. BBO: Beta Barium Borate crystal used for SHG. BS: Beam Splitter. DS: Delay Stage. CM: Chirped Mirrors stack. Red, green and blue circles mark the devices that will be the focus of Fig. 3.3.

Implementation of the design to 3D mechanical drawing

Figure 3.2 illustrates a top view perspective of the design which shows three stages of the apparatus as in the schematic diagram (Fig. 3.1). The first stage of this system is actually the grayed part in Fig. 2.1 (top right). The total optical length of the system is more than five meters. The experimental implementation follows closely this 3D design.

A number of technological advances have been implemented in this system. We can only describe some representative ones, as illustrated in Fig. 3.3:

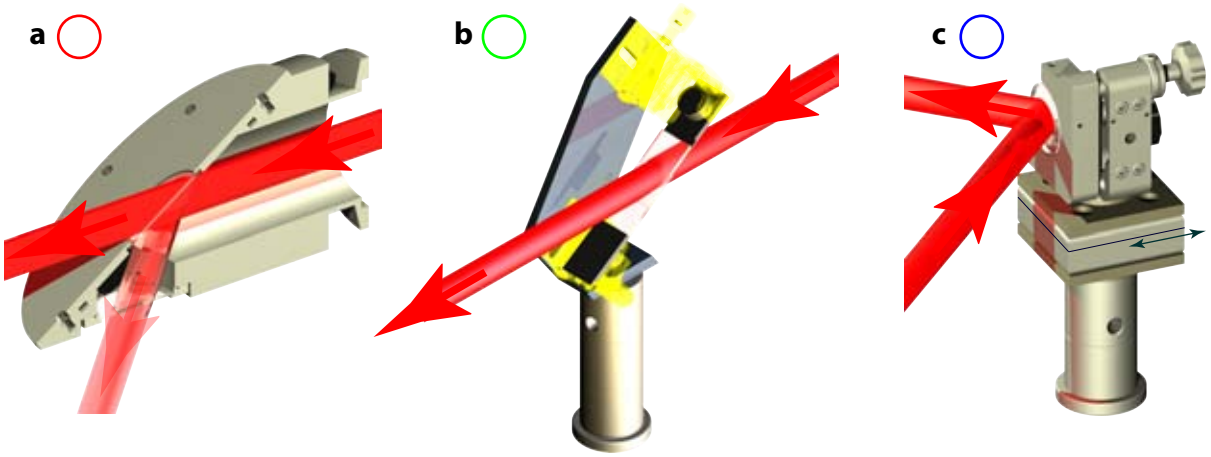

Figure 3.3: 3D design: some technological advances. a, Output window of the hollow core fiber setup at Brewster's angle. **b,** Wedge pair and translation stages placed at Brewster's angel. **c,** Temporal delay stage in minimalist design.

- **Brewster's angle exit windows - Fig. 3.3a** Because the Brewster's angle does not vary much for the whole bandwidth ($\sim$ 270 to 1100 nm) for either BK7 or Fused Silica glass material ($\varphi_B = 56 \pm 1°$), the pulses will be almost completely transmitted through the window as in Fig. 3.3a for vertically polarized field. Any fraction of the beam which is not completely transmitted and exits through a separate part will be utilized for the CEP stabilization of the slow loop (amplifier and fiber setup).

- **Wedges pair and translation stages - Fig. 3.3b** This wedge pair is designed such that there is almost no reflection of the individual beams on the wedges pair for the S-pol beam. This design also incorporates translation stages to optimize the compression of pulses in the channels as well as their CEPs, and the same design is used without modification to host electronically controlled translation stages for fine tunning of relevant parameters.

- **Simplification of a delay stage - Fig. 3.3c** Instead of a 45° angle of incidence (AOI) design incorporating a translation stage, in our new design, the mirror mount is placed directly on Piezo stage which is hosted on a pedestal post. Because most of the temporal delays required are in fs range (or the order of μm), even when the AOI $= 45°$, a temporal delay of 10 fs corresponds to $\sim 3\,\mu$m and it means a spatial displacement of $\sim 3\,\mu$m of the reflected beam, which is negligible.

3.3 Highly efficient second harmonic generation and its compression

Ever since the demonstration of the first second harmonic generation (SHG) in a bulk [162] and surface [163] of crystals, owing to the creation of the first laser [2], SHG has been widely utilized not only in fundamental sciences but also in industrial applications. Even though very high efficiency of SHG has been demonstrated, up to 92% for 30 ps pulses [164] long time ago, attaining high conversion efficiency for shorter pulses is a lot more difficult because of the phase matching requirements [75, 165] for coherent build-up of the up-converted light.

Selection of proper birefringent crystals' parameters could mitigate the group velocity mismatch (GVM) due to dispersion at short pulse regime, nonetheless, in order to obtain a broad bandwidth in SHG, one has to minimize the propagation length of the beam inside the crystal. Consequently, the total flux build-up (or conversion efficiency) is compromised. Several schemes have been proposed to overcome the phase matching limitations. They can be classified in two groups based on their nature of phase matching corrections . In the first group which we call passive phase matching correction, because of the existence of various dispersion characteristics of birefringent crystals, there exists combinations of crystals and wavelength ranges in which essentially the GVM is zero over those spectral ranges. This is demonstrated in numerous experiments with wavelengths from $1 \rightarrow 1.5\,\mu$m [166–168]. Recently, $\sim 55\%$ conversion efficiency has been demonstrated for $\sim$ 200 fs pulses using this technique [169]. The second group which we call active phase matching correction is based on different geometries used to counter the wavelength dependent refractive index that exists inherently. This group include achromatic phase matching [170–172] and tilted quasi-phase-matched gratings [173] or multicrystal designs [174].

Even though in principle, the techniques of active phase matching can work for an arbitrary wavelength range, they require complex experimental setups, as well as, very careful alignment (one can get huge angular and spatial chirp from this kind of arrangement). Passive phase matching techniques require the existence of the crystal at the given wavelength, for our case ($\sim$ 800 nm) no crystal has been reported with the high second order susceptibility. And overall, the total conversion efficiency of active phase matching techniques is not very large because of many optics required. Generally, the conversion efficiency is in the range of $\sim 20 \rightarrow 30\%$ [175, 176] for femtosecond pulses less than $\sim$ 30fs. For achromatic broadband phase matching, the total efficiency is typically lower ($\sim 10\%$ [177]).

In this setup, highly efficient SHG is essential for implementation of the scheme of Fig. 3.1. We implement the SHG using the direct approach, without utilizing any of the active or passive phase matching correction schemes. Theoretical consideration suggested that we experimentally approached the high conversion efficiency reported to date.

3.3.1 Efficient conversion efficiency: experimental results

Implementation and requirements

The first requirement for an efficient SHG setup is also the one easily to be overlooked: spatial profile of the fundamental beam. Due to the inhomogeneity of the Ti:Sapphire crystal as well as imperfections of transporting mirrors, the beam profile delivered to experiments often has non-Gaussian shape and small diffraction rings. By changing the design of the 2nd amp from one pass to two passes (done by Femtolasers), the single pass gain amplification has been relaxed a lot. Eventually this led to a reduced pumping power, almost negligible thermal lensing and the output beam profile is practically Gaussian while maintaining the final output energy of $\sim$ 3 mJ per pulse. The output instability increased but this is easily compensated by the beam pointing stabilization setup placed after the 1st amp, before the 2nd amp.

The second requirement is an adequate temporal compression of the fundamental pulses. If these pulses are not well compressed, different spectral components of a pulse do not come at the same phase (also same moment in time), and as the result the three wave mixing process or SHG is not efficient. Practically in the lab, we compress our pulses to $\sim$ 23 fs which is virtually their Fourier limit duration.

Because the intensity needed for SHG must be of the order of $\sim 10^{12}\, W/cm^2$, for our pulses of $\sim$ 23 fs, $\sim$ 3 mJ this implies a beam size on the BBO of the order of several mm. It means that a converging scheme must be implemented. Although a walk-off effect is negligible in our case (the thickness of the BBOs is maximum $\sim 200\,\mu$m), the phase matching angle is crucial. The phase matching angle varies from $31.2 \rightarrow 27.4°$ for the center wavelength from $750 \rightarrow 850$ nm. This 3.8° is already the maximum angle (from side to side) of a cone formed by focusing a beam whose width is $\sim$ 7 mm by a lens whose focal length is of 1 m.

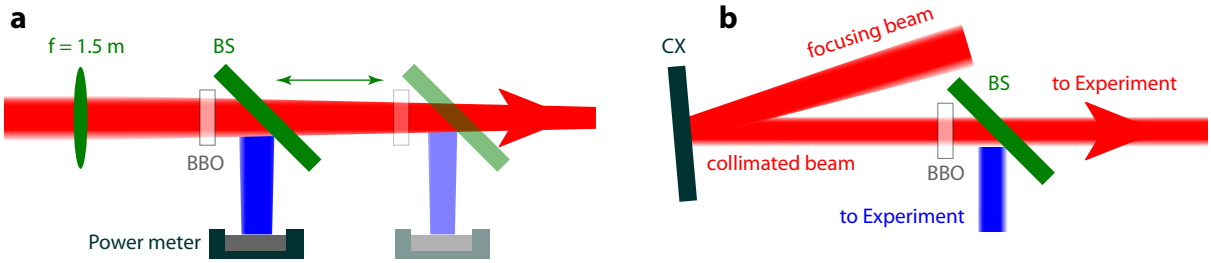

Figure 3.4: Experimental setup. **a,** Experimental setup used gentle converging beam scheme to attain optimal intensity on BBO. CX: Convex mirror (used to collimate the focusing beam). The complete setup of BBO, BS and power meter and be translated horizontally. The lens is placed for illustration only, in reality, mirror focusing is used to minimize dispersion. **b,** Experimental setup providing collimated beam hitting the BBO.

Fig. 3.4 shows the setup used to optimize the conversion efficiency of the SHG. Not only the phase matching is critical in this case but also the higher-than-second order susceptibilities must be minimized. If the laser intensity inside the crystal exceed a certain threshold, besides SHG, third order effects will not be negligible and will give rise to white light generation, and self focusing, etc. Therefore in order to make the most out of SHG, all other effects has to be as small as possible. By utilizing the setup in

Fig. 3.4a, optimal exposure intensity ($\sim 10^{12}$ W/cm^2) is found whose beam diameter is slightly less than 7 mm.

After knowing the suitable beam size (or incident intensity) of the beam on the BBO, we replaced the optimizing setup by the collimated beam setup (Fig. 3.4b) which has two advantages: the BBO can be flexibly positioned, the collimated beam exiting the BBO does not cause any problem for the BS or any optics afterward.

Summary of the results

The BBO crystals (200 μm, cut at $\theta = 29.1°$) are customized to have the width $\sim$ 15 mm square shape. Under the above optimized condition, $\sim$ 4.48 W of the SHG was detected behind the dichroic and the reflecting mirror. With power of the fundamental is $\sim$ 9.10 W (3 kHz, $\sim$ 3.03 mJ, measured 9 reflections on high reflectivity mirrors before arriving on the BBO), the **measured conversion efficiency is** $\sim$ 49%. If we take into account imperfections of the dichroic and reflecting mirrors, the effective conversion efficiency is $>$ 50%. To the best of my knowledge, this is a record SHG conversion efficiency from $\sim$ 23 fs pulses.

For thinner crystals such as 100μm BBO, the **maximum conversion efficiency is about** $\sim$ 39% at the same configuration of incident pulses.

The high conversion efficiency comes at the same time with a SH beam of good spatial profile. In fact, increasing the focusing intensity (by decreasing the beam size on the BBO) could increase slightly the total SHG conversion efficiency, but the transmitted fundamental beam develops a hot spot at the center, practically limiting potential use of it.

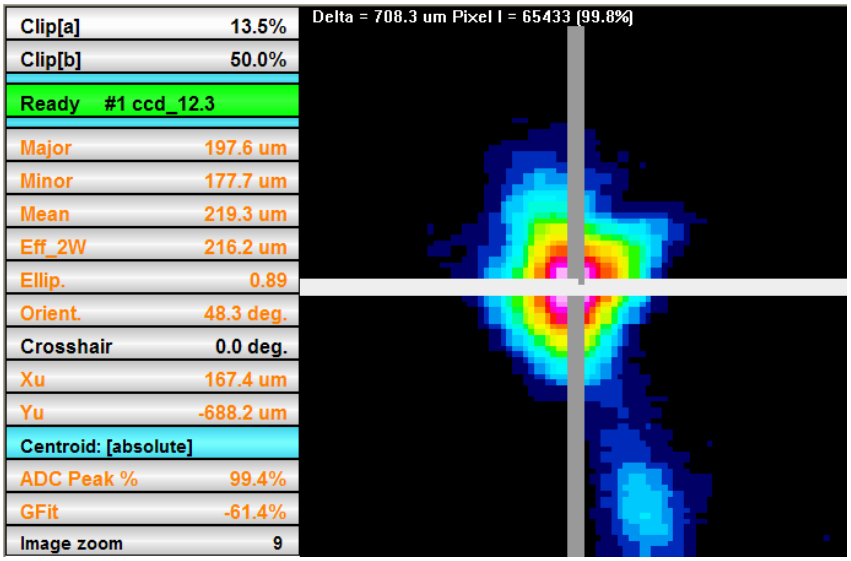

Figure 3.5: Focused SHG spatial profile at highest conversion efficiency. The generated SHG beam is focused by a mirror with focal length of 2.0 m.

Fig. 3.5 shows a well behaved beam profile of the SHG at the focus with ellipticity of $\sim$ 0.89. In conclusion, the setup provides highest possible SHG conversion efficiency while maintaining good spatial profile of both the fundamental and the SH beams.

3.3.2 Temporal characterization and compression

Compression of the fundamental pulses after SHG

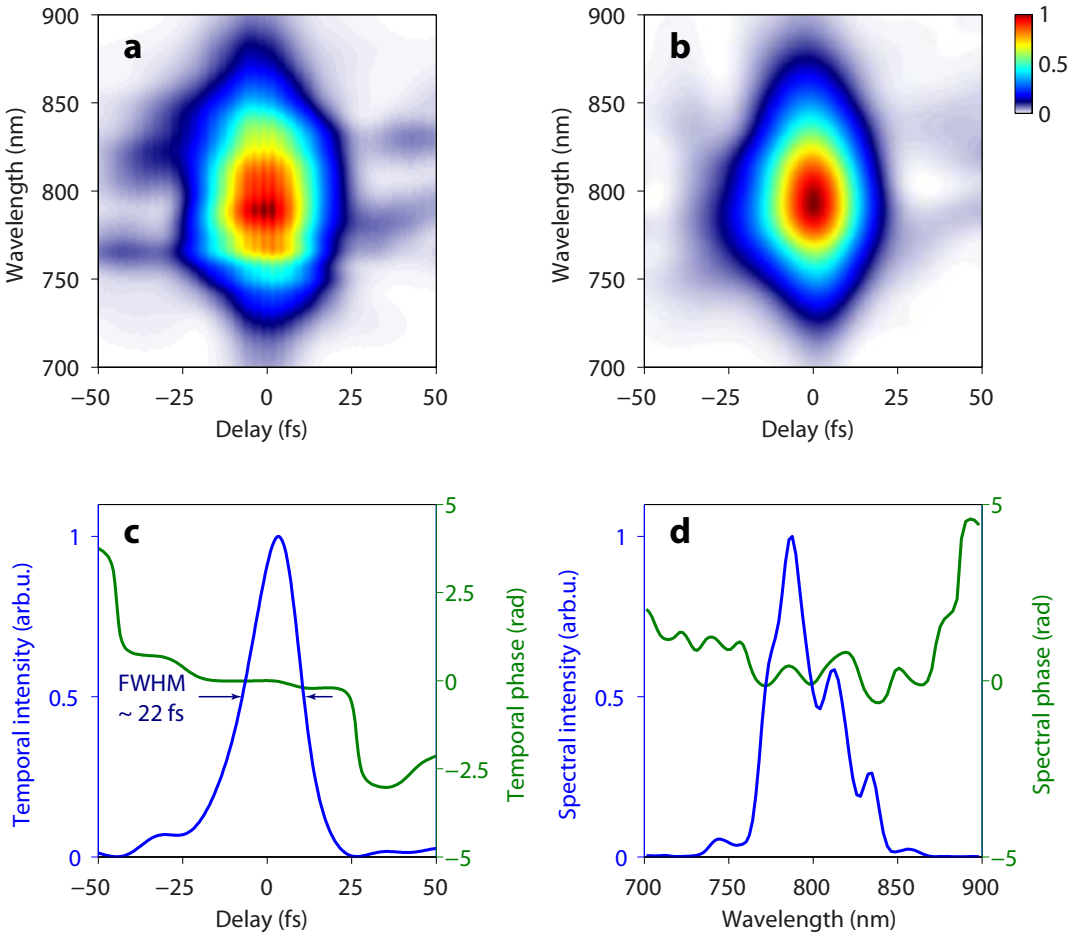

Figure 3.6: FROG measurement and reconstruction of the fundamental pulses existing the BBO. a, Measured FROG spectrogram. **b,** Reconstructed FROG spectrogram. **c,** Reconstructed temporal intensity profile and temporal phase. **d,** Reconstructed spectral intensity profile and spectral phase.

The fundamental pulses leaving the BBO and before entering the fiber compressor, propagate through various media: 200 μm BBO (broaden the pulses to $\sim$ 28 fs), $\sim$ 1.2 mm inside the BS (thickness of the BS: 1 mm) which has GDD $\sim$ 43 fs^2, 2 mm lens (GDD $\sim$ 72 fs^2), 0.5 mm window in front of the fiber housing (GDD = $\sim$ 18 fs^2) and finally about 3 m of propagation in air (GDD = $\sim$ 64 fs^2). As a result, the total effective GDD that the pulses have accumulated after the BBO is $\sim$ 460 fs^2 which in the end totally broadened the pulses from $\sim$ 21 fs (transform limit) before the BBO to $\sim$ 80 fs before the entrance of the fiber.

Similarly to SHG, in order to have an efficient supercontinuum generation, it is important to optimize these pulses to their Fourier limit. In this case, a simple combination of chirped mirrors and pair of wedges could allow a good compression of the pulses' temporal profile. Fig. 3.6 shows a typical example. The reconstructed spectrogram (Fig. 3.6b)

		Fused silica 1 mm	BK7 1 mm	MgF_2 1 mm	Air 1 m
GDD (fs^2)	400 nm	97.4	121.8	50.0	49.4
	800 nm	36.1	44.6	19.8	21.3
TOD (fs^3)	400 nm	30.0	40.4	14.1	14.5
	800 nm	27.4	32.0	13.7	19.8

Table 3.1: GDD and TOD values for typical optical media.

closely resembles the measured spectrogram (Fig. 3.6a). The pulses are compressed to nearly Fourier limit duration (Fig. 3.6c) and their spectral phase exhibits tiny GDD and negligible higher order chirp.

Compressions of the SH pulses

Compression of the SH fields is in principle more challenging than the compression of the fundamental ($\sim$ 800nm) pulses because of high dispersion and less developed pulse compression techniques in this spectral range. Fig. 3.1 shows high order dispersion values for typical optical media.

Because the SH pulses have to propagate through 0.5 mm of Fused Silica window after the BBO and $\sim$ 3 m of propagation in Air, in total, the SH pulses will acquire a GDD of$\sim$ 320 fs^2 after the BBO ($\sim$ 100 fs if left uncompressed).

Fig. 3.7 illustrates compression of the temporal profile of the SH fields by chirped mirrors optimized for this spectral range. The measured spectrogram (Fig. 3.7a) and reconstructed spectrogram (Fig. 3.7b) show good agreement. The compressed pulses are almost chirp free (their Fourier limit is $\sim$ 13 fs). Such pulses with duration of $\sim$ 13 fs and energy of $\sim$ 1.5 mJ at 3 kHz are of significant value in ultrafast sciences and also beyond the scope of this thesis.

During performing above experiments, we observed nonlinear response of the chirped mirrors. All the details in this work exceed the scope of this thesis and they are covered in another publication [178].

3.3.3 Theoretical investigation of second harmonic generation efficiency

The fast pace of the development of personal computers has brought tremendous advantages to numerical modeling. Nowadays, a large number of simple physical simulations are tractable on a single computer and they have brought great supports to experiments in terms of intuitive understanding as well as systematic optimization of the processes. Even though for light pulse propagation and interaction with media, one can solve the complete Maxwell's equations directly [179–181] but this is often computationally demanding and provide somewhat limited physical intuitive picture. Practically in order to have nonlinear effects, one has to involve strong electric fields which are not possible to attain with continuous waves. The decomposition of the light pulse into its envelope and phase [182, 183] allowed the use of *slowly varying envelope approximation* (SVEA)

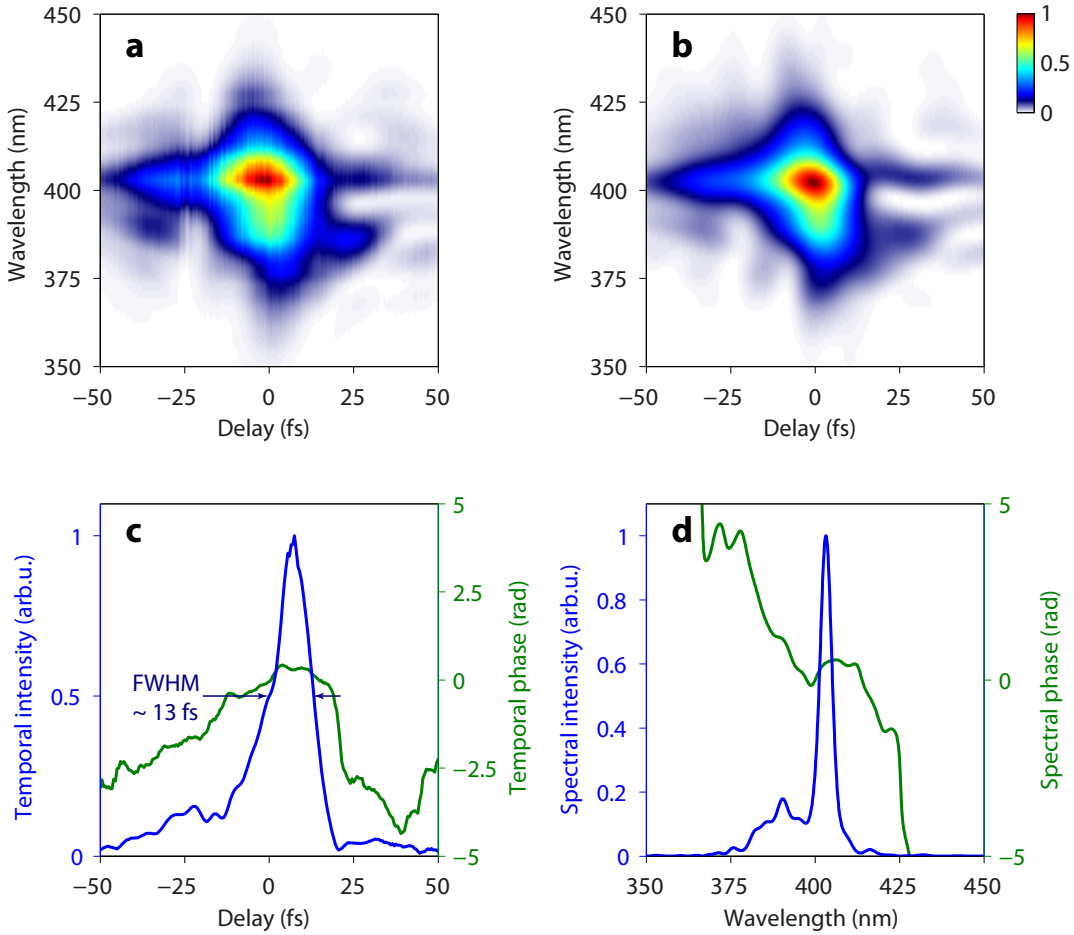

Figure 3.7: FROG measurement and reconstruction of the SHG pulses existing the BBO, before the fiber. **a,** Measured FROG spectrogram. **b,** Reconstructed FROG spectrogram. **c,** Reconstructed temporal intensity profile and temporal phase. **d,** Reconstructed spectral intensity profile and spectral phase.

[183]. In this approximation, the differential propagation equations are reduced from second order to first order which greatly improves the calculation time. Furthermore, Brabec and Krausz [184] derived another approximation which is called *slowly evolving wave approximation* (SEWA) and later more approximations are derived [185, 186]. A comprehensive review and derivation of all of these approximations is provided in a great article by Couairon and Kolesik *et al.* [187].

Although the wave equation comprises all the needed information for propagation of waves in media, in order to take into account response of the media upon interaction with light waves (SHG in this case), one has to apply the polarization creation terms into the wave equation and propagate them. Following [188], we derived the nonlinear coupled wave equations (more details in Appendix A) which describe the interactions of light matter in uniaxial second order nonlinear materials and investigate their application to our experimental data.

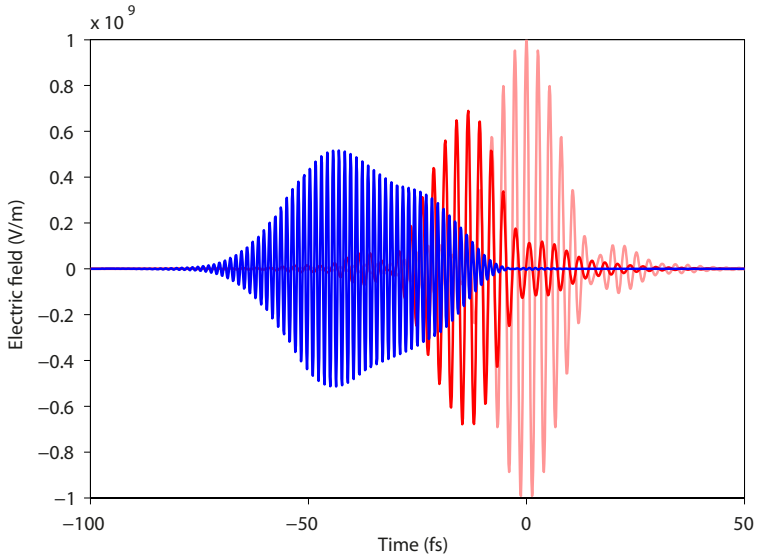

Figure 3.8: Pulse propagation inside 200 μm BBO. The incident electric field (solid light red curve) is a chirp free pulse from a 80 nm bandwidth of a hyper Gaussian spectrum centering at 800 nm. $\theta = 29.1°$ $\varphi = 90°$. The peak incident electric field was set at 10^9 V/m (inside the crystal). The depleted electric field after propagation (still in *ordinary* axis) is illustrated as the solid red curve. The generated SH pulse (*extraordinary* axis) is depicted as the solid blue curve.

Simulation results

Figure 3.8 shows the results (generated SH pulses, depleted fundamental pulses, and incident fundamental pulses) of the pulses exiting the last slice of the medium after 200 μm propagation inside BBO. Because dispersion in the medium and the fact that new SH photons should be generated at the temporal center of the fundamental fields (where electric field amplitude is highest), after some distance, the pulses are broadened to such and extent that the temporal center of the SH and fundamental pulses no longer overlap. The phase matching between the fundamental and the SH pulses is therefore weaker, resulting in reduced generation of SH field in the next slices. As a result, after 200 μm of propagation inside the BBO, although the SH pulses accumulated significant energy from the incident pulses, leading to a serious depletion of the fundamental pulses, the SH conversion efficiency starts to saturate.

With the use of absolute numbers representing the effective second order nonlinearity of BBO [75, 189], absolute conversion efficiency can be calculated and represented in Fig. 3.8. In order to take into account the real beam parameters (beam size, energy per pulse, temporal profile), one might think of a complete 3D propagation of the wave equation for the exact calculation. However, the beam size is substantially large ($>$ 5 mm) and the propagation distance is short (several 100 μm), the complete 3D wave equation could be rewritten as a series of independent equations (Eq. A.12) where the peak electric field maps the spatial beam profile.

Such a simulation result is illustrated in figure 3.9. For each crystal thickness, a very dense grid of maximum peak intensities is generated and corresponding propagations are performed. The results are mapped on a Gaussian profile and subsequently the absolute

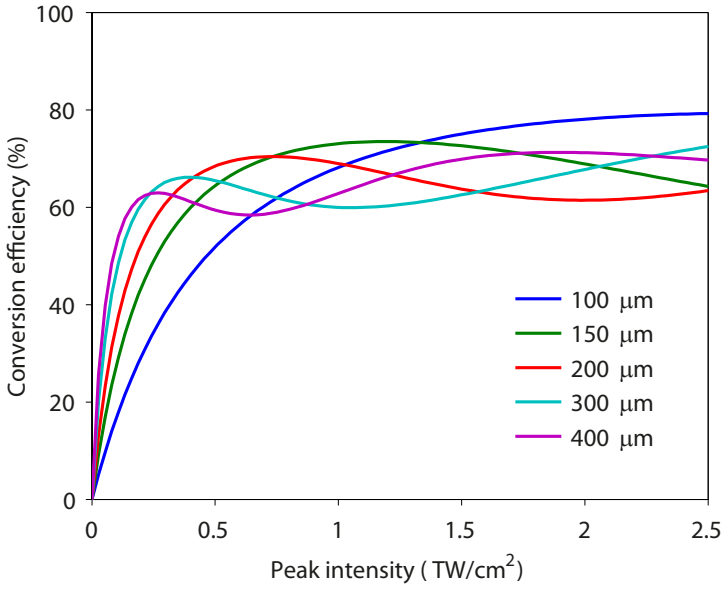

Figure 3.9: Calculated SHG conversion efficiency. A Gaussian beam profile is assumed. Maximum intensities here are intensities at the center of the beam inside the medium.

SHG conversion efficiency is calculated. In fact, using this technique we can calculate the exact SHG conversion efficiency for the exact beam profile. However, since the measured spatial beam profile fits very well by a Gaussian, simplification of the full problem to a cylindrically symmetric problem greatly improved the calculation time.

For our experimental parameters of the beam before hitting the BBO: peak electric field $\sim 2.2 \cdot 10^9$ V/m $\rightleftarrows$ $I_{\text{peak}} \sim 1.3$ TW/cm^2, the beam profile is ~ 7 mm at $1/e^2$ and the energy per pulse is ~ 3 mJ, the parameters of the electric field at the center of the beam, right in the first slice of the BBO are: peak electric field $\sim 1.7 \cdot 10^9$ V/m $\rightleftarrows$ $I_{\text{peak}} \sim 0.77$ TW/cm^2. Fig. 3.9 explains nicely the achieved high conversion efficiency. At ~ 0.77 TW/cm^2, only the 150 and 200 μm crystals provide the maximum SHG conversion efficiency. For thin crystal (100 μm), the conversion efficiency seems to increase as long as the peak intensity increases. For thicker crystal, it could result in higher conversion efficiency at lower peak intensity. However, they also reach saturation much earlier than thinner crystals. Therefore, the focusing intensity has to be chosen such that it is just enough to get maximum conversion efficiency but also it is not too high to cause higher order nonlinear effects.

From Fig. 3.9, two small deviations of the simulation from experimental results can be observed: firstly, it seems that a weaker peak intensity could provide even higher conversion efficiency and at the same time relaxes the focusing conditions. Secondly, the theoretically calculated conversion efficiency is close to $\sim 65\%$ while in the experiment we could not observe it. However, if one takes into account the inaccuracy of the reported nonlinear susceptibility values of BBO, the imperfection of the real BBO and of the fundamental beam, this is already an excellent agreement. We could optimize the crystal thickness and focusing intensity even more to reach the theoretical upper limit as illustrated in the above figure.

From the calculation of the SHG conversion efficiency, we notice that besides the

properties of the crystals and the peak intensity at the center of the beam, the total conversion efficiency does not depend on the beam size, but it depends on the beam shape. As a result, one could optimize the conversion efficiency based on above criteria: change the spatial profile so that it is more top-hat than Gaussian, change the beam size while keeping the maximum peak intensity (this is very crucial for high energy pulses).

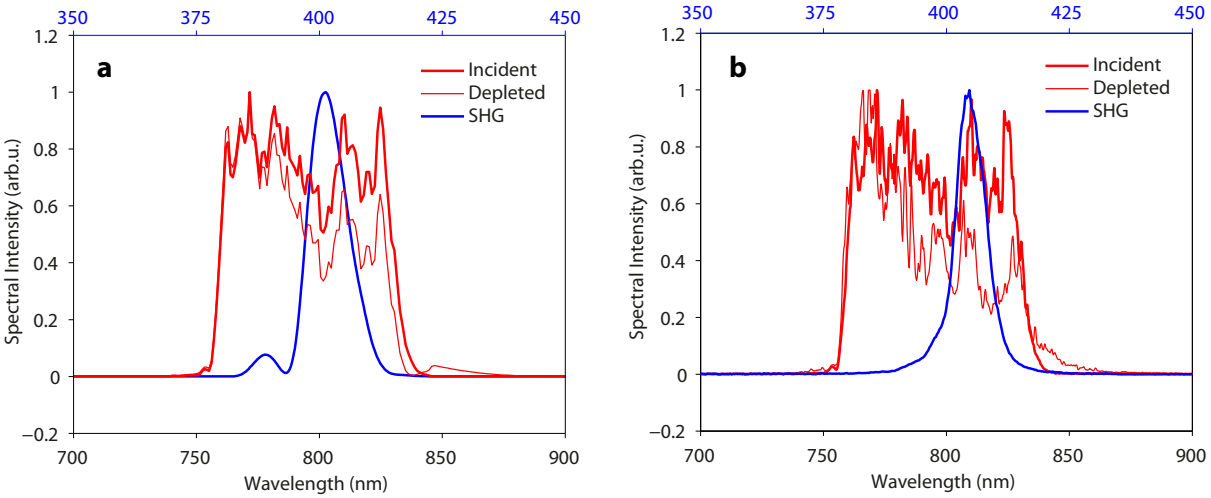

Figure 3.10: Comparison of simulated and measured spectra. a, Simulated spectra are annotated correspondingly by their color codes in the legend. The axis of the SHG spectrum is displayed on top. **b,** Same as **a,** but these are the measured spectra.

In addition, we could also compare the measured spectra with the simulated spectra as in Fig. 3.10 where a strong agreement is observed.

Firstly, one can observe easily the depletion of the fundamental spectrum after propagation through 200 μm BBO. Since the crystal is not infinitely thin thus the phase matching curve has a limited bandwidth. For such a thickness, the phase matching curve is narrow enough such that at the end of the propagation, the frequencies at the center of the fundamental spectrum got up-converted much more than frequencies at the wings, resulting in a depleted spectrum with a dip at the center. This dip virtually broadens the effective bandwidth of the fundamental so that its Fourier limit is slightly shorter.

Secondly, three wave mixing process here gives rise to the creation of the wings of the fundamental spectra (clearly seen around $\sim$ 850nm) for both measured and simulated spectra. In this particular case, back conversion process (the term $\mathfrak{F}\left[\mathfrak{F}^{-1}\left[\mathbf{E}_x(\omega)\right] \cdot \mathfrak{F}^{-1}\left[\mathbf{E}_y(\omega)\right]\right]$ in the Eq. A.12) is responsible for this.

Thirdly, the generated SHG pulse develops small wing in the high frequency side (more in the simulation, less in the measurement) which could partially be explained from the off-center phase matching angle. Since changing θ from 29.1° to 31.2° can change the center phase matching wavelength from 800 to 750 nm. It means that in order to get correct phase matching angle to within $\pm$10 nm of the center wavelength, the precision of θ has to be $\sim$ 0.4°. Practically any slight imperfections of the crystal could compromise the performance of the BBOs.

In conclusion, excellent agreement between simulation and experimental measured results has been observed. This simulation serves as an important tool in interpreting

the experimental results and also helps us to perform systematic optimization of the SHG process.

3.4 Supercontinuum generation and their compression

3.4.1 Supercontinuum generation

Optimization

There are several important parameters that are needed to be tuned in order to get an efficient supercontinuum in a fiber:

- **Fiber core size:**
  Supercontinuum generation in gases requires certain range of intensity (several 10^{14} W/cm^2) therefore a given pulse energy, duration will correspond to a given beam size. For example, a Gaussian, 20 fs pulse at 800 nm with energy of 1 mJ will reach $\sim 6 \cdot 10^{14}$ W/cm^2 at the focusing size of $\sim 200\,\mu$m ($1/e^2$). The fiber core size will be chosen such that it supports transmitted mode as well as high power at maximum spectral broadening.
  In our lab, using similar parameters as the above pulses, the fiber core size is optimized to be $\sim 250\,\mu$m for the fiber used to broaden the fundamental beam (red fiber) previously. Since the pulse energy is improved to $\sim$ 1.5 mJ, the focusing conditions do not change much, we also have optimal supercontinuum generation with $\sim 250\,\mu$m core size fibers.
  For the hollow core fiber used to broaden the SH pulses (blue fiber), we found out that among all the core sizes tested (160 μm, 200 μm, 250 μm, 300 μm, and 400 μm), the 200 μm core size gave the best result in terms of spectral bandwidth and quality of transmitted mode and high power.

- **Gas type:**
  There is also a compromise between the third order susceptibility and other effects: usually a molecule will have significantly stronger third order susceptibility compared to a noble gas (see Fig. 3.11a for a comparison between SF6 and Neon). However, it also has a lot higher probability of ionization, absorption, etc such that for the same broadening (Fig. 3.11a), using Neon will give us almost three times higher transmission compared to SF6. It means that absorption, ionization, etc, are a lot more serious in SF6 rather than in Neon in the same experimental conditions. Consequently, one has to try experimentally (it is hard to put all of these effects into a simulation) and we found out that Neon is a good option for supercontinuum generation in both fibers.

- **Gas pressure:**
  Fig. 3.11b shows the dependence of supercontinuum generation at different pressure for Neon. It is trivial that the higher the gas pressure is, the higher chance third order effects will set in thus one can expect the effective bandwidth to increase as the gas pressure increases. Nonetheless, there exists a pressure at which absorption

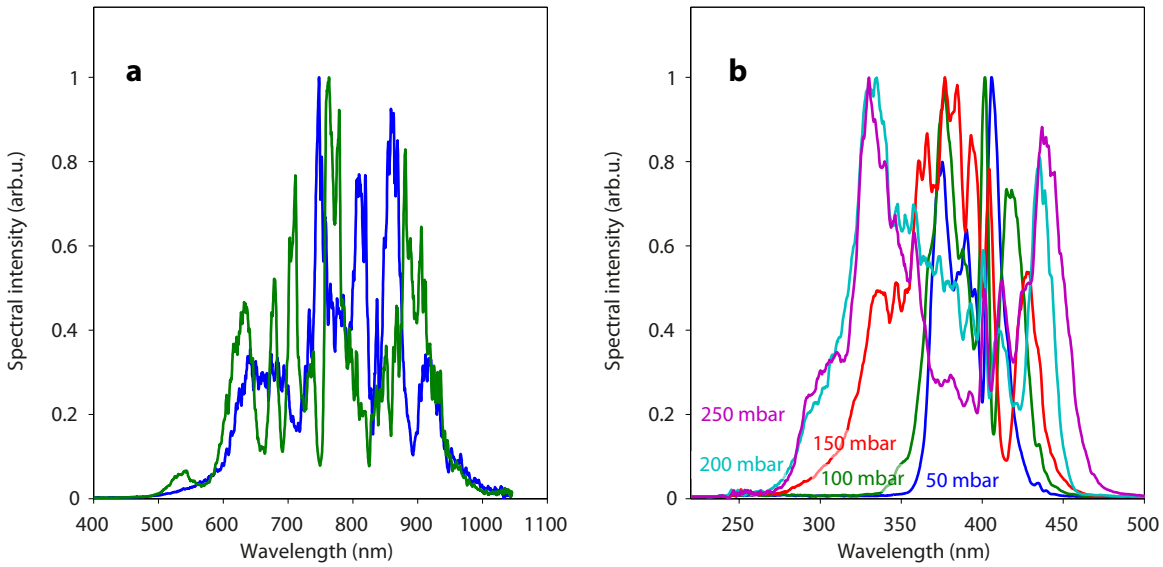

Figure 3.11: Supercontinuum generation dependence on gas type and pressure. a, Supercontinuum spectra measured behind the red fiber filled with 2 bar of Neon (solid blue curve) or filled with 200 mbar of SF6 (solid green curve). **b,** Supercontinuum spectra measured behind the blue fiber filled by SF6 with increasing gas pressure (50 → 250 mbar).

starts to be crucial, the transmission through the fiber drops dramatically and the mode deviates strongly from the TEM_{00}. Therefore, the gas pressure has to be optimized carefully along with the other parameters.

Results

Fig. 3.12 shows the optimized output spectra. The spectrum of the blue fiber extends from $230 - 500$nm and it supports a pulse with duration of ~ 1.5 fs. To my knowledge, this is the broadest supercontinuum generation recorded by seeding the hollow core fiber with the SH pulses of the 800 nm fundamental pulses. Additionally, the spectrum of the red fiber extends from $500 - 1050$ nm and it supports a pulse with duration of ~ 2.6 fs.

3.4.2 Division of the channels

We intentionally divide the current synthesizer into 5 channels which have almost equal bandwidth (in frequency). The starting wavelength is 220 nm (this is almost the limit of UV absorption in air) and the end wavelength is 1500 nm (where limited spectral broadening can be detected at this side of the spectrum). As a result, the channels are divided as follows: starting from $220 - 270$ nm (Ch0), from $270 - 350$ nm (Ch1), $350 - 500$ nm (Ch2) which are all generated by the blue fiber (bottom fiber setup in Fig. 3.1); $500 - 670$ nm (Ch3), and lastly $670 - 1500$ nm (Ch4) which are generated by the red fiber (top fiber setup in Fig. 3.1).

Placing the barrier at 500 nm between the two fiber setups not only makes use of the long wavelength components generated from the blue fiber (input pulses are SHG pulses) but also relaxes the supercontinuum generation of the red fiber (input pulses are

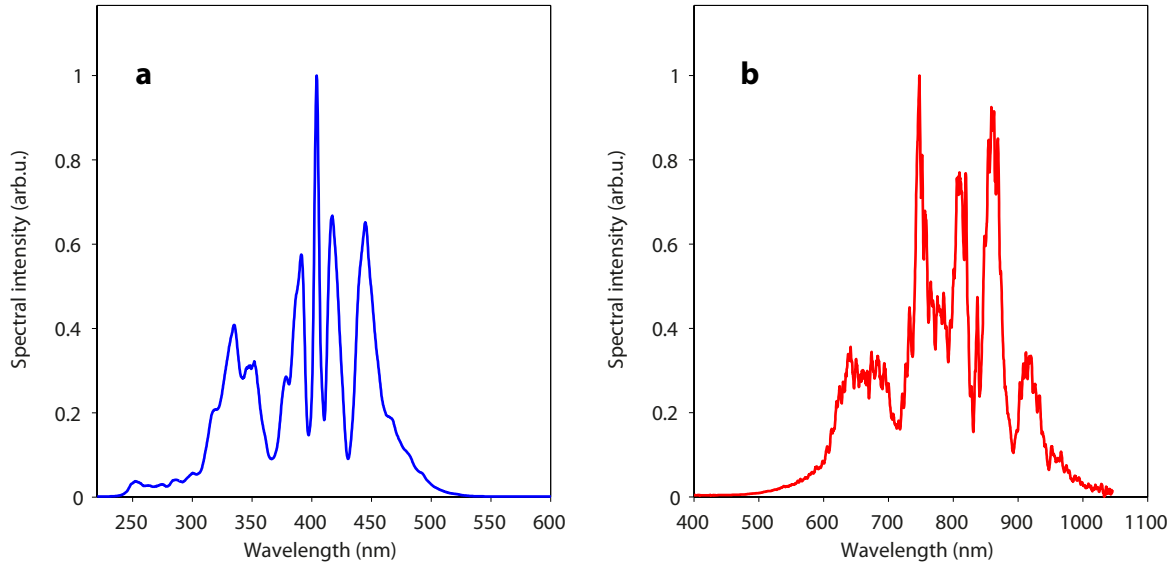

Figure 3.12: Supercontinuum generation behind the red (800 nm input puses) and blue (400 nm input pulses) fiber. a, Optimized output spectrum behind the blue fiber. **b,** Optimized output spectrum behind the red fiber.

fundamental 800 nm pulses). By having less gas pressure (higher gas pressure was needed to generate wavelengths down to $\sim$ 270 nm), this relaxation will give a trivial boost to the transmission of the beam while maintaining a good spatial profile.

3.4.3 First steps in the compression of pulses in the channels

A successfully built synthesizer setup requires adequate compression of the individual channels, temporal and spatial overlap as well as their synchronization (or stabilization) units as discussed in chapter 2. In principle, the temporal, spatial overlap, and synchronization (stabilization) units are designed very similarly to the previous generation of synthesizer. What is very critical here is the compression of the pulse in the 5^{th} channel ($220 - 270$ nm) which is challenging and never explored before.

Compression of pulses in the channel 3 and 4

The FROG measurements for pulses in each channel are measured and correspondingly compensated. For channel 4 and 3 (from $670 - 1500$ nm and from $500 - 670$ nm), compression was effective with well established multilayer technologies [1]. The temporal profiles of pulses in the channels are approximately compressed close to their Fourier limit durations. Fig. 3.13 and Fig. 3.14 show the results of the dispersion compensation where the pulses are compressed to $\sim$ 7.8 fs and $\sim$ 6.9 fs whereas their Fourier limits are $\sim$ 6.7 fs and $\sim$ 6.0 fs respectively.

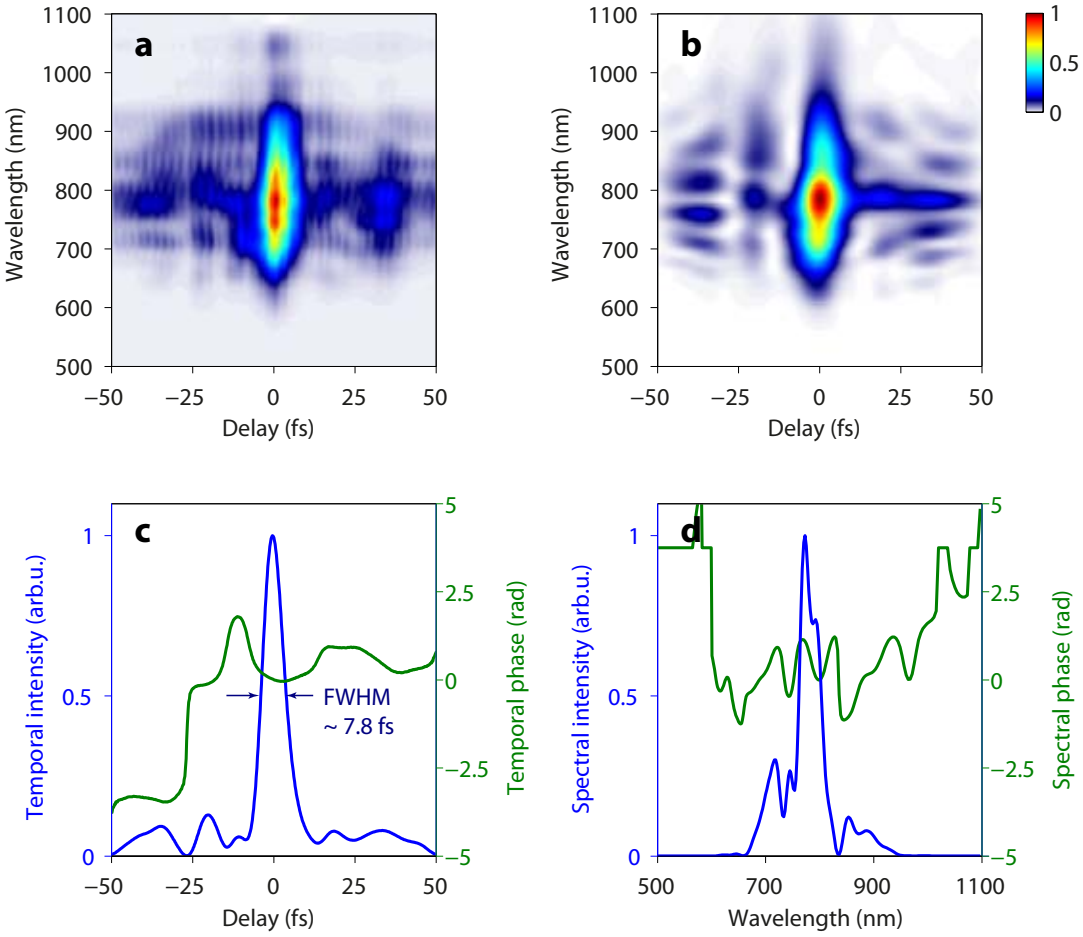

Figure 3.13: FROG measurement and reconstruction of pulses in channel 4. a, Measured FROG spectrogram. **b,** Reconstructed FROG spectrogram. **c,** Reconstructed temporal intensity profile and temporal phase. **d,** Reconstructed spectral intensity profile and spectral phase.

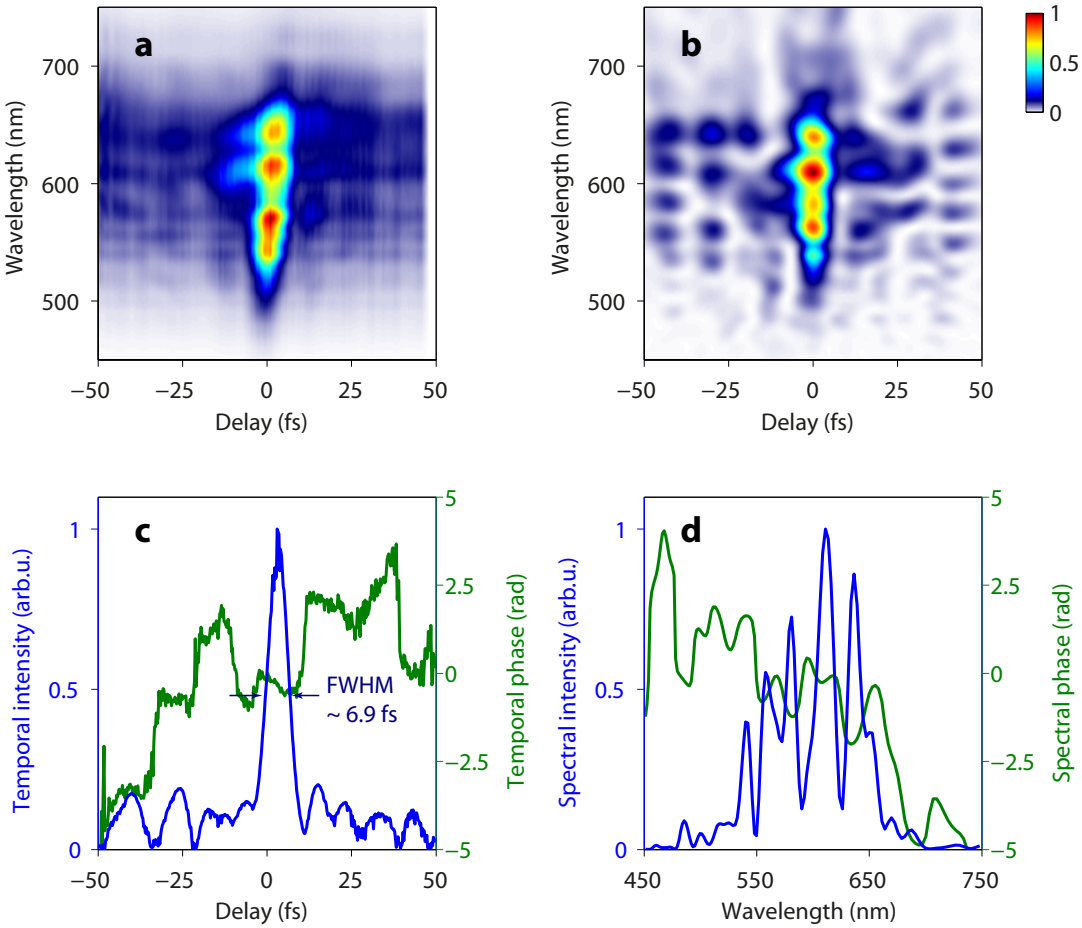

Figure 3.14: FROG measurement and reconstruction of pulses in channel 3. a, Measured FROG spectrogram. **b,** Reconstructed FROG spectrogram. **c,** Reconstructed temporal intensity profile and temporal phase. **d,** Reconstructed spectral intensity profile and spectral phase.

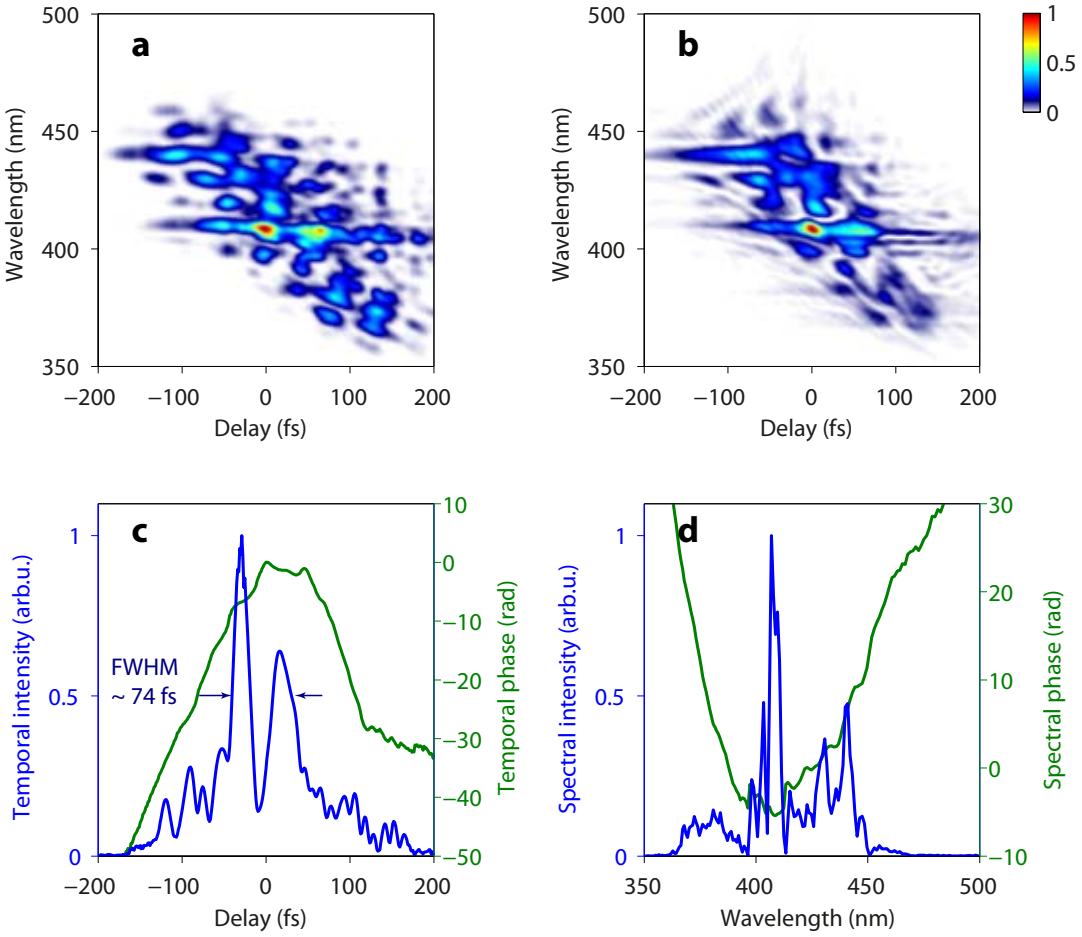

Figure 3.15: FROG measurement and reconstruction of pulses in channel 2. a, Measured FROG spectrogram. **b,** Reconstructed FROG spectrogram. **c,** Reconstructed temporal intensity profile and temporal phase. **d,** Reconstructed spectral intensity profile and spectral phase.

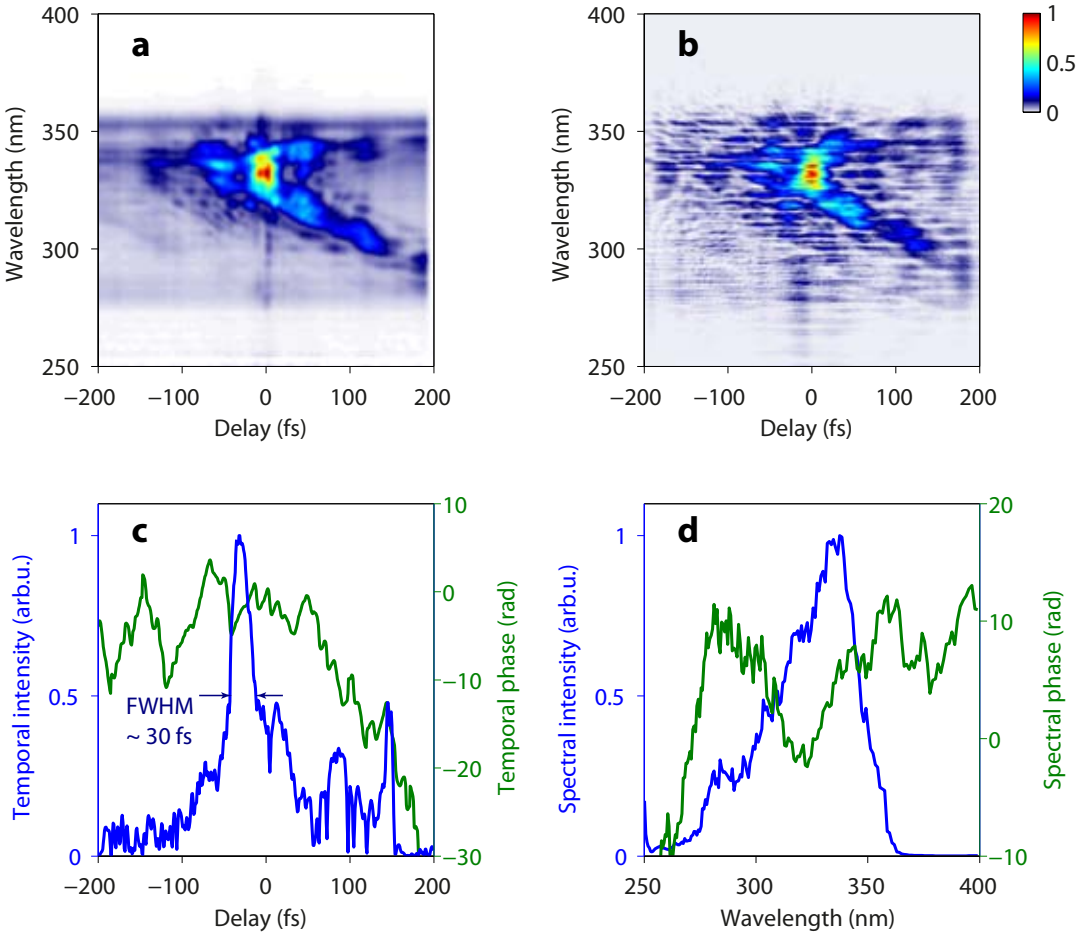

Figure 3.16: FROG measurement and reconstruction of pulses in channel 1. a, Measured FROG spectrogram. **b,** Reconstructed FROG spectrogram. **c,** Reconstructed temporal intensity profile and temporal phase. **d,** Reconstructed spectral intensity profile and spectral phase.

Compression of pulses in the channel 0, 1, and 2

For the channels seeded by the pulses behind the blue fiber, the compression is a lot more challenging. At the moment, because of the huge dispersions the pulses in these channels encounter during propagation, we can only manage to compress a part of their total spectral phase.

In particular for channel 2 (from $350 - 500$ nm) in Fig. 3.15, a considerable second order dispersion (GDD) was uncompressed even after 12 reflections on the chirped mirrors.

More specifically, the measured spectral phase in Fig. 3.15d suggests that the remaining GDD is $\sim 150\ fs^2$. If all of this spectral phase is compensated properly, the pulse will have its Fourier limit of ~ 5.7 fs. Simulation suggests that a GDD compensation equivalent to ~ -1.6 mm of Fused Silica is sufficient to make this spectral phase flat, the pulse will be compressed down to ~ 5.9 fs. However, due to the imperfections of the chirped mirrors, addition of number of reflections would further compromise the efficiency and transmission.

Fig. 3.16 shows the current status of the compression of the channel 1 (from $270 - 350$ nm). In this case, the dispersion compensation problem is even more challenging. The measurement results are shown in Fig. 3.16. The reason for non-flat spectral phase seems to be that the chirped mirrors compensate differently for different spectral bands. Fig. 3.16d illustrates that the spectral phase likely has a negative GDD for the lower wavelength part (from $\sim 250 - 300$ nm) and positive GDD for the higher wavelength part (from $\sim 300 - 350$ nm).

Finally, pulses in the lowest channel of the synthesizer (channel 0: $220 - 270$ nm) has not been compressed so far. Their spectral phases are recorded and considered for next iteration of chirped mirrors.

3.4.4 Energy of pulses in different channels

Table 3.2 summaries result on the power of the pulses exiting from the three stage synthesizer. The SHG conversion efficiency is 50%, the fundamental beam after the BBO get reduced slightly due to the imperfection of the beam splitter that splits the blue and the red beam (the designed transmission for the ~ 800 nm beam is $< 95\%$ which means that practically the transmission is lower than that). After that, the chirped mirrors used for compensating the SH beam decrease $\sim 30\%$ energy of the SH pulses. The counterpart in the fundamental beam decrease around 5%. Next are the fibers, the blue beam does not have high transmission $\sim 25\%$, the red beam got $\sim 50\%$. After the synthesizer, the power of all the channels reduces even more, making only $\sim 1.2W \Longleftrightarrow 400\mu J$.

Table 3.3 summarized in details the reflectivity of the rectangular chirped mirrors. The losses of $80 \rightarrow 90\%$ is very high. Certainly one can argue in this case that since the beam splitters are designed not to have sharp cut in spectrum, this could explain that some of the spectral components transmitting (reflecting) on the BSs, going to the rectangular chirped mirrors will not be reflected. However, in any cases, the **total** transmission (reflectivity) of the complete pack (BSs + CMs) is $10 - 20\,\%$.

Total power input: $\sim 9.1W$				
After BBO and Beam splitter				
Blue beam			Red beam	
$\sim 4.45W$			$\sim 4W$ (5% due to BS)	
After CMs and transport mirrors, in front of fibers				
$\sim 2.9W$			$\sim 3.7W$	
After fibers				
$\sim 700mW$			$\sim 1.75W$	
After the complete synthesizer				
Ch0	Ch1	Ch2	Ch3	Ch4
$\sim 1mW$	$\sim 5mW$	$\sim 61mW$	NA	NA
All channels			All channels	
$\sim 67mW$			$\sim 1.1W$	
All channels, after the complete synthesizer				
$\sim 1.2W \Longleftrightarrow \sim 400\mu J$				

Table 3.2: Power of pulses in all stages of the apparatus, represented from top down as the direction of the beam propagation

Before the stack	Rectangular chirped mirrors	After the stack
$\sim 412mW$	Ch2: 12 reflections	$\sim 92mW$
$\sim 50mW$	Ch1: 10 reflections	$\sim 10mW$
$\sim 26mW$	Ch0: 6 reflections	$\sim 2mW$

Table 3.3: The losses due to the reflection on the chirped mirrors stack are from $80 \rightarrow 90\%$

Effect of the power/energy per pulse on the FROG characterizations

Usually for a reasonable FROG measurement in our setup, the input pulse should have the energy of $\sim 1\,\mu$J or more (applicable for pulses in the channels while compressed, i.e. ~ 10 fs) for us to have reasonable statistics (at 3 kHz). As a result, for an uncompressed pulse whose duration is a lot longer, its energy per pulse has to be also higher in order for the third order processes to be activated. Nonetheless, table 3.2 shows the fact that at the end of the synthesizer, we have ~ 1 mW power ($\sim 0.3\,\mu$J) of the pulses in the channel 0 and ~ 5 mW power ($\sim 2\,\mu$J) of the pulses in the channel 1. Because these pulses are not compressed yet, their duration can range up to ~ 1 ps (at the order of 100 times longer than the chirped free case). As a consequence, the peak intensity of the pulse focusing on the fused silica sample is not great enough to have third order response. Therefore, measuring the FROG spectrogram using these powers is a big challenge.

3.5 Next steps for the TW synthesizer

Since much of the time of the PhD work was focused on the exploring the exciting physics underlying the HHG and spectroscopy in solids (represents in the next chapter) as well

as attosecond nonlinear delayed response, there was limited time devoted to enhancing the current technologies and exploring new capabilities such as the works carried out in this chapter. Nevertheless, significant progress has been made. The next steps can be described below.

3.5.1 Compression and optimization

- **Fiber optimization:** Although the output parameters of the supercontinuum after the red fiber are close to optimum values (specified by [58]), better results are possible utilizing finer tunning of the input parameters. Furthermore, since the supercontinuum after the blue fiber has very low transmission ($\sim 25\,\%$) at the moment, there is room for improvements. The best possible scenario might be a different combination of *gas type, fiber length, and fiber core size.*

- **Optimization of compressing pulses in the channels:** Even though pulses in channel 3, 4 are compressed, their FROG traces still suggest that better results can be obtained by tunning high order chirps to eventually flatten the spectral phase completely.

- **Compression of pulses in channel 0, 1, 2:** This is a challenging task because the energy per pulse in these channels are much weaker, they also suffer from higher dispersions due to shorter wavelengths. With knowledge of the existing FROG traces, one can compress pulses in channel 1, 2 in the reasonable time frame. However, compression of pulses in channel 0 depends strongly on optimization of the blue fiber.

- **Beam pointing stabilization:** Since the TW waveform synthesizer is generally a big interferometer, having a stable beam pointing is crucial for any experiments. All the necessary steps are prepared, one only needs to assemble the complete system and perform testings.

3.5.2 Spatial and temporal overlap

Spatial overlap Essentially the steps are similar to what has been described in [117]. Nevertheless, we have improved the scheme by designing a compact, most direct measurement of the beam profile at the focus (in HHG chamber) by only one reflection. The new design should help enhancing the quality of beam at the focus regardless of the number of channels.

Temporal overlap Currently the 4-channel-synthesizer utilizes two spectrometers to resolve spectral interferences between 4 channels. In the new design, the beam will still be divided into two, but with proper spectral range and resolution.

3.5.3 HHG and streaking experiments

Overall, it is the HHG and attosecond streaking that properly characterize the properties of the generated transients just as in the previous generation of light field synthesizer.

In fact, with the current setup of our HHG chamber, we could focus the new beam to reach intensities up to $\sim 10^{16}$ W/cm^2. At this regime of intensity, it has been shown theoretically that generation of 1 keV high order harmonics from gases is possible [140].

Chapter 4

EUV high harmonic generation and spectroscopy in solids

4.1 Introduction

In this chapter, we study the EUV generation using progressively shorter driving fields ranging from few-cycle to half-cycle (optical attosecond pulses) and attain the regime of attosecond manipulation of electron dynamics entailing the radiative processes. The field waveform of laser transients, synthesized in the visible and flanking spectral ranges, have been used for inducing the macroscopic polarization in the bulk of thin ($\sim$ 125 nm) polycrystalline SiO_2 nanofilms, yielding a coherent EUV radiation that extended to photon energies up to $\sim$ 40 eV without inducing damage to the nonlinear medium. Semiclassical and quantum-mechanical calculations of intraband current density have reproduced the key trends in our experimental spectra and offer physical insight into this control. Our experiments have established the emitted radiation as a sensitive probe for optical-field-driven, attosecond, electronic processes in condensed matter as well as a novel compact, solid-state light source in the EUV spectral range.

4.2 EUV generation and control in SiO_2

4.2.1 Generation and basic properties

Selection of the samples

The selection of SiO_2 in our quest for laser-driven EUV generation in bulk solids was motivated by its wide bandgap of $\sim$ 9 eV (measured by [190] and calculated by [191, 192]), which (i) is responsible for the high damage threshold [193] of SiO_2 compared with semiconductors or metals, enabling exposure to intense optical fields ($>$ 1.3 V/Å) and (ii) allows the study of nonperturbative interactions by laser pulses spectrally centered around the visible and nearby ranges, where the field manipulation of light [58] and its attosecond control or confinement [117] have recently attained attosecond resolution. The combination of (i) and (ii) further extend the damage threshold to even higher field strengths (more than $\sim$ 2 V/Å [69]). To mitigate both nonlinear and linear distortions of driving and generated fields during propagation in the medium, we opted for thin ($\sim$ 125

nm) films of polycrystalline SiO_2 (amorphous material made up from multiple short-range crystals). Moreover, this thickness of SiO_2 was also estimated to be compatible by order of magnitude with a medium-length supporting coherent build-up of EUV (subsection 4.4.1), based on simple considerations [194].

Experimental setup for EUV generation in SiO_2

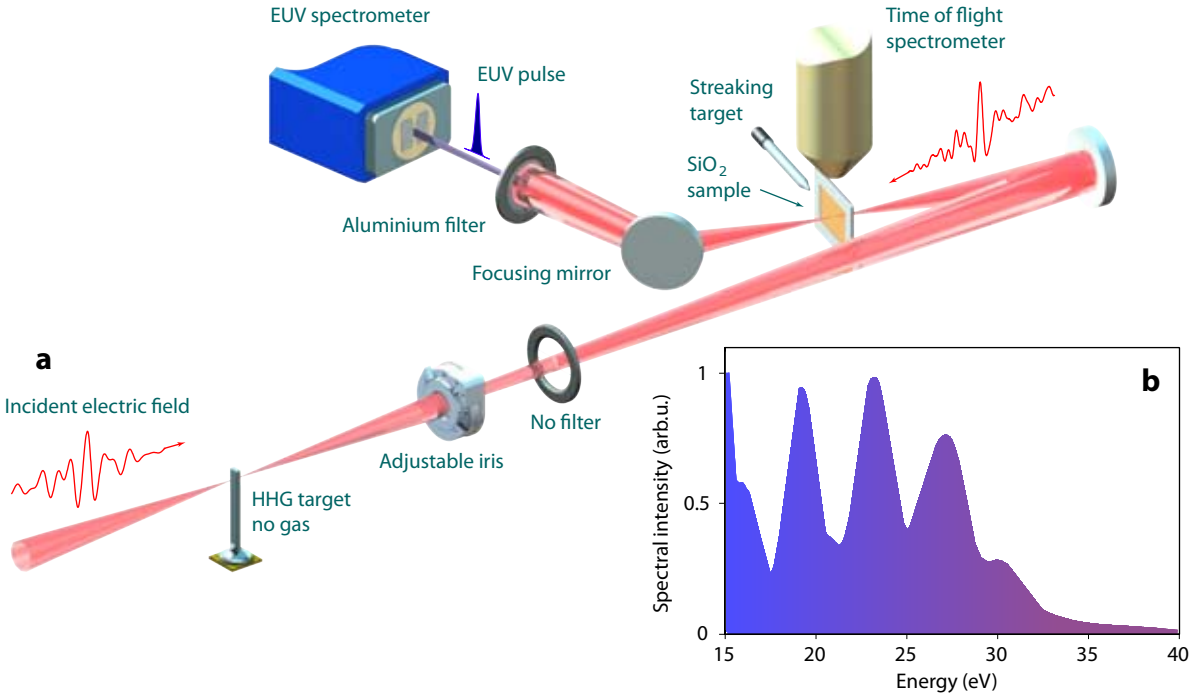

Figure 4.1: Spectral measurements of EUV generation in SiO_2. **a,** One concave spherical rhodium mirror line-focused the generated EUV beam onto the entrance slit of the spectrometer. One aluminum filter ($\sim$ 100 nm) is placed between to transmit only the EUV. **b,** Representative spectrum recorded for 1.5-cycle pulse as incident electric field and its peak field strength of $\sim$ 1.04 V/Å.

In our experimental setup, a concave spherical rhodium mirror is installed right after the SiO_2 sample to route the beam to the spectrometer. Furthermore, the spherical radius of the mirror is designed to project the focal spot (circular shape) of the EUV beam onto the spectrometer perfectly. Since the incident angle is large ($\sim 66°$), the spherical mirror will act as a toroidal mirror (with horizontal radius equals vertical radius). The image of the focal spot is a thin line, its thickness is defined via the effective horizontal focal length, and its length is defined via the effective vertical focal length of the mirror. Furthermore, the aluminum filter ($\sim$ 100 nm) is installed between the spectrometer and the focusing mirror to filter out the low frequencies coming mostly from the incident field. The experimental apparatus is shown in Fig. 4.1a.

Since the reflectivity of the rhodium mirror is relatively flat at our spectral range (IMD, [195]) the signals we recorded on the spectrometer are close to the true EUV spectra (without taking into account wavelength and intensity calibration). The spectra are measured on a commercial spectrometer (McPherson) in which the multi-channel

plate/phosphor's screen is coupled by fiber to a camera (Andor). The camera can be cooled down to −40° C to reduce dark current, improving signal to noise ratio. Because the combination of multi-channel plate/phosphor's screen and camera can be moved along the Rowland circle, photons of different energies propagated through the entrance slit will all be focused on the corresponding positions (angles) of the camera setup.

Fig. 4.1b shows a representative spectrum recorded when the sample is exposed to a (approximately) 1.5-cycle pulse whose maximum field strength is ∼ 1.04 V/Å (inside the sample so that the screening factor ∼ 80% derived from the Fresnel formula is accounted for).

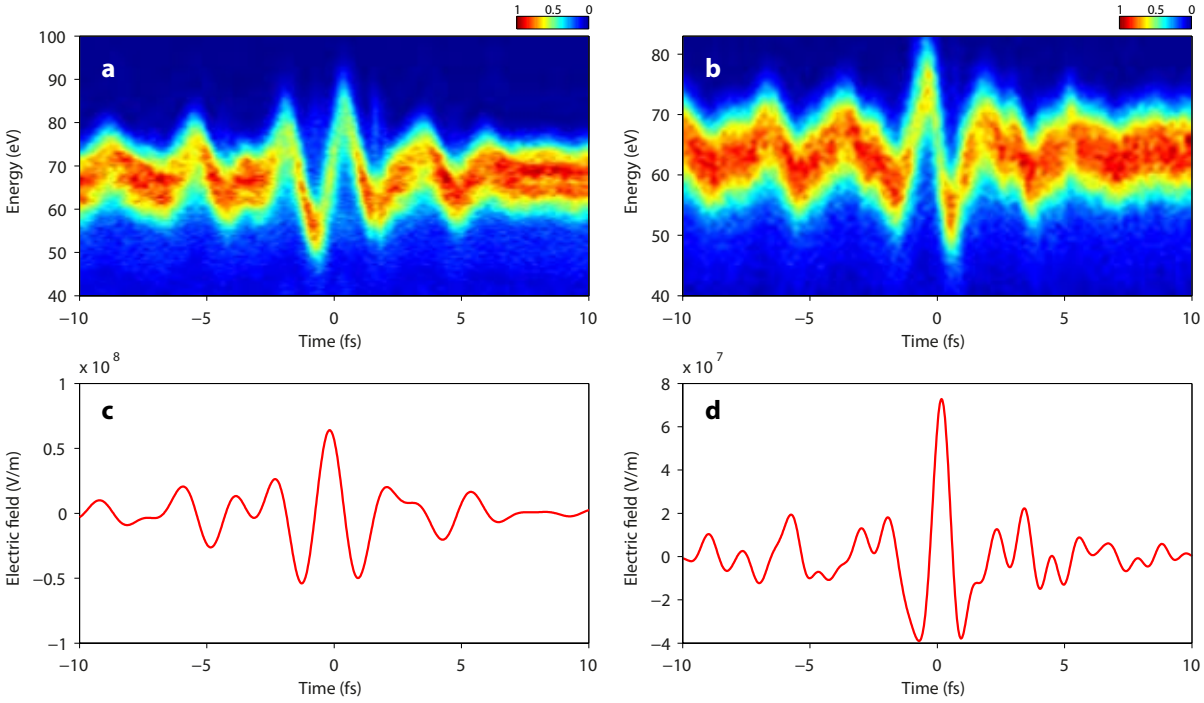

Figure 4.2: Representative attosecond streaking spectrograms of the pulses used in the experiment. a, b, Streaking spectra of the 1.5-cycle pulses and optical attosecond pulses. **c,d,** Reconstructed electric fields for the spectrograms **a** and **b**.

For all the spectra at different waveforms reported below, the electric field used in the experiment is characterized by attosecond streaking (see Fig. 4.2). To synthesize the 1.5-cycle pulses, we physically block the deep UV and UV-visible channels (discussed in more details in Chapter 5), leaving only the photons whose wavelengths are longer than 500 nm. The spatial overlap and temporal overlap locking are kept intact for the remaining two channels. The result is that the combination of the other two (visible and near infrared) channels already makes a relatively short pulse with carrier wavelength $\lambda_c \sim 700$ nm and the intensity envelope duration of ∼ 2.8 fs (we call it ∼ 1.5 cycle pulses because the envelope is longer than the carrier period of ∼ 2.3 fs). The electric field after being characterized by attosecond streaking is scaled up to the corresponding spectra measurements with the help of the iris-power calibration (correlation). Similarly, the optical attosecond pulses are created by utilizing all the available channels, the results of this is shown in Fig. 4.2b.

After exposing the 1.5-cycle pulses at different field amplitudes (Fig. 4.3a illustrates

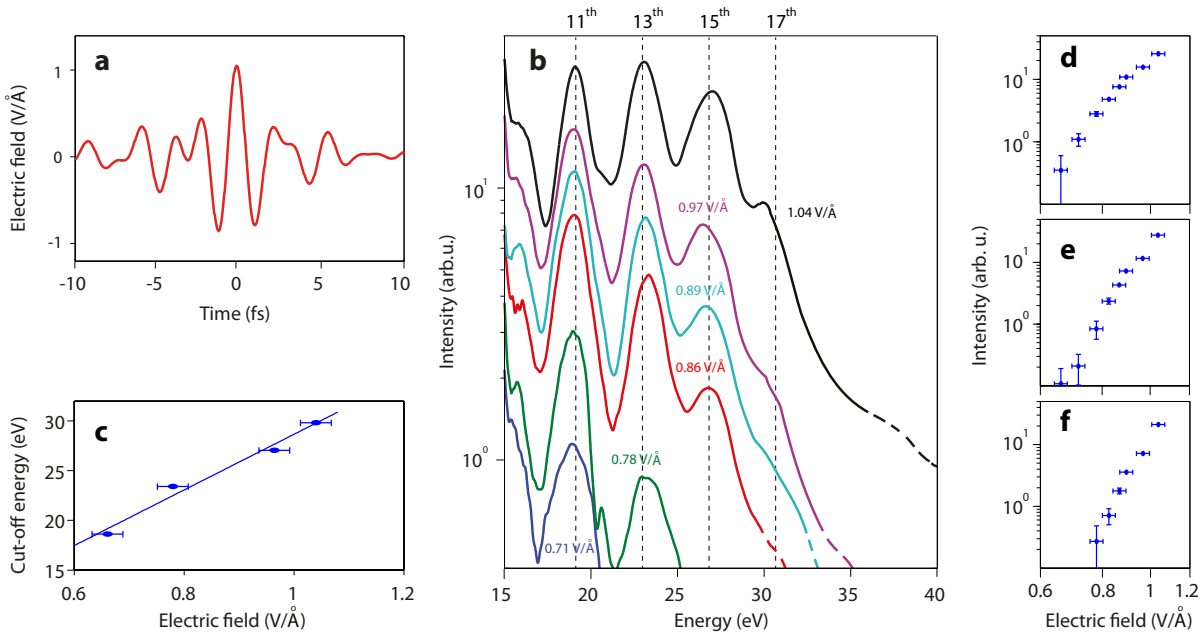

Figure 4.3: EUV generation in SiO_2. a, Incident electric field characterized by attosecond streaking and scaled to the maximum peak field strength used in the experiment. **b,** Spectra recorded for increasing field strengths ($\sim 0.71 - 1.04$ V/Å) denoted by the same color. Dashed lines indicate the noise floor. **c,** Scaling of the cutoff energy as a function of the incident electric field strength. Blue dots are experimental data points. Blue solid line is the linear fitting of the experimental data. **d,e,f,** Spectral intensity of the 11^{th}, 13^{th}, 15^{th} harmonics are represented by blue dots respectively. The experimental errors of the electric field strength are indicated by blue bars. Adapted from [196].

the maximum electric field), we measured the radiated spectra (Fig. 4.3b) accordingly. Furthermore, the wavelength calibration is done by employing the gas HHG spectra in the plateau region generated from few-cycle pulses.

From the intensity scaling of the generated spectra, discernible features are:

- **Harmonic-like structure.** The measured spectra exhibit well defined spectral peaks, both in the logarithmic scale as well as in the linear scale (Fig. 4.1b) with regular spacing of $\sim$ 3.5 eV which is exactly $2\omega_c$ of our carrier wave ($\lambda_c \sim$ 700 nm). In addition, the position of the peaks confirms the harmonic-like structure of our spectra. There is a small 9^{th} harmonic, followed by three strong harmonics: 11^{th}, 13^{th}, 15^{th} and the cutoff 17^{th} harmonic.

- **Formation of a robust multi-ten-eV broad plateau and nonperturbative behavior.** In the gas-phase HHG [197, 198], spectrum exhibits a plateau, which reflects the nonperturbative characteristics of the process. Here, the high harmonics generated from SiO_2 also display a broad plateau region extending from 15 eV to more than 25 eV, covering several harmonics, evidently underlying the nonperturbative character of the physics involved. The nonperturbative character of the generated EUV spectra can be further confirmed by examining the spectral intensity of single harmonics (from 11^{th} to 15^{th}) as a function of electric field strength.

Fig. 4.3d,e,f makes use of the spectra in Fig. 4.3b together with other recorded spectra recorded at interim values of field strength but not plotted in Fig. 4.3b.

- **Linear dependence of the cutoff energy on the field strength.** By defining the cutoff energy as the highest harmonic peak resolvable (discernible) before the onset of noise, Fig. 4.3c shows that the cutoff energy is linearly dependent on the incident electric field strength. This dramatically differs from HHG in gases, where the cutoff scales as a square of the field.

4.2.2 Attosecond control of electron dynamics

The above experiment (Fig. 4.3) establish the generation of coherent EUV radiation from bulk dielectrics and verify key predictions of semiclassical theories, such as the formation of a plateau and a linear scaling of the cutoff energy versus the incident field strength, in analogy to studies in other spectral ranges [43, 46]. Nevertheless, above experiments do not identify the conditions of control of the underlying electronic process nor attain it experimentally. To elaborate on this essential aspect, we took advantage of the capabilities offered by our second-generation light field synthesizer [139] and exposed our samples to various, precisely-characterized driving fields in terms of pulse duration, carrier frequency, intensity and global phase.

General control scheme

In this section, the first waveform has not only the longest central wavelength ($\lambda_c \sim 800$ nm) but also the longest pulse duration (~ 7 fs). We created it (Fig. 4.4a) simply by blocking all the other three channels of our synthesizer (same techniques used in Chapter 2, leaving only channel near infrared passes through (few-cycle pulses). As a consequence, there was no need of spatial overlap and temporal locking, the synthesizer is a lot simpler and easier to use.

After characterizing the electric field at $\varphi_G = 0$ via attosecond streaking (Fig. 4.4a, solid blue line, scaled up), this field and its counterpart with different global phase $\varphi_G = \pi/2$ rad (solid red line) are applied consecutively to the SiO_2 sample. Their EUV spectra are shown in Fig. 4.4b (filled blue and red areas, respectively). We observed that the harmonic-like structure remains and harmonic spacing changes to ~ 3 eV which is compatible to the carrier frequency, which is slightly less than that in Fig. 4.3a. The spectra show limited sensitivity to the global phase.

Since the foundation of the attosecond physics, the extreme nonlinearities emerging from the exponential rule of tunneling ionization [13] and the quadratic dependence of the quiver energy of electrons to the incident field [12] are already demonstrated in the few-cycle regime [29, 94]. Surprisingly, these degrees of control were not presented here because only the minor differences between two EUV spectra were found.

When we progressively shorten the pulse durations (to a 1.5-cycle pulses), more deviation of the EUV spectra at one phase setting compared to the others is observed. Fig. 4.4d shows the similar behavior as we have learned in the intensity scaling measurement (Fig. 4.3): the radiated EUV spectra feature harmonic-like structure, existence of a plateau region. Spectral differences (mostly amplitude) between the two EUV spectra at low energy range ($\sim 16 - 22$ eV) are observed but they do not differ much at high energy

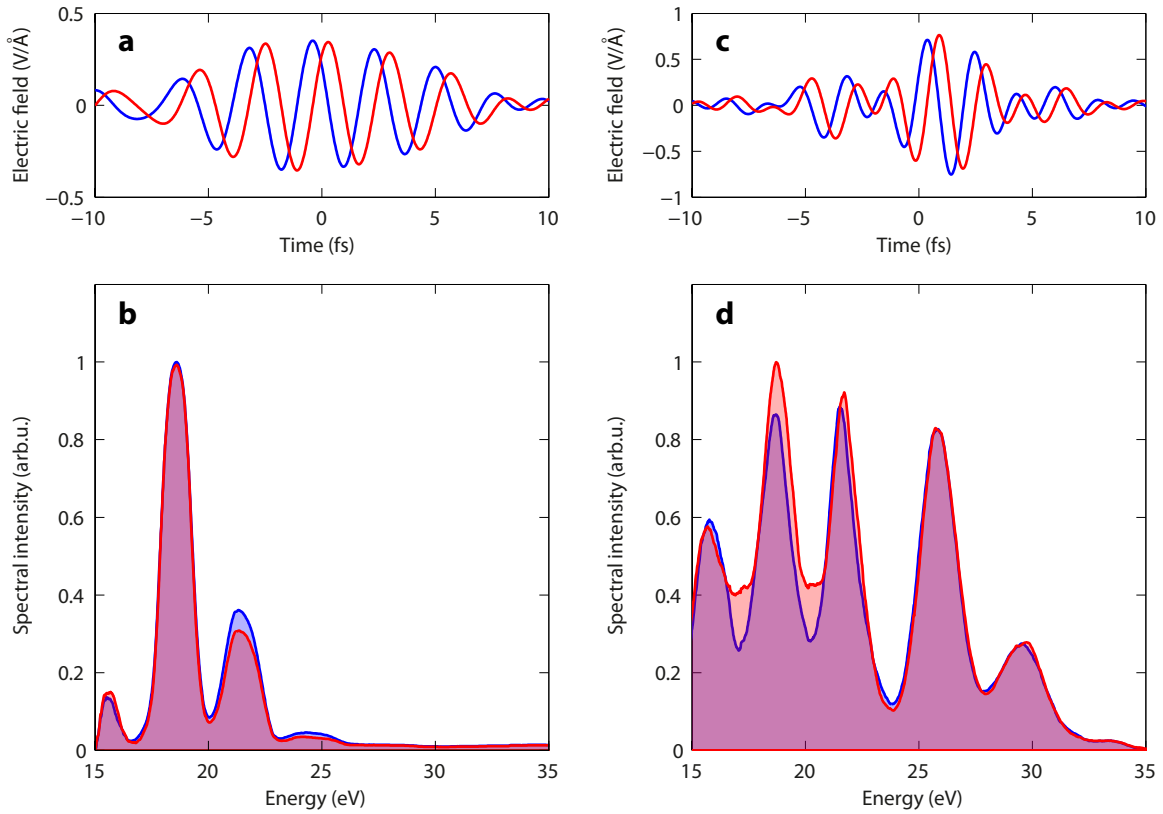

Figure 4.4: EUV emission dependence on global phase for few cycle and 1.5-cycle pulses. **a,** Electric fields (few-cycle pulses) used to excite the SiO_2 sample at two different global phase settings: $\varphi_G = 0$ rad (blue solid line) and $\varphi_G = \pi/2$ rad (red solid line). **b,** Captured EUV spectra of HHG radiation for electric fields at two global phases (same colors). **c,d,** Same as **a,b,** but with the 1.5-cycle pulses as incident electric fields. Adapted from [196].

range (above 22 eV). As a result, the subtle change in the spectral intensity observed for two different global phase settings here does emphasize the limited control of the electric field waveforms to the generated radiation, furthermore implying that the physics in this case differs significantly to the physics underlying HHG in gas-phase systems.

EUV emission control using attosecond light transients

By physically blocking only the DUV channel, we synthesized an electric field that is characterized by attosecond streaking as in Fig. 4.5a - solid blue line (scaled up). Because this pulse has the duration of ~ 1.7 fs while its carrier wavelength ~ 640 nm and its carrier period ~ 2.1 fs, we call it a single-cycle pulse.

The generated EUV spectra recorded from this pulse and its global phase changed counterpart are illustrated in Fig. 4.5b. Noticeable spectral differences can be seen across the whole spectra. At this limit of the pulse compression, the EUV spectra do not differ only in amplitude but also in their shapes, especially from $\sim 20 - 25$ eV.

All of above investigations of the radiated EUV spectra dependence on the electric field waveforms deduce the need to study the behavior of coherent EUV radiation at the ultimate limit of pulse compressions: attosecond light transients. Fig. 4.5c illustrates the

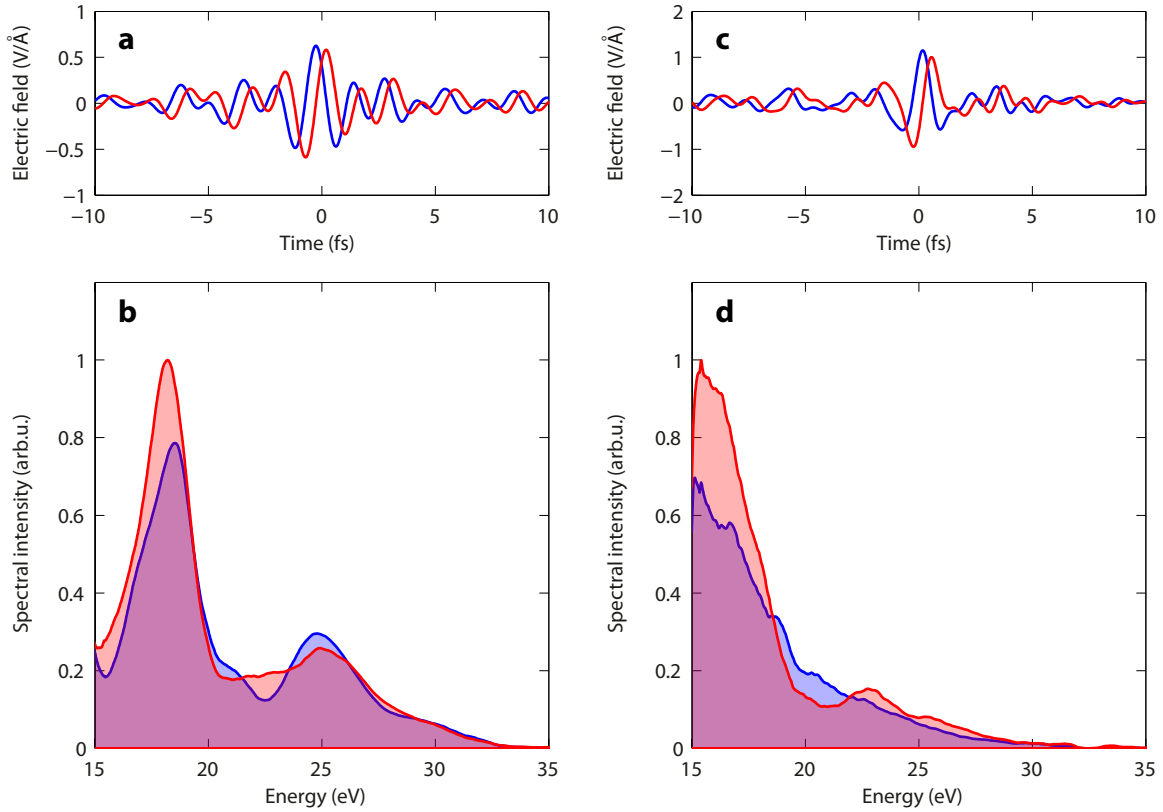

Figure 4.5: EUV emission dependence on global phase for single-cycle pulses and attosecond light transients. a, Electric fields (single-cycle pulses) used to excite the SiO_2 sample at two different global phase settings: $\varphi_G = 0$ rad (blue solid line) and $\varphi_G = \pi/2$ rad (red solid line). **b,** Captured EUV spectra of HHG radiation for electric fields at two different global phases (same colors). **c,d,** Same as **a,b,** but with the attosecond light transients as incident electric fields. Adapted from [196].

electric fields measured by attosecond streaking (solid blue line, scaled up) and the same electric field but its spectral phase is shifted by $\pi/2$ rad (solid red line, scaled up). This is the extreme limit of pulse compression with the effective bandwidth broader than 2 octave, the carrier wavelength ~ 530 nm and effectively this is a half cycle pulse with an instantaneous intensity profile duration of ~ 400 as (shown in Chapter 2, Fig. 2.8a). The recorded EUV spectra (Fig. 4.5d) show remarkable differences compared to the single cycle case and complete difference in contrast to the few-cycle and 1.5-cycle cases. Indeed, when the sample is excited by an optical attosecond pulse, the spectrum (filled blue area) exhibits no harmonic peaks, there is only a broad supercontinuum expanding more than 15 eV. Conversely, when the sample is hit by the same pulse but its spectral phase is shifted by $\pi/2$ rad, the radiated spectrum (filled red area) displays more discernibly two harmonic peaks, each one spanning more than 5 eV. Overall, this behavior of the EUV spectra is very similar to what have been observed for HHG in gases at the cut off region when driven by few cycle laser pulses [29], but in our case, the pulses have to be a lot shorter and faster.

In conclusion, by changing the electric field waveforms from the few-cycle pulses to attosecond light transients, we observed from negligible control with no spectral differences

to substantial control with broadband supercontinuum opposed to harmonic-like spectrum at two different global phase settings. This characteristics of the generated EUV spectra is significantly different from HHG in gases thus suggesting a different physical mechanism underlying these processes.

4.3 Theoretical description

After exploring the spectral characteristics and their dependencies to the global phase of the generated EUV spectra, we perform the semiclassical and quantum-mechanical simulations according to Refs. [41, 44–46, 49, 199, 200] and compare them to our experimental data.

4.3.1 Semiclassical model

In the reciprocal space (or **k**-space), the crystal momentum of electron is described by the so called "acceleration theorem" [201]. It was shown that motion of electron in the electromagnetic field can be described by the following equations:

$$\mathbf{v}_\nu = \frac{d\mathbf{r}}{dt} = \frac{1}{\hbar}\frac{\mathcal{E}_\nu(\mathbf{k})}{d\mathbf{k}}, \tag{4.1}$$

$$\frac{d\mathbf{k}}{dt} = -\frac{e}{\hbar}\Big(\mathbf{E} + \frac{1}{c}\mathbf{v}\times\mathbf{B}\Big) \tag{4.2}$$

m_0 is the mass of free electron, $e > 0$ is the elementary charge, $\mathcal{E}_\nu(\mathbf{k})$ is the dispersion of the band ν, **E** and **B** are electric, magnetic fields.

We considering the non-relativistic regimes, where $\mathbf{v}\times\mathbf{B} \ll \mathbf{E}$ then Eq. (4.2) reduces to

$$\frac{d\mathbf{k}(t)}{dt} = -\frac{e}{\hbar}\mathbf{E}(t) \tag{4.3}$$

The charge carriers gain momentum and kinetic energy from the electric field. If the field is strong enough to push the electrons to the edges of the Brillouin zone, we have three possibilities. First, the electron may perform the transition to the upper bands via interband Zener tunneling [202] or multiphoton process. Second, the electron may scatter (with other electrons, phonons, etc). Finally, it can stay in the same band and perform the Bloch oscillation [201] with the frequency $\omega_B = e\mathbf{E}a/\hbar$, which determines the corresponding energy of emitted radiation due to decelerated motion of electron in the lattice. Here, a is the lattice constant.

Following [45], we consider the pre-existing Gaussian electronic wavepacket $f_\nu(\mathbf{k}, t_0)$ in the first conduction band ($\nu = c$) at initial moment of time t_0. We neglect the interband transitions and electron-electron interactions. Also, we neglect the current induced by holes in the valence band, because the simulations have shown that their contribution is negligible.

As it is shown, electron exposed to a laser pulse gains momentum from the field and explores the regions where the bandstructure is non-parabolic (see Fig. 4.6). Decelerated motion in these regions induces the radiation of high harmonics.

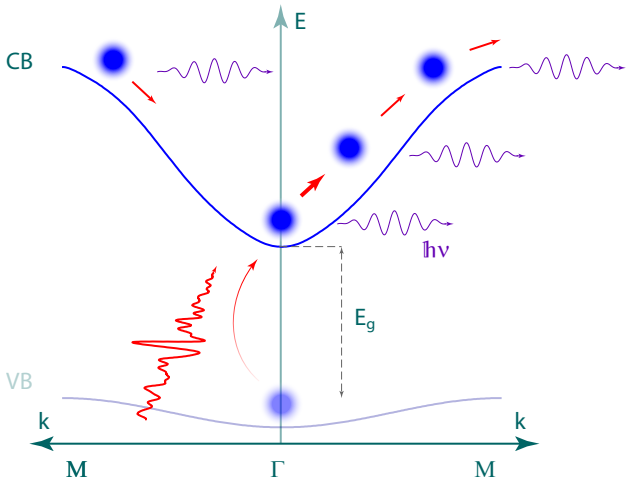

Figure 4.6: Dynamics of electron wavepacket in the semiclassical picture. Valence band is presented as semi-transparent. The bandgap is denoted as E_g. The incident electric field accelerates the electron wavepacket along the field polarization, which is directed along the Γ–M direction of the Brillouin zone. Adapted from [196].

The Boltzmann equation, which governs the dynamics of a system, contains only the acceleration term

$$\frac{\partial}{\partial t} f(\mathbf{k}, t) = -\frac{e}{\hbar} \mathbf{E}(t) \frac{\partial}{\partial \mathbf{k}} f(\mathbf{k}, t) \tag{4.4}$$

and has the following analytical solution

$$f(\mathbf{k}, t) = f_0 \left(\mathbf{k} + \frac{e}{\hbar} \mathbf{A}(t), t_0 \right), \tag{4.5}$$

where

$$\mathbf{A}(t) = \int_{t_0}^{t} \mathbf{E}(t') dt'$$

is the vector potential of the laser field.

This means that the electric field pushes the electron wave packet forward and backward in the **k**-space while keeping the overall shape of the electron wave packet.

Finally, we calculate the current density of conduction band electrons as

$$\mathbf{J}(t) = -\frac{2e}{(2\pi)^3} \int_{\mathrm{BZ}} v_c(\mathbf{k}) f_c(\mathbf{k}, t) d^3k \tag{4.6}$$

Propagation effects

In general, if one has the absolute amplitude of the current, it can be inserted directly to the Maxwell's equations to obtain the exact solution. This often requires costly calculation including the propagation in 3D space.

In our case, the simpler approach can be used to determine the spectrum of intensity. From the derivation of the first order propagation equation in the frequency domain A.9, one can see that the *creation term* $\frac{\partial \mathbf{E}(\mathbf{r},\omega)}{\partial z}$ on the left hand side primarily depends on the *dispersion (absorption) term* $ik(\omega)\mathbf{E}(\mathbf{r},\omega)$, the *diffraction term* $\frac{i}{2k(\omega)} \nabla_\perp^2 \mathbf{E}(\mathbf{r},\omega)$, and the

nonlinear polarization term $\frac{i\omega}{2\epsilon_0 n(\omega)c}\mathbf{P^{NL}}(\mathbf{r},\omega)$. We see that the generated electric field in frequency domain is proportional to $\omega \cdot \mathbf{P^{NL}}(\mathbf{r},\omega)$. Dimensional analysis of the Ampere's law shows that $\omega \cdot \mathbf{P^{NL}}(\omega) \propto \mathbf{J}(\omega)$, which means that the radiated spectrum $S(\omega)$ is proportional to $\left|\mathfrak{F}\left[\mathbf{J}(t)\right]\right|^2$.

The observed spectrum is usually the total coherent superposition of radiated waves recorded *after propagation*. Therefore, we need to take into account dispersion (absorption, gain) and diffraction terms. Without solving exact propagation equation, we know that for a short-distance propagation, the dispersion term can be neglected, and the term $\nabla^2_\perp \mathbf{E}(\mathbf{r},\omega)$ can be solved by simple multiplication in the momentum space[1]. Finally, the solution of this operation is proportional to $\omega \cdot \mathbf{E}(\mathbf{r},\omega)$. Therefore, the main effect of the diffraction term is to make the low frequencies (long wavelengths) to diffract more, hence making them weaker in the far field and the high frequencies (short wavelengths) to diffract less, hence making them stronger when both are compared relatively. As a result, one can approximate the final observed spectrum in the far field, after propagation inside the medium, as proportional to additional ω in the electric field in frequency domain, i.e. $S(\omega) \propto \left|\mathfrak{F}\left[\frac{d\mathbf{J}(t)}{dt}\right]\right|^2$.

Above mentioned propagation effects are only applicable, if we are really measuring the spectra in a far field region. However, if a collimating mirror (or any focusing optics) is being used to collect the emitted radiation onto the slit of the spectrometer (which is *usually* the case) to improve the signal strength, then the diffraction no longer applies, hence the detected spectra would be similar to the spectra generated at the exit of a medium. In this case, we do not need to apply diffraction effect in the propagation of the signal from the end of the generating medium to the entrance slit of the spectrometer. The diffraction effect inside the sample (or in gas nozzle in other cases) still applies. In conclusion, the above discussion illuminates that in our particular case here, the most appropriate first order approximation of our spectrum is $S(\omega) \propto |\omega \mathbf{J}(\omega)|^2$ without using the full propagation calculation.

4.3.2 Semiconductor Bloch equations

To verify the results of semiclassical simulations we also considered a quantum mechanical model based on the semiconductor Bloch equations (SBEs) [203, 204] together with the inclusion of the driving electric fields [205].

These equations serve as a great tool to study dephasing processes via *Four-Wave Mixing* or to study the carrier dynamics leading to extreme nonlinear optical response of a quantum system [41, 43, 49, 199], etc. Even though there was no direct comparison to show the differences between the multiple two-level systems to the SBEs, Golde *et al.* [199] have pointed out the enhancement of generation of the odd harmonics in semiconductor equations compared to the single two-level system.

Furthermore, when one considers the electronic excitations driven by the strong field, one realizes that the many-body Coulomb interaction will start playing a role. In fact, once the electrons and holes are generated in the conduction and valence bands, Coulomb interaction between them will inevitably affect their dynamics and consequently modify the total optical response of the system [203, 206]. However, it has been shown [199]

[1] Not to be confused with the crystal momentum **k**-space.

that in the regime of extreme nonlinear optics (strong field physics), the emission of a system being driven by a strong field will have little contribution from the Coulomb interaction. The main contribution to the radiated photons comes from light-matter interaction and the Coulombic forces only play an important role in weak field regimes. Therefore within the scope of the thesis, we only consider the SBEs with the omission of the Coulomb interaction [41]. Since the derivation of this quantum mechanical model is rather complicated, its derivation will not be described here and it is recommended to consult more complete treatment of this topic in [203, 204].

In the independent particle approximation, the equations describing the dynamics of interband coherence $p_{\mathbf{k}}$ and populations of electrons $f_{e,\mathbf{k}}$ and holes $f_{h,\mathbf{k}}$ can be written as [41]

$$i\hbar\frac{\partial}{\partial t}p_{\mathbf{k}} = \left(\mathcal{E}_{e,\mathbf{k}} + \mathcal{E}_{h,\mathbf{k}} - i\frac{\hbar}{T_2}\right)p_{\mathbf{k}} - (1 - f_{e,\mathbf{k}} - f_{h,\mathbf{k}})\mathbf{d}_{\mathbf{k}} \cdot \mathbf{E}(t) + ie\mathbf{E}(t) \cdot \nabla_{\mathbf{k}} p_{\mathbf{k}} \tag{4.7a}$$

$$\hbar\frac{\partial}{\partial t}f_{\lambda,\mathbf{k}} = -2\mathrm{Im}[\mathbf{d}_{\mathbf{k}} \cdot \mathbf{E}(t)p^*_{\mathbf{k}}] + e\mathbf{E}(t) \cdot \nabla_{\mathbf{k}} f_{\lambda,\mathbf{k}}. \tag{4.7b}$$

Here, $\lambda = e, h$ is the index, which specifies either electron or hole, $\mathcal{E}_{e,\mathbf{k}} = \mathcal{E}_{c,\mathbf{k}}$ and $\mathcal{E}_{h,\mathbf{k}} = -\mathcal{E}_{v,\mathbf{k}}$ are energies of the corresponding carriers, T_2 is the dephasing period, $\mathbf{d}_{\mathbf{k}}$ is the dipole matrix element characterizing the transitions between the two bands.

The total interband polarization $\mathbf{P}(t)$ and intraband current density $\mathbf{J}(t)$ are given by

$$\mathbf{P}(t) = \sum_{\mathbf{k}} \left(d_{\mathbf{k}} p_{\mathbf{k}}(t) + c.c.\right) \tag{4.8}$$

$$\mathbf{J}(t) = \sum_{\lambda,\mathbf{k}} -2ev_{\lambda,\mathbf{k}} f_{\lambda,\mathbf{k}}(t), \tag{4.9}$$

where $v_{\lambda,\mathbf{k}}$ is the group velocity of the λ^{th} band defined by Eq. (4.1).

If we utilize the same consideration that has been done before (for the case of semiclassical model), we can see that the spectrum generated at the source point is $S(\omega) \propto \left|\mathfrak{F}\left[\frac{d\mathbf{P}(t)}{dt} + \mathbf{J}(t)\right]\right|^2$. Then correspondingly, the most appropriate way to estimate our spectrum at the detection point is to take first order approximation for the propagation, finally we get the spectrum $S(\omega) \propto \left|\omega^2\mathbf{P}(\omega) + i\omega\mathbf{J}(\omega)\right|^2$. In this case, $\mathbf{P}(\omega) = \mathfrak{F}\left[\mathbf{P}(t)\right]$ and $\mathbf{J}(\omega) = \mathfrak{F}\left[\mathbf{J}(t)\right]$. This consideration agrees to what has been suggested before by Golde, Meier, and Koch [41]. However, in their recent publication [43], they have adapted to a slightly different formula: $S(\omega) \propto \left|\omega\mathbf{P}(\omega) + i\mathbf{J}(\omega)\right|^2$.

Additionally, if one wants to investigate the spectra generated by the polarization and current separately, one can have the interband polarization spectrum: $S_{\text{inter}}(\omega) = \left|\omega^2\mathbf{P}(\omega)\right|^2$ and intraband current spectrum: $S_{\text{intra}}(\omega) = \left|\omega\mathbf{J}(\omega)\right|^2$. This is unarguably a strong advantage of the theoretical calculations. One can separate different terms in an equation and investigate their effects individually while this is not yet feasible experimentally.

While an analytical solution is available for the semiclassical model, it has been shown [199, 207, 208] that the approximations and simplifications are not enough to derive an analytical solution for the SBEs with realistic experimental parameters. Therefore, numerical techniques have to be employed to find solutions for such equations. Several

techniques suggested in the consideration of the semiclassical model have been tested and it turns out that a combination of second order discretization scheme in **k**-space and an adaptive Runge–Kutta 4-5 integrator provided satisfactory results.

Semiconductor Bloch equations for multiple bands

On the other hand, if we look to elaborate the current two band model, we can see that adding more levels (bands) into our current SBEs might bring the model closer to reality. However, by selecting the length gauge representation of the SBEs as we have shown above, one difficulty immediately comes as an intrinsic problem of the numerical calculation in the length gauge at band degeneracies. When we consider multiple bands (levels) of the band structure in solids, there are level crossings which if not treated well, will lead to unphysical (numerical) results. One solution is to switch to velocity gauge representation using the solution of the density matrix equations in 1D [209] or more sophistically employing TDDFT [210, 211]. In fact, employing the velocity gauge results in a set of uncoupled equations [209] that is easy to scale up (include more number of bands) and it is free from effects of degeneracies. However, the velocity gauge approach also has a number of its own problems: it is hard to put phenomenological dephasing time into the equations, strict requirements for input parameters [209], numerical errors at low frequencies [200], etc. As a result, a good solution might be to use the length gauge representation but with proper implementation of the numerical issues as demonstrated in [200].

Nonetheless, by treating the degeneracies well (smooth them using numerical techniques), one can just expand the original equations to multiple bands, as fully described by S. W. Koch *et al.* [43]. We found that this is a convenient way of extending the model given the existence of the numerical solution of the two band model, thus we adopted this extension for our simulations.

4.3.3 Applications of numerical simulations to experimental data

After having described two models and their numerical implementation, we utilize the *precisely characterized* electric field waveforms as the input to the simulations and investigate calculated results.

Input parameters to the numerical simulations

Electric fields utilized in simulations In order to give a coherent view throughout the text, all the electric fields, regardless of being described in (*a.u.*) (atomic units) or V/Ångstrom (SI), they are the fields inside the samples unless specifically mentioned otherwise. The real applied fields inside the sample would then be scaled down compared to field in vacuum by Fresnel's formula for the S-pol and P-pol beam:

$$T_{\mathrm{t},\perp} = \frac{2}{1 + n_t/n_i \cdot \cos(\theta_t)/\cos(\theta_i)}, \tag{4.10a}$$

$$T_{\mathrm{t},\parallel} = \frac{2}{n_t/n_i + \cos(\theta_t)/\cos(\theta_i)} \tag{4.10b}$$

Here $n_t\,, n_i$ are the refractive indices of the transmitted and incident medium, $\theta_t\,, \theta_i$ are the transmitted/incident angle. Generally for our experiments here, normal incident geometry is used thus the fields inside the sample are ~ 0.8 times the field strengths outside (neglecting interference effects due to thin film).

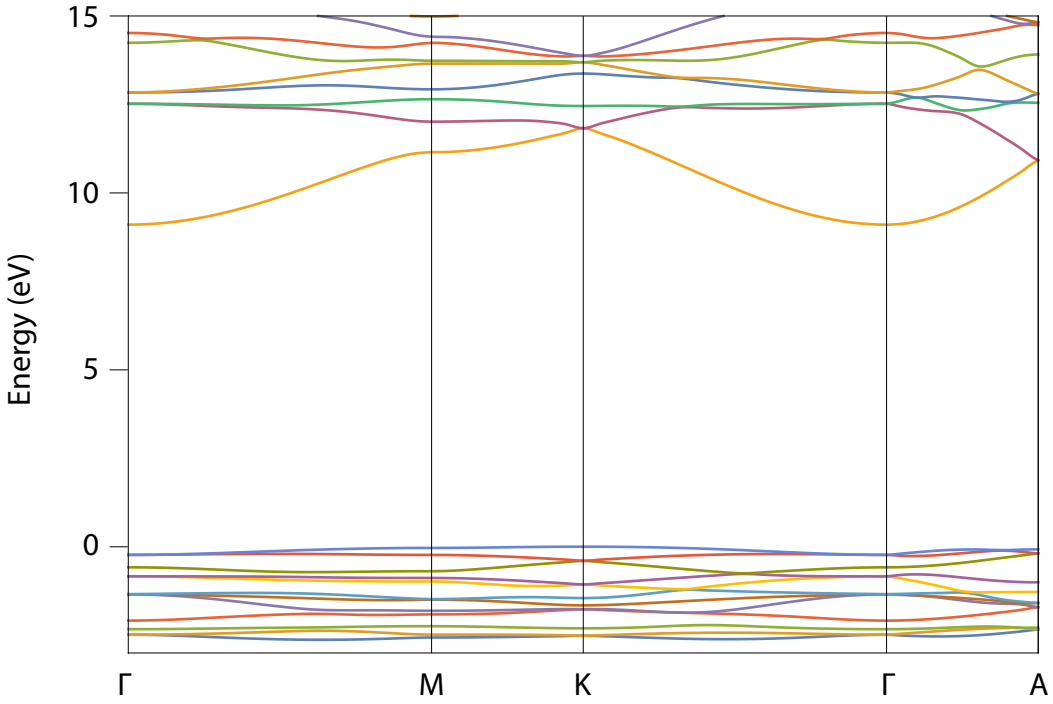

Figure 4.7: Band structure of α-quartz. Calculated with Wien2K software package [212]. Adapted from [196].

Band structure of SiO_2 and dipole matrix elements The band structure and dipole matrix elements are extracted from Wien2K [212], and Virtual NanoLab [213]. For our case, considering α-quartz, they both offer similar results to each other as well as to Schlüter [191] using self-consistent pseudopotentials.

As a result, for the semiclassical model (involving only one band, in our current consideration), we used the existing results from Schlüter [191]. However, for the quantum-mechanical model, we need to have dipole matrix elements as well, thus we opted to use the exact expression of the dipole matrix elements: momentum matrix elements divided by energy difference. [203].

Consideration of multiple bands and directions

Practically, for the numerical solution of the SBEs, the calculation time increases as the number of bands included in the consideration increases. Therefore, knowing an optimal number of bands can help us substantially in getting the most out of the model such that the accuracy or precision of the calculation is not compromised. For this purpose, we performed a calculation of multiple band SBEs including eight valence bands and six conduction bands. Since in this model, the strength of the generated signal

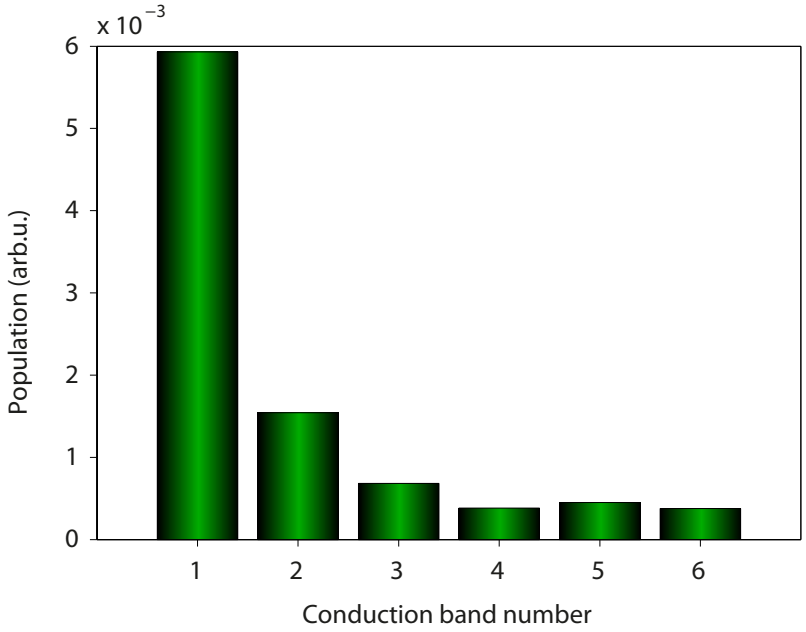

Figure 4.8: Time-averaged populations in the lowest conduction bands. Multiple band SBEs calculated using the 1.5-cycle pulse from Fig. 4.3a at the peak field strength of 1 V/Å. The bands are selected along the Γ–M direction. The average of population is taken from −2 to 2 fs. Adapted from [196].

depends strongly on the amplitude of the population of electrons (and holes) that are excited to conduction (or valence) bands, we examine the time-averaged population in the conduction bands as illustrated in Fig. 4.8.

The result of this simulation, in this case, shows that the excitation to the lowest conduction band is dominant and it drops nearly exponentially for higher conduction bands. Even though we understand that the total emitted spectra is the coherent sum of all the emission from different bands, this simulation already suggests we can restrict our computationally demanding quantum-mechanical simulations to a single valence and conduction band without compromising much the interpretation.

Furthermore, since we know that there are different directions where the laser polarization can be aligned to with respect to the crystal axes, a perfect consideration should take into account all the directions (or integration in 4π directions - 3D). However, for the sake of simplicity, we calculate the generated spectra in the region of interest using band dispersions for different directions (for the semiclassical only, the SBEs would yield similar results), as demonstrated in Fig. 4.9.

Fig. 4.9 demonstrates that if the laser polarization is aligned to other directions, Γ–K and Γ–A, the yield of the emitted spectra will be order of magnitude smaller than when the laser polarization aligned along the Γ–M direction. As a result, we consider only Γ–M direction in all the simulations below.

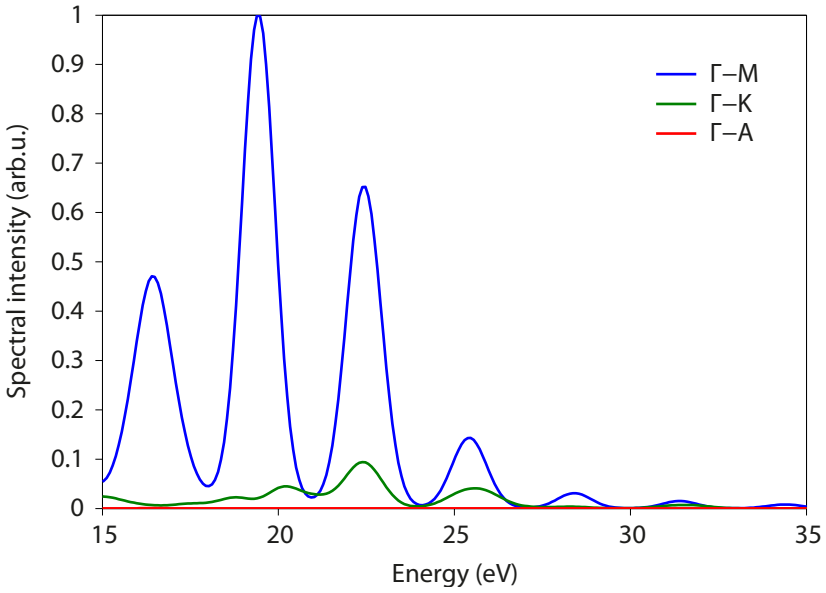

Figure 4.9: Intensity spectra calculated with a semiclassical model for different orientations of the field polarization (1.5-cycle pulse). The spectrum for the $\Gamma - A$ direction (red line) is too weak to be seen on the linear scale. Adapted from [196].

Role of interband coherence

From the Eq. 4.7a, it is clear that both the intraband and interband dynamics are coupled. As a result, the intraband excitation modifies the interband excitation and consequently enhances the generation of high order harmonics [41], but most of the radiation still comes from the interband polarization. Therefore in our experiments, one could naturally expect the interband polarization to play a significant role in the EUV emission. And because in our semiclassical simulations, the interband excitation is not taken into account thus this model might not be applicable for our experiments.

To seek a transparent answer to the above problem, we compare the intensity dependence of the 11^{th} harmonic in our experiments (Fig. 4.3) with that predicted, for the same harmonic peak, from the interband and intraband excitations in our quantum-mechanical and semiclassical simulations, as illustrated in Fig. 4.10. The results highlight the excellent reproduction of the experimental yield dependence by the semiclassical simulation and the intraband term of the quantum-mechanical model, and poor agreement with the yield calculation from the interband polarization term. This fact supports: (i) other physical mechanisms that enhance the existence of electrons in the conduction band, for instance, because of the defect states or doped materials, etc eventually boosts the importance of the semiclassical model or explains the validity of the assumption of a pre-existing electron wavepacket in the conduction band; (ii) the real dephasing time of the interband polarization is on a time scale much faster than the longitudinal-optical (LO) phonon oscillation period $\tau_{\text{LO}} \approx 27$ fs [214] that we have assumed as the dephasing time in our simulations.

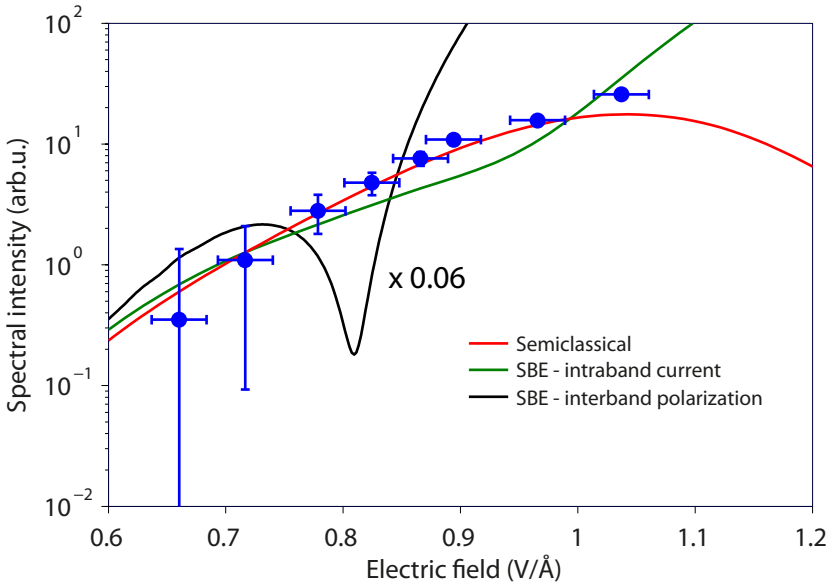

Figure 4.10: Intensity yield of the 11th harmonic in our experiments (blue dots with error bars) compared to semiclassical and quantum-mechanical simulations. The pulse profile is shown in Fig. 4.3a. All the simulations are done using the $\Gamma - M$ direction. Error bars depict the standard deviations of the values extracted from several data sets recorded under identical conditions. Adapted from [196].

Role of dephasing

As a next step, we investigate the importance of the phenomenological dephasing time that is included in the SBEs (Eq. 4.7aa). Fig. 4.11 shows the results of a quantum-mechanical simulation for 1.5-cycle pulses using the dephasing time $T_2 = 27$ fs and the field strength $E_0 = 0.7$ V/Å.

Fig. 4.11a illustrates nicely the time dependent electron wavepacket dynamics in the conduction band. One can observe easily the existence of the bubbles which is a strong indication of the interband polarization as a function of time. Furthermore, not only the interband polarization is indicated but also the intraband excitations are revealed very well as explained next. Along the **k**-axis, the electron wave packet is dragged (accelerated/decelerated) by the electric field and eventually when the electron wave packet is dragged to the edges of the zone, Bloch oscillation occurs as illustrated by the arrows.

Additionally, we split the intraband and interband terms in the calculation and plot their associated intensity profiles ($|P_{\text{inter}}|^2$ and $|P_{\text{intra}}|^2$, filtered in the region > 15 eV) and their spectra $S_{\text{inter}}(\omega)$, $S_{\text{intra}}(\omega)$ as well as their total spectrum $S_{\text{total}}(\omega)$ (Fig. 4.11b-f). The results show that all the spectra exhibit a strong component at ~ 16 eV. However, only the intraband current has significant spectral intensity at higher photon energies. There exits also harmonic structure in the intraband spectrum. In contrast, the interband term and the total spectrum have very little spectral components higher than 20 eV (the interband term is much stronger in amplitude thus it dominates the total spectrum). In conclusion, at the current setting of the dephasing time and the electric field strength, the spectra produced by only the intraband excitation show similar cutoff energy as the experimental ones. However, the spectra produced only by the interband excitation (or

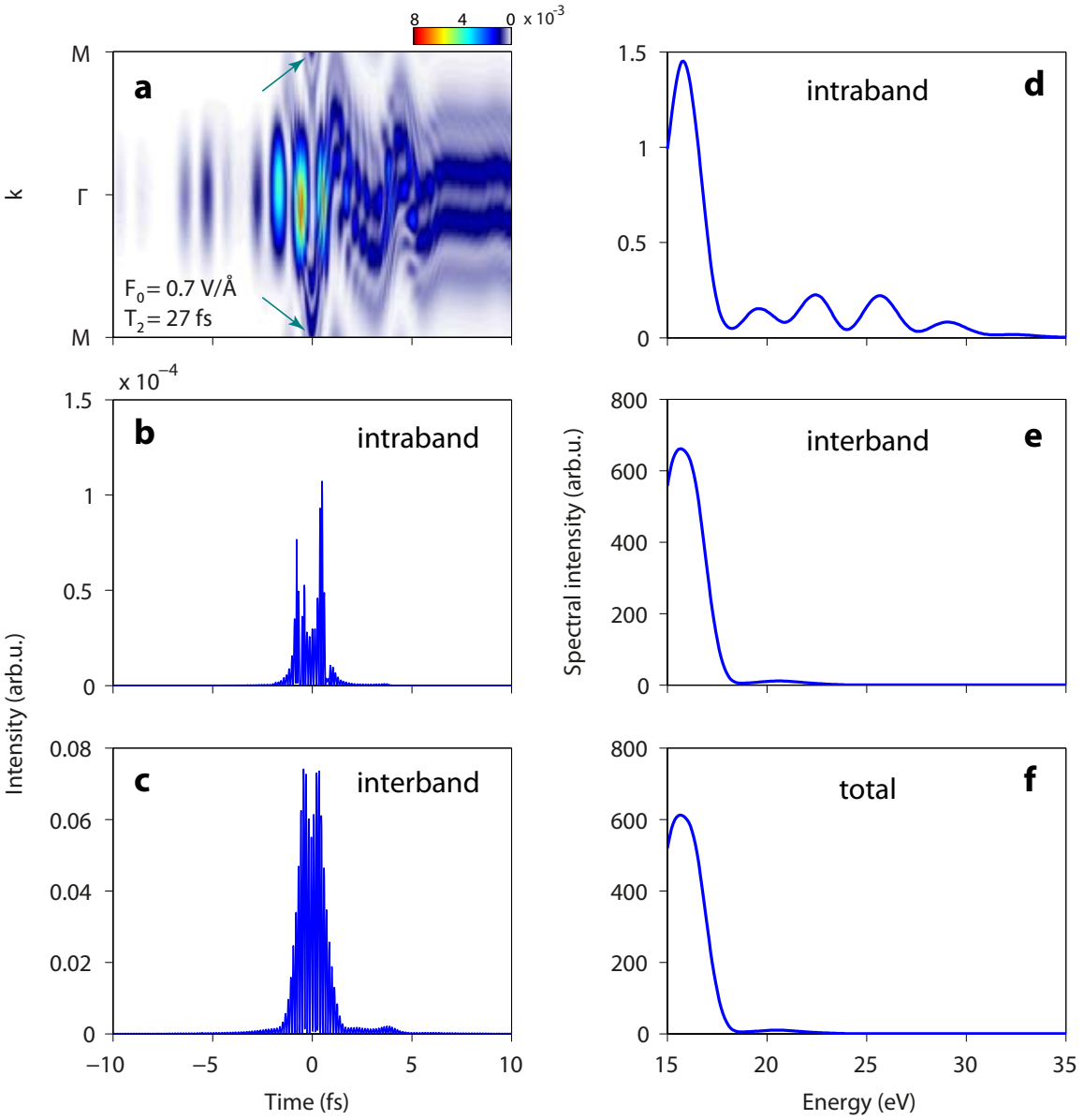

Figure 4.11: Two-band quantum-mechanical simulations for 1.5-cycle pulses ($E_0 = 0.7$ V/Å). The exact electric field is taken from Fig. 4.3a. **a,** Temporal dynamics of the electron wavepacket in the conduction band calculated for the peak field strength $E_0 = 0.7$ V/Å and dephasing time $T_2 = 27$ fs. **b, c,** Temporal intensity profiles of the EUV field induced by intraband current and interband polarization, respectively, in the spectral region > 15 eV. **d, e, f,** Spectra induced by intraband, interband polarization, and total contributions. All spectra are convoluted with 1 eV experimental resolution to ease comparison with the experiment. Arrows indicate one instance of Bloch oscillations. Adapted from [196].

total excitations) do not show similar trend.

By further reducing the dephasing time, the interband spectra seem to increase the cutoff energy and show the harmonic-like spectrum as recorded experimentally. Nevertheless, only reducing the dephasing time is not enough, in order to get close agreement to experimental spectra, we had to increase the electric field strength (up to ~ 3 time

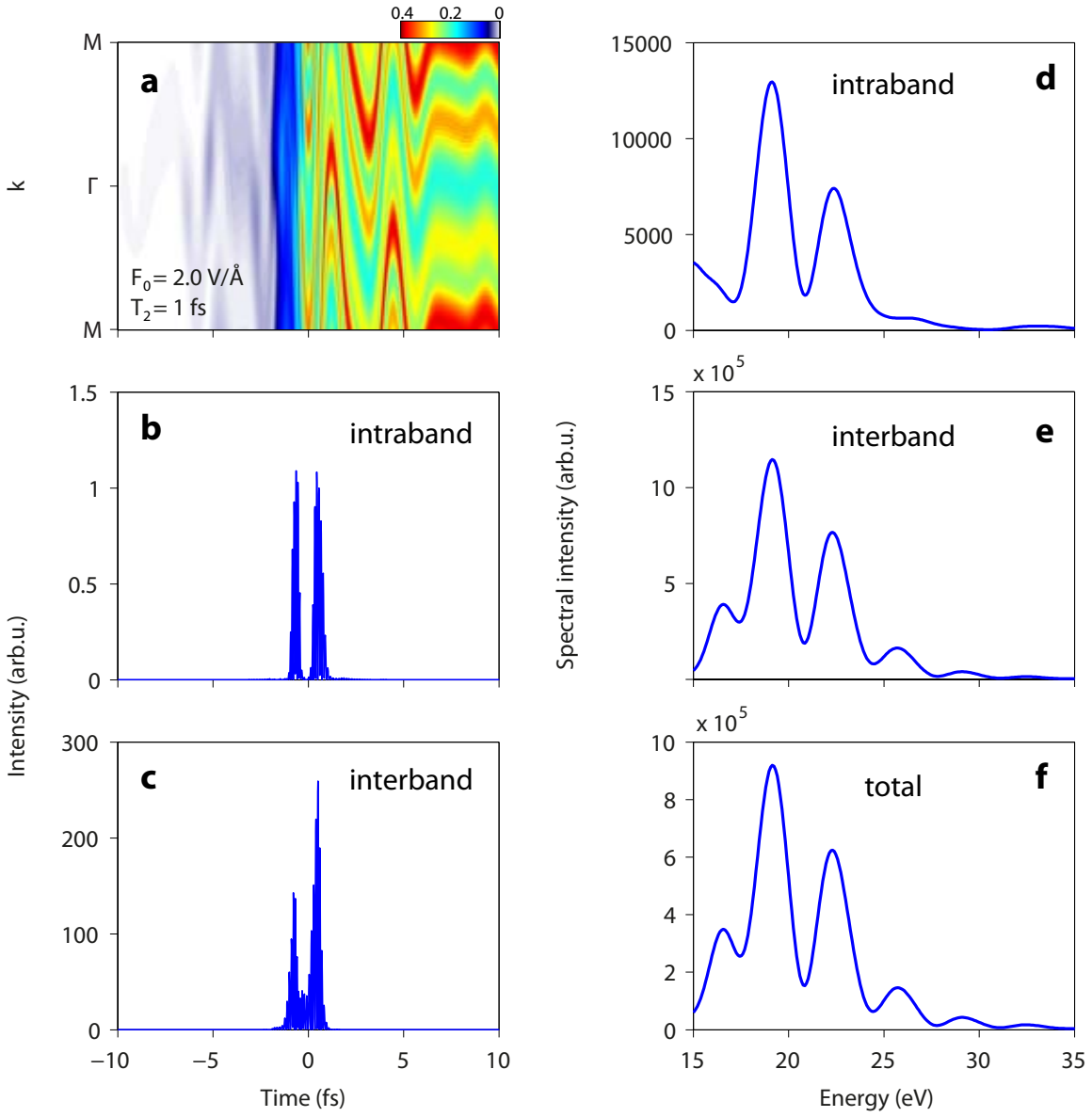

Figure 4.12: Two-band quantum-mechanical simulations for 1.5-cycle pulses ($E_0 = 2$ V/Å). The exact electric field is taken from Fig. 4.3a. **a,** Temporal dynamics of the electron wavepacket in the conduction band calculated for the peak field strength $E_0 = 2$ V/Å and dephasing time $T_2 = 1$ fs. **b, c,** Temporal intensity profiles of the EUV field induced by intraband current and interband polarization, respectively, in the spectral region > 15 eV. **d, e, f,** Spectra induced by intraband, interband polarization, and total contributions. All spectra are convoluted with 1 eV experimental resolution to ease comparison with the experiment. Adapted from [196].

stronger). Fig. 4.12 illustrates a typical result at the dephasing time $T_2 = 1$ fs and electric field strength $E_0 = 2$ V/Å. Firstly, the temporal electron dynamics (Fig. 4.12a) shows a substantially strong interband excitation. The absolute maximum population is ~ 0.4 which is extremely high because it means that almost half of the electrons are removed from the valence band and put into the conduction band and at this regime, even mul-

tiple band simulations are not realistic enough. At this regime of electric field intensity, there is also a lot of Bloch oscillations resulting from very strong intraband currents. The collective effects of the ultrafast dephasing time and strong electric field introduce high cutoff energy photons in both intraband and interband spectra. The emitted spectra at this regime agrees to certain extent the measured experimental spectra.

However, an increase of electric field intensity by approximately one order of magnitude is completely unrealistic compared to our experimental conditions. Simulations performed in [215, 216] have also shown that agreement with experimental data can be achieved under assumption of ultrafast dephasing, $T_2 = 1$ fs. Nonetheless, they are all theoretical papers and there has not been any experimental demonstration so far showing such an extremely fast dephasing time, to the best of our knowledge.

In conclusion, these findings highlight the need for more accurate models of electron dephasing, which may overcome the limitations of conventional treatments, e.g., the Markov approximation and the completed-collision limit [217, 218]. For current modeling, we refrain from using unrealistic numbers hence for all simulations afterward, we use $T_2 = 27$ fs ($T_2 = 1$ fs is not realistic in our perspective).

Comparison with experimental data

We performed multiple simulations (quantum-mechanical and semiclassical) on different electric field waveforms, for all cases from few-cycle, 1.5-cycle, single cycle, to half-cycle (optical attosecond light transient). The results are illustrated in Fig. 4.13 and 4.14.

Firstly, by considering the dynamic range created by different electric field waveforms (total of 8 waveforms at different settings) and how excellent is the agreement between the semiclassical results (Fig. 4.13i, t and Fig. 4.14i, t) to the experimental spectra (Fig. 4.4c, d and Fig. 4.5c, d), we can conclude that the semiclassical model captures the experimental results very well. Even though the intraband term of the SBEs also seems to reproduce the experimental spectra (at least by the few-cycle pulses) as in Fig. 4.13g, p, 4.14g, p, by direct comparison, it is still inferior to the semiclassical model. The interband polarization term can hardly make any connection to the experiments.

Secondly, the reasonable reproduction by both the semiclassically and quantum-mechanically simulated intraband currents allows linking the temporal electron dynamics underlying our simulations with those in our experiments. For few-cycle pulses (Fig. 4.13a,b), excitation of the currents and concomitant radiation extend temporally over several field cycles. The current profile (Fig. 4.13c,e, red and blue curves) in this case is temporally displaced by a CEP variation of the optical driving field, but its structure remains virtually unaffected, resulting in nearly in-variable spectra (Fig. 4.13g,i) against the variation of this pulse parameter in agreement with our experiments (Fig. 4.4a). By contrast, half-cycle pulses confine and control electronic currents to the optical cycle (Fig. 4.13l,n) with CEP. This control is manifested in the spectra domain by wideband modulations of the broadband emitted spectra (Fig. 4.13p,t) and their continuum shape to the structured one in accordance with our experiments (Fig. 4.5d).

The CEP-based manipulation of the emitted spectra originated from an extreme nonlinear process has served for years as a paradigm of sub-cycle confinement and control in attosecond physics[12, 29, 219]. Our experiments and simulations support the notion that this paradigm is also applicable for strong field-driven electron dynamics and EUV

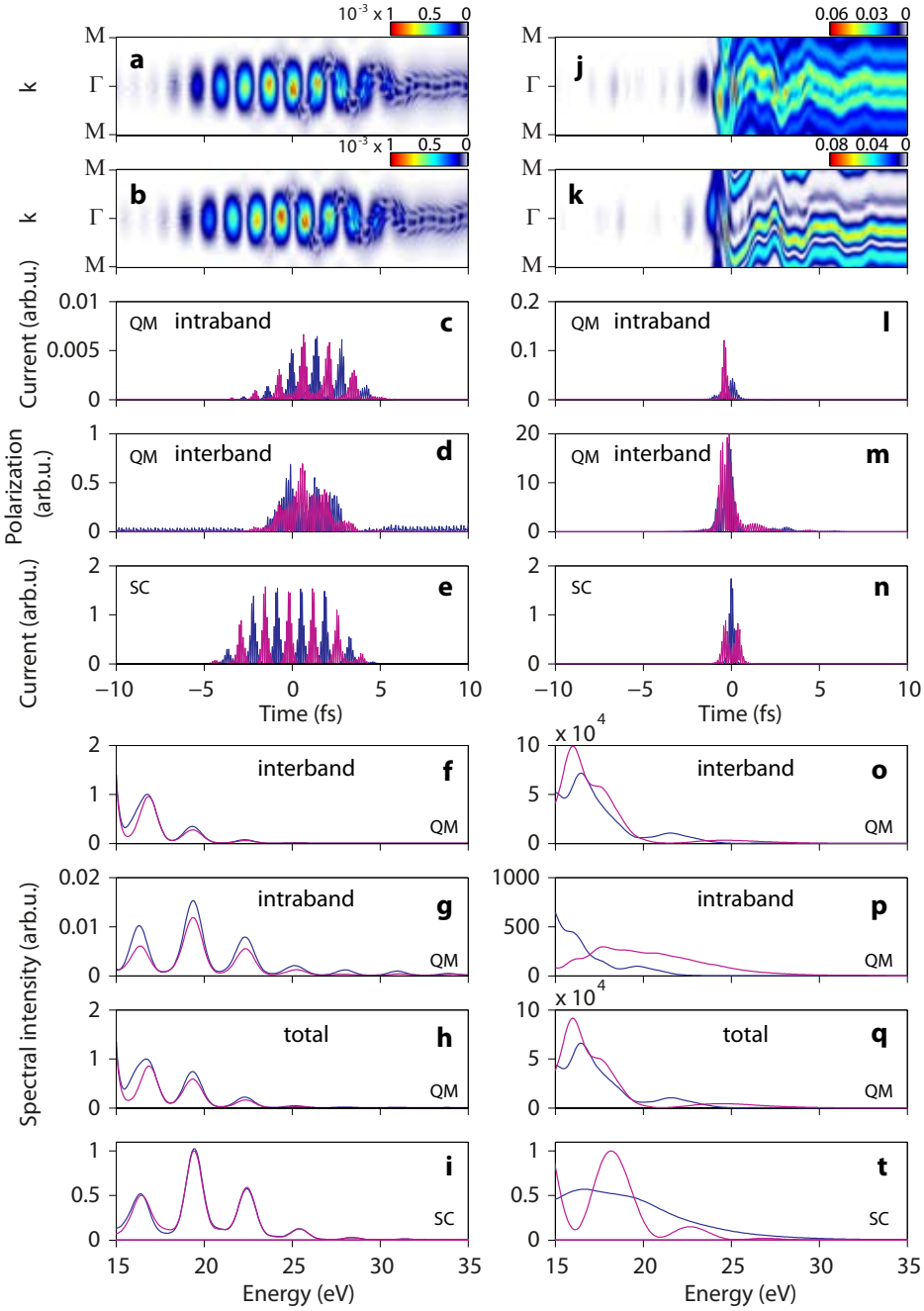

Figure 4.13: Comparison of quantum-mechanical (QM) and semiclassical (SC) models for a few and half-cycle pulse. **a, b,** Temporal dynamics of the electron wavepacket in the first conduction band for few-cycle pulse with $\varphi = 0$ and $\varphi = \pi/2$, respectively (Fig. 4.4a). **c,** Temporal intensity profiles of the EUV field induced by intraband current in the spectral region > 15 eV for $\varphi = 0$ (blue curves) and $\varphi = \pi/2$ (red curves). **d,** Same as **c** but for the interband polarization. **e,** Same as **c,** but calculated from semiclassical model. **f,** Spectral intensity of radiation, induced by interband polarization. **g,** Spectra induced by intraband currents. **h,** Total emitted spectra (inter- and intraband contributions). **i,** Spectra calculated from semiclassical model. **j-t,** same as **a-i** but for the half-cycle pulses (Fig. 4.5b). All spectra are convoluted with 1 eV experimental resolution. Adapted from [196].

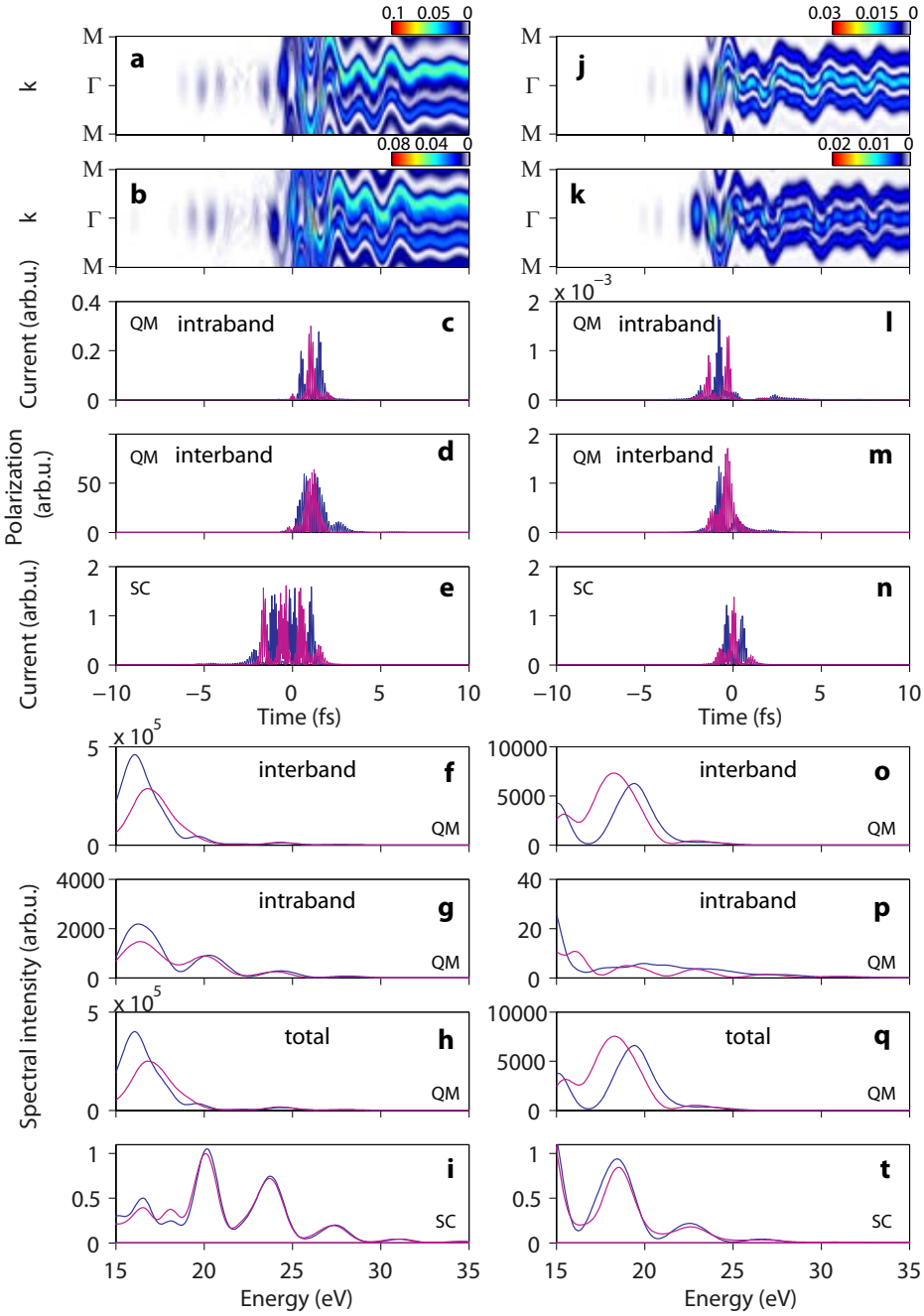

Figure 4.14: Comparison of quantum-mechanical (QM) and semiclassical (SC) models for attosecond light transients. **a, b,** Temporal dynamics of the electron wavepacket in the first conduction band for 1.5-cycle pulse with $\varphi = 0$ and $\varphi = \pi/2$, respectively (Fig. 4.4b). **c,** Temporal intensity profiles of the EUV field induced by intraband current in the spectral region > 15 eV for $\varphi = 0$ (blue curves) and $\varphi = \pi/2$ (red curves). **d,** Same as **c** but for the interband polarization. **e,** Same as **c,** but calculated from semiclassical model. **f,** Spectral intensity of radiation, induced by interband polarization. **g,** Spectra induced by intraband currents. **h,** Total emitted spectra (inter- and intraband contributions). **i,** Spectra calculated from semiclassical model. **j-t,** same as **a-i** but for the single-cycle pulses (Fig. 4.5a). All spectra are convoluted with 1 eV experimental resolution. Adapted from [196].

emission in bulk solids. As half-cycle drivers are confined to a *de facto* sub-femtosecond interval (its duration $\tau < 1$ fs), these broadband spectral modulations offer evidence of the attosecond confinement and control of the induced multi-PHz intraband currents, and represents a unique and generic tool for tracing coherent strong-field dynamics in solids.

Semiclassical description of the HHG beyond the nearest-neighbor approximation

Although the numerical solution of the SBEs and the Boltzmann equation 4.4 can shed light on the generated EUV and its dependence on the parameters, if we notice that basically for certain simple function of the electric fields, the Boltzmann equation 4.4 can be solved analytically and also its resultant current density Eq. 4.6 [207].

In fact, if we assume an electric field: $E(t) = E_0 \cos(\omega_0 t + \varphi)$, and a Bloch frequency $\omega_B = eaE_0/\hbar$ given the band dispersion $E(k)$, it is shown [207] that the peak of the odd harmonics order N in the radiated spectrum can be written as: [196]

$$I_{\text{rad}}(N\omega_0) \propto (N\omega_0)^2 \cdot \mathfrak{J}_N^2 \left(\frac{\omega_B}{\omega_0}\right) \tag{4.11}$$

with $\mathfrak{J}_N$ is the Bessel function of the first kind, order N.

Clearly in this case, the appearance of the Bessel function $\mathfrak{J}_N^2\left(\frac{\omega_B}{\omega_0}\right)$ already indicates a non-perturbative behavior of the radiated spectra. Furthermore, evaluation of the Bessel function at different peak electric fields (ω_B) also supports the nonlinear as well as the saturation behavior of the spectra intensity, as observed experimentally in Fig. 4.3. However, very strong dependence of the radiated spectra on the conduction band dispersion profile (seen in evaluation of SBEs and semiclassical model for different band dispersions) and the above consideration suggested the decomposition of the band dispersion profile into multiple harmonics.

One can decompose the energy dispersion of the i-th band $\mathcal{E}_i(k)$ into the Fourier series

$$\mathcal{E}_i(k) = \sum_{n=0}^{n_{\max}} \epsilon_{i,n} \cos(nka) \tag{4.12}$$

where $n_{\max}$ denotes the maximum number of distant neighbors considered in the model [196].

In this case, the analytical result similar to Eq. 4.11 can be obtained [196]

$$I_{\text{rad}}(N\omega_0) \propto (N\omega_0)^2 \left| \sum_{n=1}^{n_{\max}} n\epsilon_n \mathfrak{J}_N\left(\frac{n\omega_B}{\omega_0}\right) \right|^2 \tag{4.13}$$

note that Eq. 4.13 differs from Eq. 4.11 by the $\sum$ and the n factor both inside the sum as well as in front of ω_B inside the Bessel function. Eq. 4.13 has a big advantage in interpreting our experimental data thanks to it fast evaluation.

Figure 4.15 summaries all the important features one could derive from Eq. 4.13 as well as the natural idea behind it. By investigating and understanding the influence of the conduction band structure, the electric fields to the radiated spectrum, we selectively choose the conduction band in Γ–M direction (Fig. 4.15a) as calculated by Schlüter

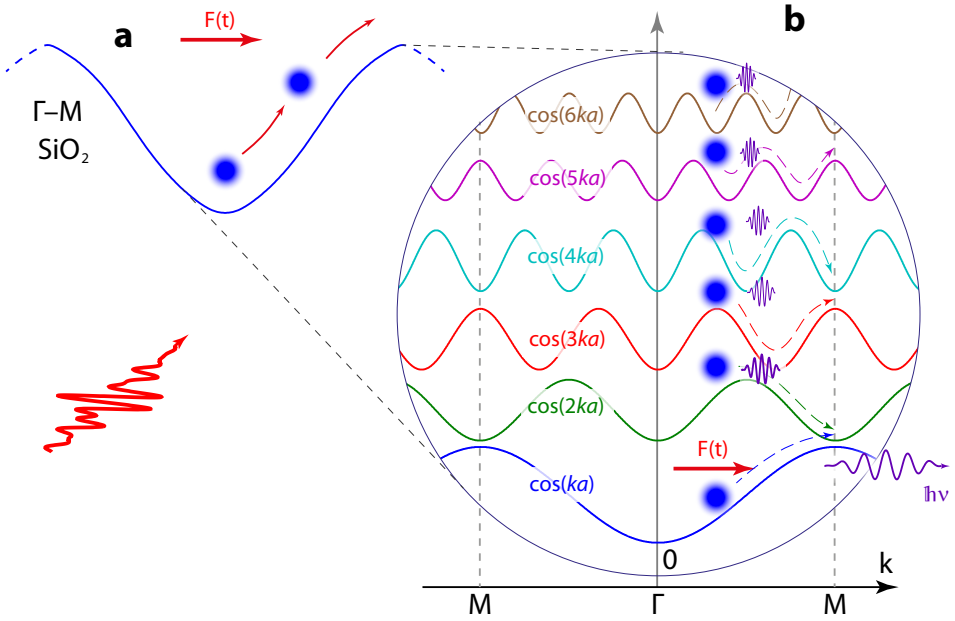

Figure 4.15: Semiclassical picture of the field-driven electron dynamics in SiO_2. **a,** An electron wavepacket driven by the field in the lowest conduction band along the $\Gamma - M$ direction of the Brillouin zone. **b,** Spatial harmonic components of the band dispersion resulting from Eq. 4.12. Relative amplitudes are scaled, for clarity. Adapted from [196].

[191]. Even though the selection of this band was explained in subsection 4.3.3, we can qualitatively add to the fact: (i) this is the lowest conduction band that is the most isolated from higher bands. The highest energy spacing between this band and the next bands ensures the least probability for the electron wave packet to do interband transitions [202], keeping most of the electron wave packet within the same band, allowing only Bloch oscillations and influencing the Bragg scattering from collisions of the electron wave packet to the band as well as to the Brillouin zone edges. (ii) Furthermore, by spanning close to 3.5 eV, this band provides relatively large group velocity v_g to the electrons that eventually contributes to the generated current or radiated spectrum. As a result, this conduction band contributes as a highest weight in the total radiated spectrum if accounted for all the bands (Fig. 4.9). In particular, this band can be decomposed into its Fourier series with higher frequency components as in Fig. 4.15b. Because a $\cos(ka)$ function could represent most of the band structure, all the higher order terms $\cos(2ka)$, $\cos(3ka)$, $\cos(4ka)$, *etc* exist in the decomposition but with much weaker weights. Therefore they have to be scaled up to be visible at the same amplitude of the first $\cos(ka)$ term.

Acceleration or deceleration of the electron wave packet in the first term $\cos(ka)$ automatically mean a lot higher acceleration (deceleration) or a lot more oscillations in the same time window on the higher terms $\cos(2ka)$, $\cos(3ka)$, $\cos(4ka)$, *etc* in the decomposition. Naturally the same incident electric field can drive the electron wave packet to generate photon $\sim \omega_B$ in the lowest order term but if we consider the higher order terms, this same electric field can generate photon $\sim n \cdot \omega_B$.

Because the electric fields used in our experiment are in principle more complex than just the cosinusoidal approximation ($E = E_0 \cos(\omega t)$) thus in order to get a realistic picture, we conducted the semi-classical simulation using the separately decomposed bands

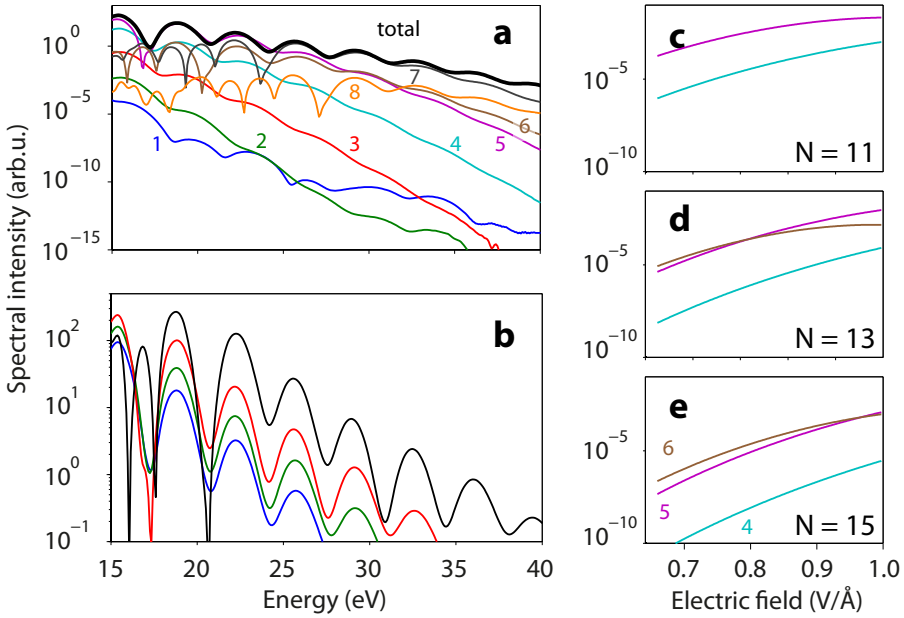

Figure 4.16: Semiclassical picture of the field-driven electron dynamics in SiO_2 - continued. a, Contributions to the EUV spectra from each of the spatial harmonics for the field of Fig. 4.3a at the amplitude $E_0 = 0.8$ V/Å. The total emitted spectrum (black curve) aggregates contributions from all spatial harmonics. **b,** Simulated spectra for the electric field waveform (Fig. 4.3a) for the realistic band shown in Fig.4.15a as a function of the peak field strength E_0. Color-coding corresponds to field strengths of Fig. 4.3b. **c, d, e,** Contributions of spatial harmonics $n = 4$, 5, 6 to the intensity yields of EUV harmonics of orders $N = 11$, 13, and 15 versus field amplitude E_0. Adapted from [196].

(Fig. 4.15b) under a same electric field as in Fig. 4.3a. The results are illustrated in Fig. 4.16a. Evidently, being excited by the same electric field, the lowest order term, $\cos(ka)$ has a very fast dropping cutoff (solid blue curve). The spectra generated by progressively higher order terms reach higher cut off and eventually the calculation using the complete $\Gamma - \mathrm{M}$ band structure (all terms in the decomposition are included) generates strongest intensity as well as the highest cut off energy (solid black curve). In the other words, the higher the terms involved in the decomposition, the higher the cut off energy the generated spectra will exhibit at this current electric field strength. At higher electric field strength, the saturation of the Bessel function makes it hard to predict the behavior of the spectral components as well as cutoff energies.

Intensity scaling measurements and spectroscopy application

If the first conduction band in the Γ–M direction in [191] is represented by a series of spatial harmonics, it will be rewritten as (in eV unit):

$$\mathcal{E}_c(k) = 10.6 - 1.669\cos(ka) + 0.0253\cos(2ka) - 0.0098\cos(3ka) \tag{4.14a}$$
$$+ 0.0016\cos(4ka) + 0.0263\cos(5ka) - 0.0052\cos(6ka) \tag{4.14b}$$
$$+ 0.0103\cos(7ka) + 0.0005\cos(8ka) + \ldots \tag{4.14c}$$

By applying this Fourier series on the incident electric field as in Fig. 4.3a for a variety of field strengths as used in the experiment, the semiclassical simulations (Fig. 4.16b) yield an excellent agreement with experimental spectra (Fig. 4.3b).

Furthermore, evaluation of the Eq. 4.11 for each of the high order spatial harmonic terms (4a, 5a, 6a) as a function of the incident field strengths are shown in Fig. 4.16c,d,e (for 11^{th}, 13^{th}, 15^{th} harmonic order respectively). Clearly, different spatial harmonic orders have different intensity scaling laws and they exhibit either exponential (4a, 5a) or saturated scaling behavior (6a in Fig. 4.16c,d,e). With the combination of them represented by Eq. 4.13, another strong agreement between this simulation and the experimental results can be reached, as illustrated in Fig. 4.17.

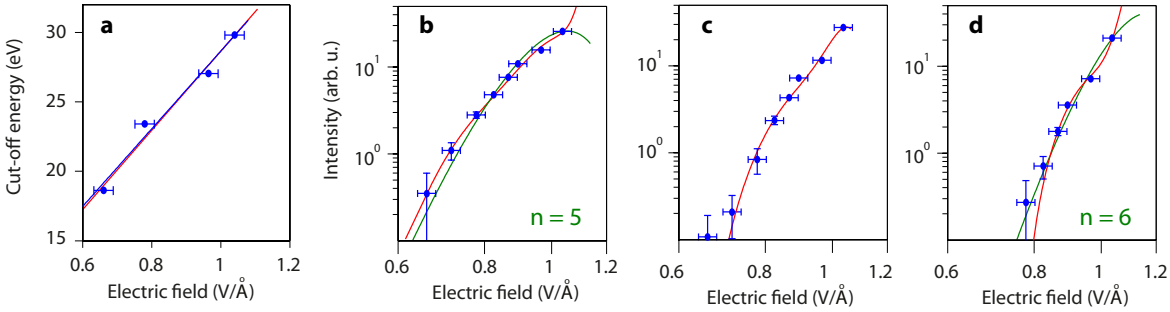

Figure 4.17: Energy cutoff and intensity scaling of EUV emission in SiO_2. a, Scaling of the cutoff energy E_{cutoff} (blue dots with error bars) with the field amplitude E_0. Linear fitting of the measured data (blue line) and results of semiclassical simulations (red line). b, c, d, Yield dependence for harmonics of order $N = 11$, 13, and 15 on the field amplitude (blue dots). Red curves represent fittings based on the Eq. 4.13 , including all spatial harmonics up to n_{max}. Green curves in b, d, represent the fittings of experimental data with Eq. 4.13, where only one spatial harmonic ($n = 5$ and $n = 6$, respectively) was taken into account. Error bars depict the standard deviations of the values extracted from several data sets recorded under identical conditions. Adapted from [196].

It is not straight forward to verify the cutoff scaling law (linear dependence of the cutoff energy versus the electric field strength) analytically because our electric fields are not representable analytically. (For the case of a constant electric field, the linear dependence is trivial via the Bloch frequency formula $\omega_B = aeE/\hbar$). However, it is fairly easy to verify this numerically. In fact, numerical simulations using either Eq. 4.13 or the solving the Bolztmann equation (Eq. 4.4) both give a consistent result that is the linear dependence of the cutoff energy versus field strength. Evidently, one can see a strong agreement between the measured dependency and the simulated linear dependence in Fig. 4.17a.

The key advantage of the Eq. 4.13 is that its allow one to investigate the scaling of spectral intensity as a function of the incident electric field strength in the approximation of the cosinusoidal form. Therefore, we try to use Eq. 4.12 as a basis and fit Eq. 4.13 to the experimental data and we expect to get back the band dispersion in the representation of multiple high order spatial harmonics. The results of the fitting can be summarized as follows:

- **Excellent fitting:** As one can observe in Fig. 4.17b, c , d, the degree of agreement between the measured data (blue dots) and the fitted results (red curves) is great. Because the data are represented in the logarithmic y-axis thus while the fitting is done in the linear scale, it means that a small deviation in the weak field strength ~ 0.6 V/Å is negligible. In fact, all of the deviation between experimental data and fitted results are well within the error bars of the experiments.

- **Only few spatial harmonic orders play a role:** The results of the fitting suggest that not all the spatial harmonic orders, for instance 1a to 8a in this particular fitting, are of equal importance. In particular, it was found out that only certain orders, mostly 5a and 6a, are the main component in the fitting. Again, Fig. 4.16a has given us a clear explanation: only these orders and higher orders are contributing the most in the emitted EUV in this spectral range (for this given electric field). Hence the highest contributing terms will certainly play more important role in determining the generated spectral intensity, and consequently showing up in the result of the fitting.

- **Fine details of the band dispersion is captured:** Because we cannot calculate the absolute values of the spectral intensity as well as the imperfect calibration of the measured spectra, we cannot extract the absolute ϵ_n from the fitting. However, the ratio between the ϵ_n is maintained due to the fact that each spatial harmonics gives different scaling laws (Fig. 4.16c,d,e) thus the combination of them is unique and it is this unique combination which is reconstructed through the fitting. In particular, from the fitting we have $\epsilon_5/\epsilon_6 \sim -5.1 \pm 0.6$ which is almost identical to the calculated value ($\epsilon_5/\epsilon_6 \sim -5.6$) of the first conduction band of SiO_2 in the Γ–M direction (Eq. 4.14) [191]. Semiclassical simulations take into account only these two terms (ϵ_5, ϵ_6) produce almost identical spectra compared to Fig. 4.13, 4.14 where the complete series of bandstructure in the Γ–M direction is included.

In conclusion, not only the Fourier decomposition of the band dispersion profile helps interpreting the experimental data, explaining the physical nature of the emitted EUV but it also further advances our capability by extracting the correct parameters representing the band dispersion profile. Spectroscopically, this opens the door to measuring in the most direct way the dispersion profiles of the conduction bands. If one wants to calculate the resolution of this technique, a sensitivity to the 6^{th} spatial order means a crystal momentum resolution of $\pi/(6a) \sim 0.1$/Å which is nearing that of modern angular resolved photoemission spectroscopy [220].

Linear fit of the cutoff energy scaling

Close inspection of the Eq. 4.13 reveals that for maximum number of distant neighbors included in the consideration $n_{\max}$, the highest characteristic distance in the crystal is $R_{\max} = n_{\max}a$ and consequently the maximum energy that a photon can be emitted from driven electrons is $E_{\max} = n_{\max}\hbar\omega_B$. This suggest the maximum measured cutoff energy is linearly dependent on the electric field strength (through ω_B) as well as the effective maximum number of distant neighbors ($n_{\max}$).

In fact, Fig. 4.18 shows that if a linear fitting of the experimental data is performed we found out $R_{\text{cutoff}} \sim 30$ Å and $n_{\text{cutoff}} = 6.2 \pm 0.5$. Furthermore, extrapolation of the

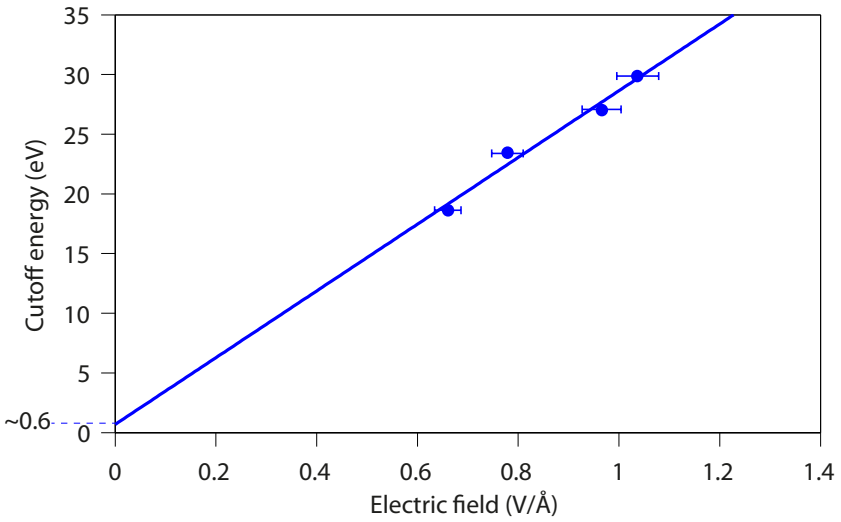

Figure 4.18: Linear fit of the experimental cutoff energy versus field (extension of Fig. 4.17a). Blue line is the linear regression with the least squares method, which gives the cutoff energy $E_{\text{cutoff}} = 0.6 \pm 2.0$ eV at $E_0 = 0$. Adapted from [196].

linear fitting to zero field $E_0 = 0$ yields a cutoff energy $E_{\text{cutoff}} = 0.6 \pm 2.0$ eV. This additionally strengthens the link between the emitted radiation and the induction of intraband currents considered in the semiclassical model where $E_{\text{cutoff}} = 0$ at zero field is predicted.

Experimental setup for beam profile measurement

After characterizing the electric fields by the attosecond streaking, we replaced the streaking target by the ultrathin SiO_2 sample as in Fig. 4.19a. After making sure that there is only well characterized optical beam reflected on the outer mirror, the small annular beam is focused onto the SiO_2 sample. Because the incoming beam is annular, any generated coherent photons will be directed collinearly to the axis of propagation of the incident electric field. One thin aluminium filter ($\sim$ 100 nm) is placed after the sample, before the multi-channel plate (MCP).

A simple imaging setup was installed to project the beam profile of the EUV ($>$ 15 eV) radiation on the phosphor's screen onto our camera. The measured profile (after calibration) Fig. 4.19b shows a well behaved, Gaussian-like beam. The ellipticity is calculated through 2D Gaussian fitting of the real beam profile and turns out to be ~ 0.9. The beam width evaluated by full width at half maximum (FWHM) is ~ 4.8 mm and by $1/e^2$ is ~ 9.0 mm for the broad axis and for the other axis are ~ 4.2 and ~ 7.7 mm respectively. Therefore, the calculated divergence of the beam from the averaged FWHM value is $\theta \sim 5.2$ mrad.

Spatial profile and coherent of the generated EUV beam

Additionally, one can further study the measured beam profile in the far field and try to contrast it with the simulated one using above described theory. Because the generated EUV spectra are different at different incident electric field strengths, naturally

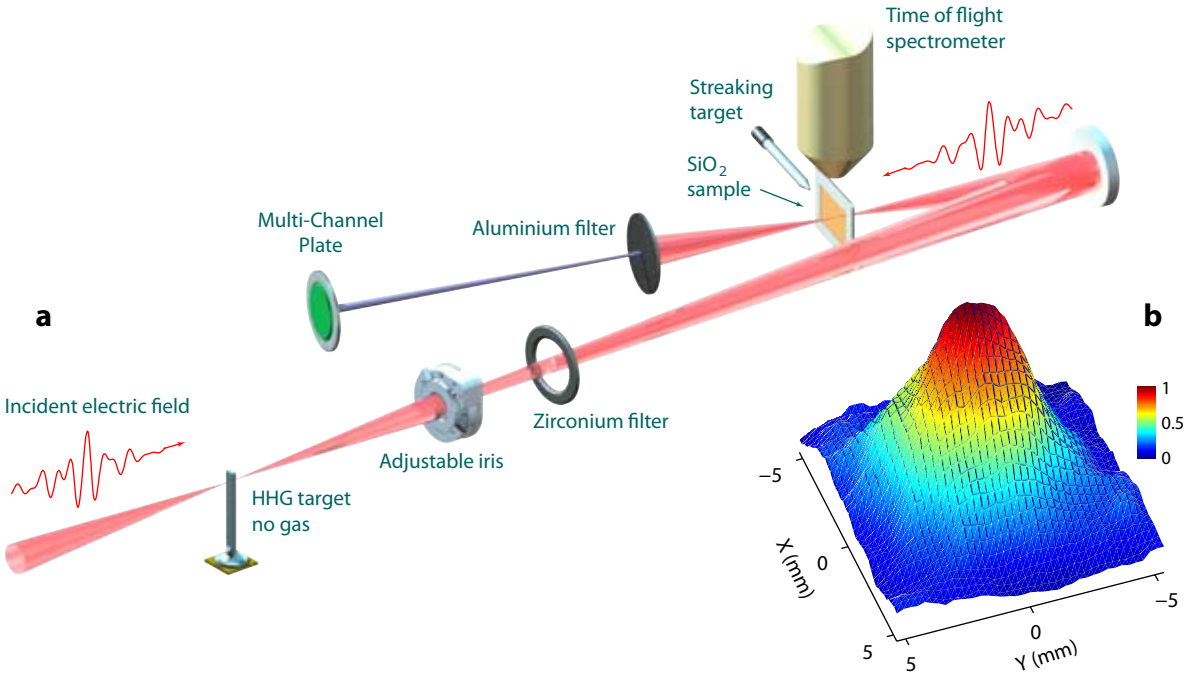

Figure 4.19: Measurement of the coherent EUV radiation beam profile. a, Ultrawideband pulses (bandwidth $\sim 1.1 \rightarrow 4.6$ eV) which are synthesized after a light field synthesizer and characterized by attosecond streaking. Red waveform represents 1.5-cycle pulses as incident electric fields. The SiO_2 sample replaced the position of the streaking target afterward. **b,** 3D plot of the captured EUV beam profile taken from an multi-channel plate/phosphor image intensifier which is placed ~ 87 cm downstream from the sample. One aluminium filter (~ 100 nm) is installed to block the driving electric field frequencies.

this will lead to an evolution of emitted EUV spectra across the focal spot of the incident beam. Studies of space-time characteristics of this type are very important and eventually support the characterization of electric fields in femtosecond and attosecond regimes [16, 221]. Since in our case the laser beam profile is relatively big ($\sim 20\,\mu$m, Fig. 4.20a,b), we can safely assume that there is no cross talk between different positions on the focal spot. Therefore, we could use directly the intensity scaling simulation (calculated semiclassically) results together with the intensity profile of the incident electric field to generate a spatially resolved EUV spectrum as displayed in Fig. 4.20c for the case the peak field strength is ~ 1.04 V/Å. This shows how different spectral components are generated at different positions on the focal spot (on the sample). It is clear that mainly the odd harmonics are being generated. The size of the them as well as their intensities gradually decrease as we look at higher photon energies. As a consequence, the total emitted EUV profile (Fig. 4.20d) is mainly dominated by the $15-20$ eV photon energies.

Nonetheless, this is the simulated beam profile emitted at the generation point (near field), the beam in the far field can be calculated from linear propagation. In this case, we have to use the wave equation A.6 neglecting the polarization term because this beam propagates in vacuum.

$$\left(\nabla^2 + k^2(\omega)\right)\mathbf{E}(\mathbf{r},\omega) = 0 \tag{4.15}$$

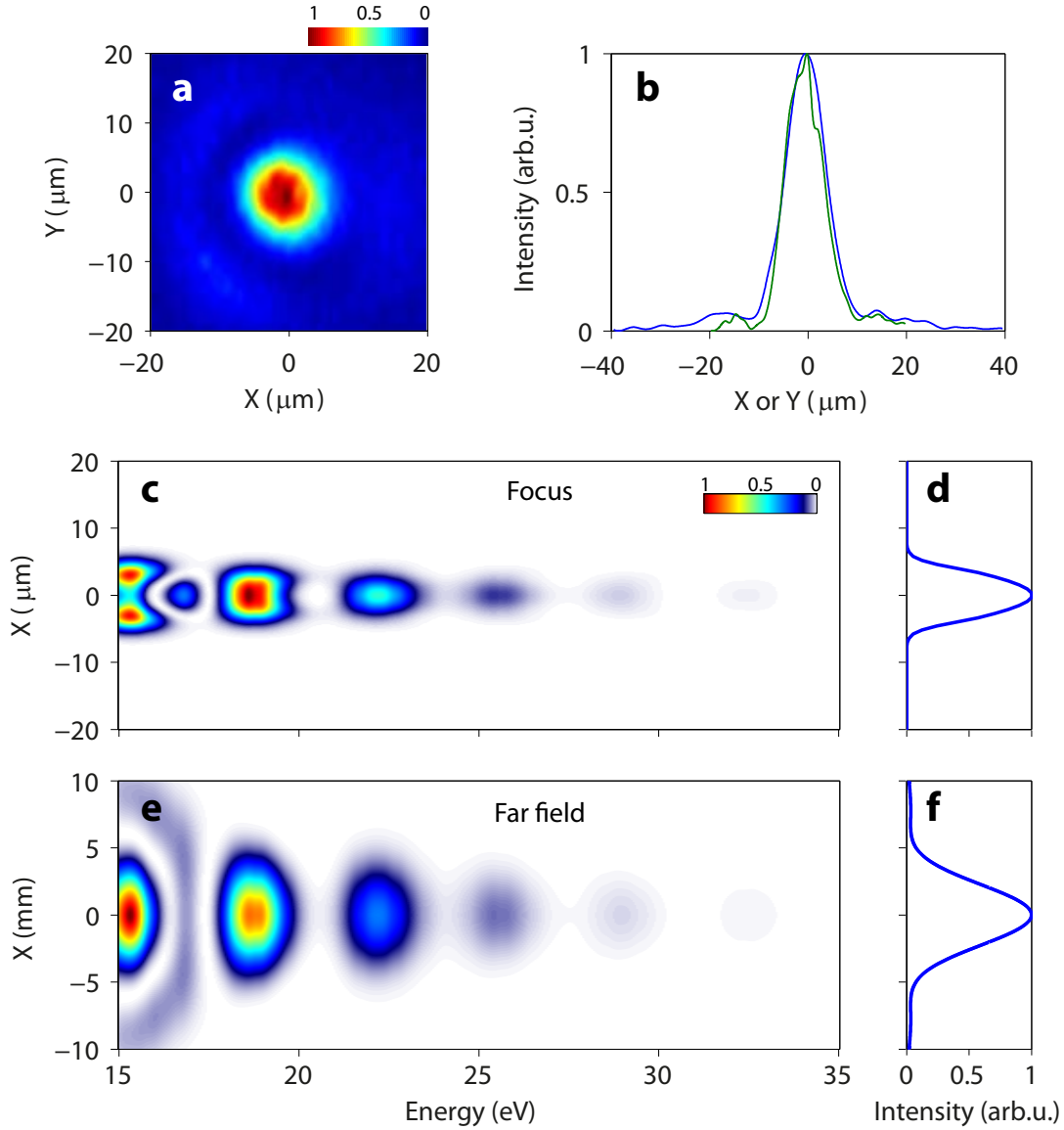

Figure 4.20: Spatially resolved EUV spectrum in the near and far field (simulation). **a,** Measured laser beam profile in the focus. **b,** Cross sections of the laser beam profile along X and Y-axis. **c,** Generated EUV spectral intensity as a function of the photon energy across the beam profile. **d,** Integrated EUV beam profile in the near field. **e, f,** Same as **c** and **d**, but for the far field (note the difference of y-axes units between **c** and **e**). Adapted from [196].

By applying the envelope decomposition [222] as in Eq. A.7 and *slowly varying amplitude approximation*, after some steps we have:

$$2ik(\omega)\frac{\partial \mathbf{U}(\mathbf{r},\omega)}{\partial z} + \frac{\partial^2 \mathbf{U}(\mathbf{r},\omega)}{\partial x^2} + \frac{\partial^2 \mathbf{U}(\mathbf{r},\omega)}{\partial y^2} = 0 \tag{4.16}$$

which is very similar to the *first order propagation equation in frequency domain*, A.9. If we transform $\mathbf{U}(\mathbf{r},\omega)$ to its k-space using Fourier transform: $\mathbf{U}(kx, ky, z, \omega) = \mathfrak{F}_{2\mathfrak{D}}\big[\mathbf{U}(\mathbf{r},\omega)\big]$

and make use of the Fourier identity A.4, Eq. 4.16 becomes:

$$2ik(\omega)\frac{\partial \mathbf{U}(kx,ky,z,\omega)}{\partial z} = (kx^2+ky^2)\mathbf{U}(kx,ky,z,\omega) \tag{4.17a}$$

$$\implies \quad \mathbf{U}(kx,ky,z,\omega) = \mathbf{U}(kx,ky,0,\omega)\cdot e^{-iz\frac{kx^2+ky^2}{2k(\omega)}} \tag{4.17b}$$

From Eq. 4.17bb, we can finally calculate the profile $\mathbf{U}(x,y,z,\omega)$ given the initial profile $\mathbf{U}(x,y,0,\omega)$ by the following expression:

$$\mathbf{U}(x,y,z,\omega) = \mathfrak{F}_{2\mathfrak{D}}^{-1}\Big[\mathfrak{F}_{2\mathfrak{D}}\big[\mathbf{U}(x,y,0,\omega)\big]\cdot e^{-iz\frac{kx^2+ky^2}{2k(\omega)}}\Big] \tag{4.18}$$

Applying Eq. 4.18 to the generated EUV profile in the near field as in Fig. 4.20c, we get the EUV profile Fig. 4.20e in the far field, after $\sim$ 87 cm of propagation as in the experiments. Because the wave equation is solved in free space thus there is no coupling between the frequencies thus the harmonic structure in the near field remains the same in the far field. However, the beam profile of the 19 eV components seems to be bigger than 15.5 eV components in the far field and there is a halo around the lowest frequencies that results in a weak ring in the total beam profile Fig. 4.20f.

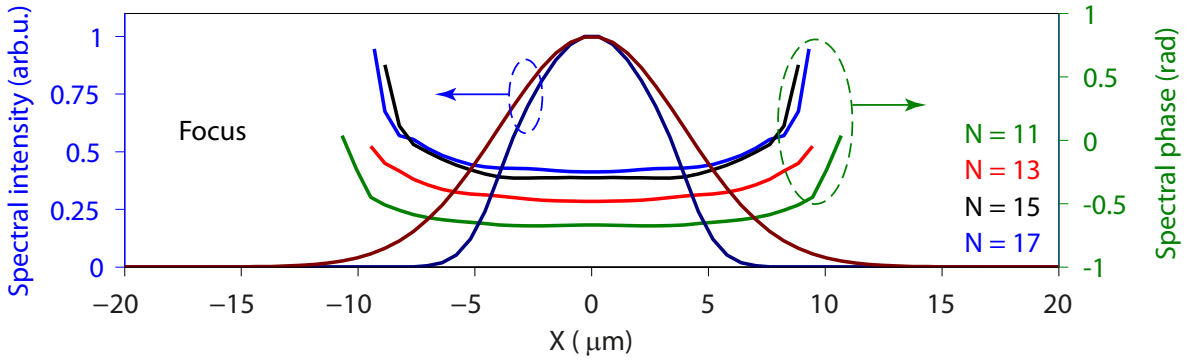

Figure 4.21: Intensity and phase profiles of the EUV harmonics in the focus. Spatial profile of the laser field (solid sepia curve). Solid dark blue curve is the spectrally integrated EUV profile (see Fig. 4.20d). Spatial phase profiles of different EUV harmonic orders N = 11, 13, 15, 17 are shown by solid green, red, black, and blue curves, respectively. Adapted from [196].

According to Fig. 4.21, there is a very small phase shift of the emission latterally across the pump focal spot. From the direct comparison of the X-axis profile of the measured and simulated beam in the far field (Fig. 4.22), excellent agreement has been observed. The simulated EUV beam profile in the far field has the width $\sim 9.0 \pm 1.0$ mm while the measured profile (Fig. 4.19b) has the width $\sim 9.0 \pm 0.8$ mm, defined via $1/e^2$. This remarkable agreement suggests the coherence of the emitted radiation and supports the validity of the semiclassical model of HHG.

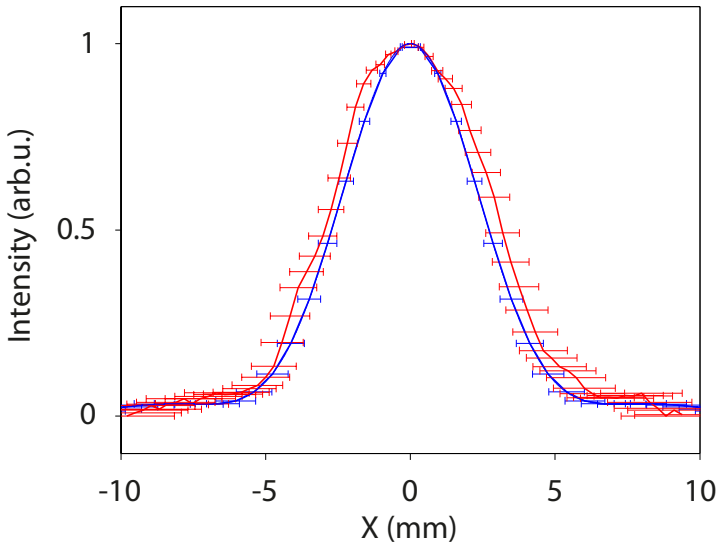

Figure 4.22: Comparison of measured and simulated beam profile. X-axis profile (red curve) of Fig. 4.19b and far field beam profile (blue curve) calculated using semiclassical model and free space propagation. Error bars depicted the standard deviation of the values extracted from several data sets recorded under identical experimental conditions. Adapted from [196].

4.4 Further considerations

4.4.1 Phase matching (first order propagation) consideration of EUV radiation in SiO_2 thin films

The two models above which helped us to understand the basics of physical processes inside bulk crystals and their associated EUV radiation are just fundamental first steps. EUV radiation at source points can only be detected at the detection points if the generated photons undergo significant coherent build-up such that they arrive on detectors at measurable intensity. Due to the fact that hardly any material has constant refractive indexes over the ultrabroad range from the fundamental carrier frequency to the EUV frequencies, the fundamental carrier wave will travel at different speed compared to the EUV photons which are generated by the fundamental waves. Hence the generated EUV photons will lag behind (in most cases) compared to the fundamental waves as they propagate though a medium. After a certain amount of propagation distance, the previously generated EUV photons will acquire enough phase mismatch that makes destructive interference with their newly generated photons. This leads to the oscillation of the total generated EUV intensity along the propagation axis and it undoubtedly limits the ultimate intensity that could be generated significantly.

There are different ways to minimize the difference in propagation speed, enhance the total coherent build-up, and ensure the phase matching capability of the fundamental waves and generated high frequency waves, these are called phase matching optimizations [75]. Although the most precise and accurate way to calculate the total optical response of a system finally is to solve the Maxwell's equations in conjunction with a model that describes the generation processes (semiclassical model or SBEs in this case), it is rather complicated because it includes dispersion (or absorption, gain), diffraction and all kinds

of other spatial effects. One might try to reduce the complexity from a 3-D calculation to a 1-D calculation. However, because our spectral region of interest is so broad, its phase matching requirements will be difficult to achieve. Constant *et al.* [194] has suggested a convenient way to consider phase matching optimizations and demonstrated HHG with high conversion efficiency ($\sim 4 \cdot 10^{-5}$). Since the principles of phase matching consideration apply to all kinds of media, we calculate our phase matching requirements based on their work [194]:

$$\mathbf{L}_{\mathrm{m}} > 3\mathbf{L}_{\mathrm{a}} \tag{4.19a}$$

$$\mathbf{L}_{\mathrm{c}} > 5\mathbf{L}_{\mathrm{a}} \tag{4.19b}$$

Here $\mathbf{L}_{\mathrm{m}}$ is the length of the medium, the attenuation (or absorption) length $\mathbf{L}_{\mathrm{a}}$ is defined as: $\mathbf{L}_{\mathrm{a}} = c/(2\omega k) = c\hbar/(2E_k)$, E_k is the photon energy of the wave vector k in consideration. The coherence length $\mathbf{L}_{\mathrm{c}}$ is defined as: $\mathbf{L}_{\mathrm{coherence}} = 2\pi/\Delta k$, $\Delta k = n_q/\lambda_q - q \cdot n_0/\lambda_0$ is the wave vector mismatch between the fundamental λ_0, with refractive index n_0 and the q^{th} harmonics λ_q, with refractive index n_q.

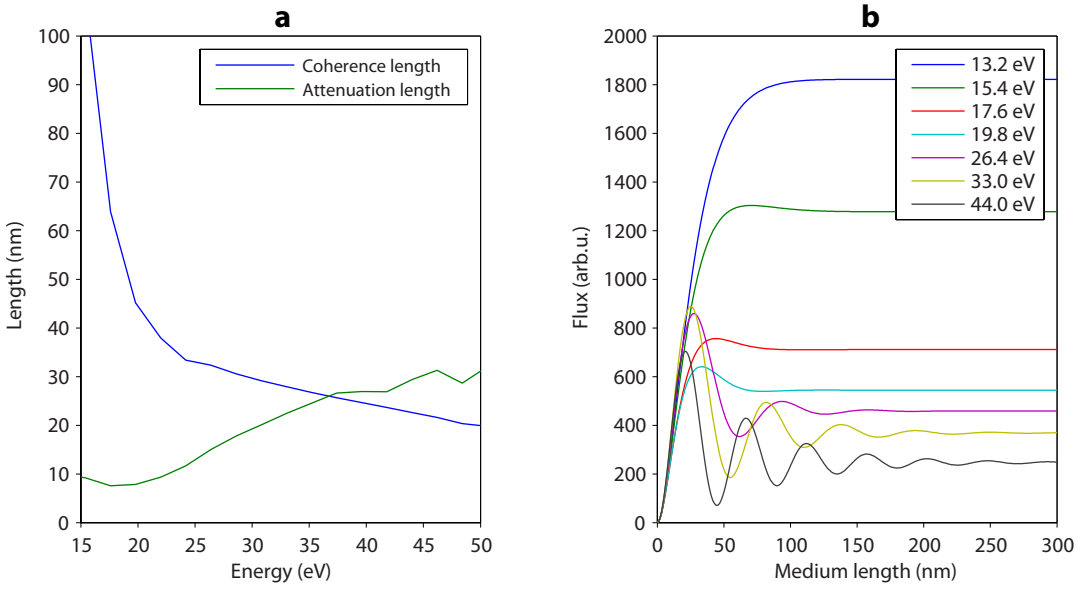

Figure 4.23: Phase matching considerations of EUV radiation in SiO_2 thin films. **a,** Coherence and absorption (attenuation) length as a function of photon energy. **b,** Build-up of EUV flux versus propagation length calculated for different photon energies (annotated in legend).

Fig. 4.23 shows an evaluated coherence length and attenuation length for the case of SiO_2 thin films and their corresponding flux build-up. Since this consideration depends strongly on the refractive indexes acquired for SiO_2, we utilized here the parameters from Palik [223] because it provides the parameters for our range of interest completely. Comparable results (within 10% accuracy) can be obtained using the parameters from Henke *et al.* [195]. However, the data from Henke *et al.* did not provide parameters for photon energies higher than 30 eV thus using data from Palik is a proper choice.

For the low energy photons, Fig. 4.23a demonstrates that the requirement Eq. 4.19b is satisfied easily and Eq. 4.19a means that our medium has to be > 90 nm in order to collect photons at ~ 40 eV effectively. However, the Eq. 4.19b is not satisfied well at high energies which indicates that we might not have high flux at this energy range. Indeed, the total flux calculation as a function of different photon energies and different propagation lengths in Fig. 4.23b shows that we can have most efficient flux build-up at ~ 100 nm for our range of interest. Therefore, a selection of SiO_2 film with a thickness of ~ 125 nm as we did in our experiments was reasonable and it also introduced the least effects of nonlinear and linear distortions of our driving fields while propagating through the medium.

For sample with thickness close to ~ 250 nm, the result of Fig. 4.23 suggest that the total radiated EUV flux will be similar to that of ~ 125 nm. However, the heat dissipation for the thicker sample will be better than the thinner ones but more importantly, the electric field waveforms can be changed significantly compared to the thinner cases. Because of this reason, we prefer to carry out experiments with the thinner samples first so that less parameters will be included in the studying of the physical picture.

4.4.2 Crystallinity of samples: determination of microcrystals size

We investigated our samples using an EUV synchrotron source. The EUV absorption in the $L_2, 3$ edge of SiO_2 has been measured with a spectral resolution < 0.1 eV, it is displayed on Fig. 4.24 (solid blue curve). The presence of the spin-orbit doublet in the core exciton at 106 eV has been reported to be a proof of crystallinity of SiO_2 (the doublet is smeared out in totally amorphous samples)[224, 225]. To be more quantitative, we applied the procedure described in Ref. [224] by deconvoluting the spin-orbit doublet (dashed red curve) and fitting with a Gaussian (solid green curve), the FWHM of which is 0.52 eV. According to Ref. [225], the result of this fitting demonstrates short-range order with a coherence radius above 20 Å meaning average size of > 40 Å.

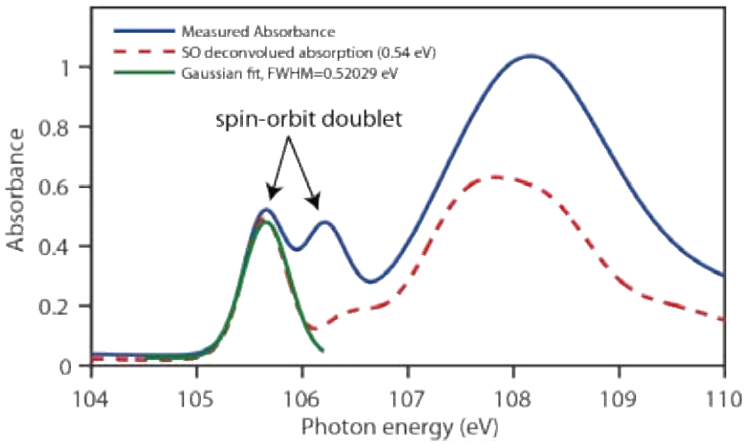

Figure 4.24: Estimation of short range order length from EUV absorbance. Measured EUV absorbance (solid blue curve), spin orbit deconvoluted absorbance (dashed red curve) and Gaussian fit of core-exciton spike (solid green curve). Adapted from [196].

4.4.3 Other consideration of theoretical models

The two models utilized in our discussion so far are based on real acceleration and scattering of the electron wave packet in the conduction band (with and without taking into account other electron dynamics) which plainly requires the involvement of the differentiation in **k**-space. If one wants to consider the effective mass (which is used to construct an analogy of the electrons in the bands in solids as free particles in real space), one could reduce the burden getting the solutions of a differential equation (or coupled differential equations) and find a simpler analytical solution instead which is similar to our results (Eq. 4.13)

In fact, it has been shown by Ghimire *et al.* in [42] and with more details in [46] that a nonlinear current density will be created:

$$\mathbf{J}(t) = \frac{Ne^2}{m^*\omega_0} \sum_{n,s=1}^{\infty} \frac{n^2 b_n}{2s-1} \left[\mathfrak{J}_{2s-2}\Big(n\frac{\omega_B}{\omega_0}\Big) + \mathfrak{J}_{2s}\Big(n\frac{\omega_B}{\omega_0}\Big) \right] E \sin\Big((2s-1)\omega_0 t\Big) \tag{4.20}$$

when a small electron density N is accelerated under influence of an electric field $E\cos(\omega_0 t)$. Here m^* is the effective mass of the band in consideration, $b_n = c_n d^2 m^{\cdot}/\hbar^2$ are the scaled Fourier coefficients corresponding to coefficients c_n making up the band structure using cosinusoidal assumption $\epsilon(\mathbf{k}) = \sum c_n \cos(nd\mathbf{k})$, d is the lattice constant. $\mathfrak{J}_i$ is the i^{th} order Bessel function of first kind. $\omega_B = eEd/\hbar$ is the Bloch frequency corresponding to the maximum electric field.

In addition, Golde, Meier, and Koch have shown nicely even before in [41] that a similar expression for the current density can be achieved:

$$\mathbf{J}(t) = -ed\omega_\Delta 2 \sum_{N=0}^{\infty} \mathfrak{J}_{2N+1}\Big(\frac{\omega_B}{\omega_0}\Big) \sin\Big((2N+1)\omega_0 t\Big) \cdot \sum_{k_0} n_{k_0}(t)\cos(k_0 d) \tag{4.21}$$

where the effective $\omega_\Delta = (\Delta_e + \Delta_h)/(2\hbar)$ and $n_{k_0}(t)$ is the time dependent population of the electrons in the conduction band.

The current density in Eq. 4.20 does assume there are some electrons already in the conduction band and the nonlinear current is generated through acceleration and scattering of the electron wave packet in the conduction band. In Eq. 4.21, they added the last term on the right hand side to take into account the interband excitations. Nevertheless, both of the equations visibly show that there is contribution of the odd high harmonic terms ($(2s-1)\omega_0$ in Eq. 4.20 or $(2N+1)\omega_0$ in Eq. 4.21) to the total current densities in temporal domain which broadens their associated spectra.

Chapter 5

Bound electron control in Krypton

5.1 Bound electron control in Krypton atoms

In this chapter, we show that intense (> 50 GW), field-tailored, optical attosecond pulses ($\sim$ 400 as, chapter 2) are capable of providing attosecond control in bound electrons. Broadband manipulation of vacuum ultraviolet (VUV) spectra that emanated from neutral Kr atoms, driven by waveform-controlled optical attosecond pulses, revealed attosecond dynamics of bound-electron dipoles, which are a close analogy to those of ionized atoms in strong fields [29, 63, 226]. Our experiments highlight capability of these tools for porting the basic paradigms of attosecond control from continuum-state (ionization) to bound-state (neutral) electrons. Electrons in Kr atoms exposed to ultrafast excitation by these pulses reveal, for the first time, the frontiers of nonlinear electronic response, manifested as an attosecond-scale non-instantaneity of the induced dipole, as captured in our measurements.

5.1.1 Two level model - adiabatic response

To demonstrate the power of optical attosecond pulses in advancing nonlinear control of bound-state electrons to attosecond scales, we performed simulations in which a bound electronic system was modelled as a two-level atom. In the quasi-static approximation for a low frequency electric field, the induced dipole moment in a two level model can be calculated by [227], Eq. (8):

$$d(t) = d\frac{2dF\sin(\omega t)}{\sqrt{4d^2F^2\sin^2(\omega t)+\omega_0^2}} \tag{5.1}$$

where the electric field is described by $F(t) = F\sin(\omega t)$, d is the transition dipole moment of the two levels (chosen to match the nonlinear properties of Kr), ω_0 is the energy difference between the two levels. The transient transition frequency can also be written analytically as:

$$\omega_0(t) = \sqrt{\omega_0^2 + 4d^2F^2\sin^2(\omega t)} \tag{5.2}$$

This is a Stark shift (shifting of energy levels under influence of electric field) and as the time dependent function suggests, the transient energy level depends rigorously on

the strength *and* the phase of the incident electric field. Even though this is a result obtained for a two level model, Eq. 5.2 in principle can serve as an intuitive picture representing the bound electrons response of Kr atoms under incident electric fields.

We exposed this model atom (Eq. 5.1) to three different electric fields applied in our experiments: (i) a single-cycle pulse (Fig. 5.1a); (ii) a considerably shorter, optical attosecond pulse (Fig. 5.1d); and (iii) a chirped but spectrally equivalent pulse (Fig. 5.1g). All three driving fields were synthesized and used in the experiments described below. Importantly, the peak intensity was restricted at levels ($\sim 4 \cdot 10^{13}$ W/cm^2) for which simulations based on solution of the 3D-TDSE for Kr predict $< 0.2\%$ ionization (Table 5.1), i.e., the electrons remain virtually bound.

Peak intensity $*10^{13}$ W/cm^2	1	2	4	6	8	10
Ionization probability (%)	0.0018	0.06	0.18	0.84	1.38	2.4

Table 5.1: Ionization probability calculated for different pulse intensities using the 3D-TDSE [74]

Following an investigation method based on previous studies in the strong-field regime of control [29, 32], we plot the nonlinear electron dipoles induced by these case-study driving fields as a function of their global phase (Fig. 5.1) along with a significant fraction of their corresponding dipole spectra in the range of $5 - 15$ eV. For illustration purposes, the energies of the electronic resonances of Kr are also indicated (dashed grey lines).

Close inspection of the induced nonlinear dipoles and their respective spectra shown in Fig. 5.1a,b reveals that single-cycle pulses - which have been demonstrated to attain attosecond control under a strong field, as, for instance, manifested by the multi-eV broad, CEP-sensitive emission of EUV radiation [29, 30, 226] - are here unable to significantly modify the emitted spectra by variation of their global phases. This result implies that in the time domain, other than a shift of its absolute phase, the induced few-femtosecond dipole remains virtually unchanged (Fig. 5.1a) under this variation. In contrast, compression of the driver field to a half-cycle (Fig. 5.1d,e,f) not only allows confinement of the nonlinear dipole to a fraction of the oscillating field but also enables its dynamic control with global phase (double- vs. single-polarization bursts) within its *de facto* sub-femtosecond time interval of action. As a result, the polarization, and consequently the emitted spectra, suffers a broadband (several eV) modulation with φ_G (Fig. 5.1f), which, in close analogy with that of ionized electrons in strong field experiments, highlights attosecond control of the nonlinear dipole. When the chirped but spectrally equivalent pulse in Fig. 5.1g is used to drive the system, spectral control is retained, but it becomes asynchronous: various parts of the emitted spectrum follow a different modulation phase with respect to φ_G (Fig. 5.1i), thereby revealing fragmentation of the nonlinear dipole into several half-cycles (Fig. 5.1g) instead of the single or double burst displayed in Fig. 5.1d. The above simulations illustrate that porting concepts of attosecond control to bound electrons calls for compression of optical fields to time scales that are nearly an order of magnitude shorter than those typically required for attosecond control based on ionization.

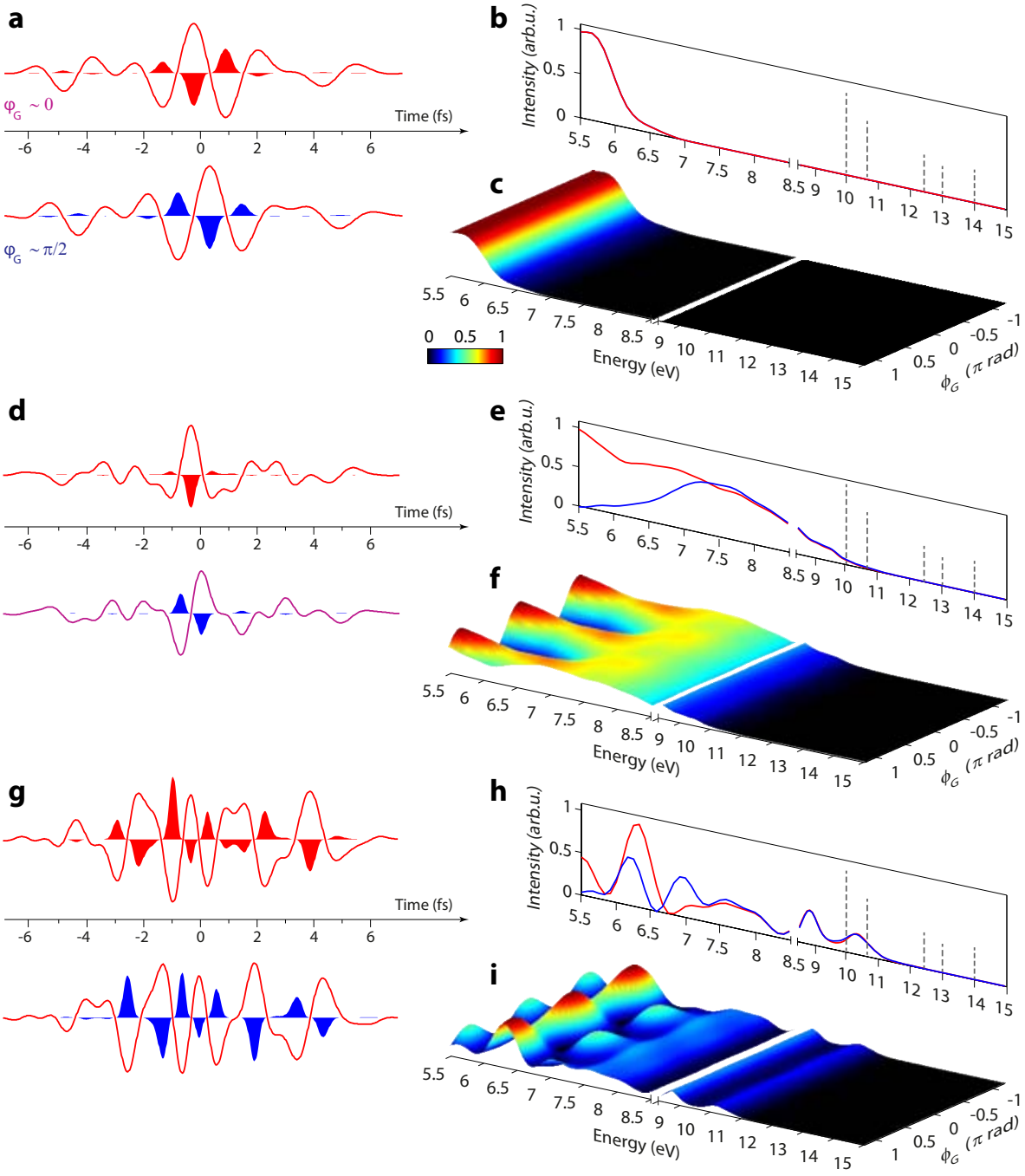

Figure 5.1: Field induced nonlinear control of bound electrons. **a,** Time dependent electric fields (solid red lines) and their respective dipole moments (rescaled, filled areas) of a single cycle pulse, **d,** of an optical attosecond pulse and **g,** a chirped optical attosecond pulse at two global phase settings ($\varphi = 0$ (red areas) and $\varphi = \pi/2$ rad (blue areas). **b,e,h,** Corresponding spectra in the range 5.5 $\rightarrow$ 15 eV ($\varphi = 0$ (red lines) and $\varphi = \pi/2$ rad (blue lines). Dashed gray lines indicate resonant emissions of Kr. **c,f,i,** Emitted spectra as a function of the global phase.

5.1.2 Experimental setup

To experimentally explore the above control possibilities, we used the same setup as shown in Fig. 2.7, where now the streaking gas target can be replaced by a quasi-static gas cell which is filled with Krypton (Kr) at $\sim$ 80 mbar, Fig. 5.2a. The nanometric precision 3-axis stage allows one to accurately move both the targets at the same place which ensures that the Kr gas target will be exposed with the same electric field recorded by attosecond streaking. The emitted VUV spectrum is line-focused on the slit of the VUV spectrometer. The spectrometer is set to measure spectra ranging from 5 to 14 eV which constitute the energy range from the end of the fundamental pulses to the first ionization potential of Kr ($I_p \sim 14$ eV), respectively. The sampled spectra are illustrated in Fig. 5.2b.

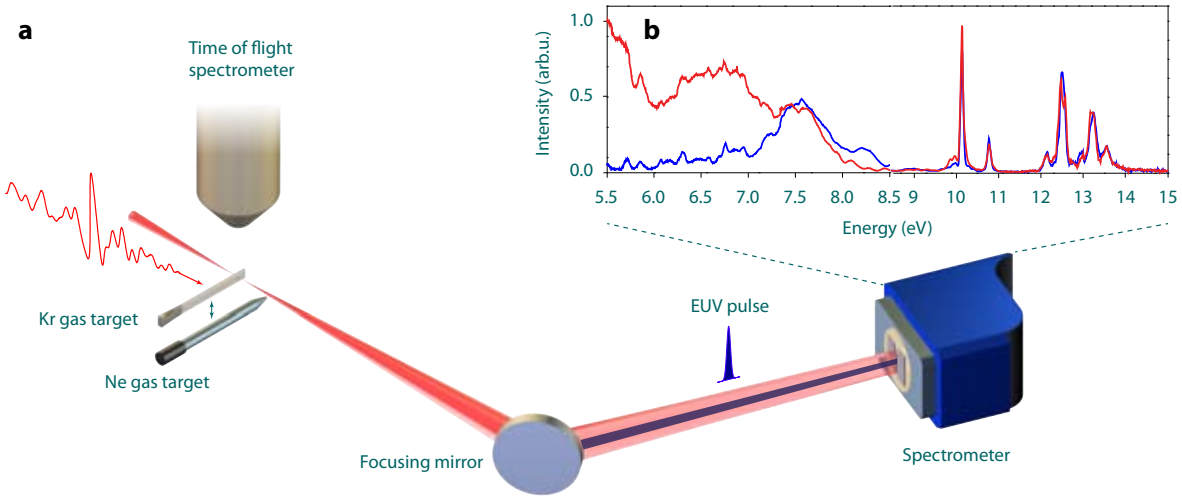

Figure 5.2: Experimental setup for bound electron control in Krypton. **a** The optical attosecond pulses are focused on the Kr gas target. Emitted spectra are recorded on a spectrometer placed after a focusing mirror. **b,** Spectra recorded at identical experimental conditions except the global phase is changed from $\varphi = 0$ (solid red line) to $\varphi = \pi/2$ rad (solid blue line). Different normalizations are used for two different spectral ranges, $5.5 - 8.5$ eV and $8.6 - 15$ eV.

Since the emitted spectra extend to a very large frequency range, calibration of both the energy axis as well as the spectral intensity axis becomes important. To this end, we employed a calibrated Deuterium lamp (McPherson) that supports $115 \rightarrow 380$ nm (or $3.3 \rightarrow 10.8$ eV) and use this as a calibration source for our spectrometer. By using polynomial fitting, we could calibrate our spectra up to photon energies of 10.8 eV, the higher photon energies were calibrated by using atomic spectral data from National Institute of Standards and Technology. Because of the presence of 1200 grooves/mm grating, the spectra were recorded at two different grating positions. All fragmented spectra are patched to give the final spectrum.

We performed systematic measurements of the emitted spectra from Kr atoms by utilizing different electric fields, each of them at different global phase settings and different intensities. The result of these measurements is discussed in the next section.

5.1.3 Attosecond control of bound electrons

The captured spectra were quasi-continua over several electron volts (5.5 to 10 eV) (Fig. 5.3a), whereas in the range 10-14 eV, they exhibited discrete peaks that coincided well with the electronic transitions of atomic Kr. These spectra demonstrate the capability of optical attosecond pulses to nonlinearly excite virtually any quantum level in the range $1 - 14$ eV, including the complete bound electronic state manifold of Kr, and already suggest their potential for attosecond control.

Variation of the global phase (Fig. 5.3a) of these pulses yielded a pronounced broadband modulation of the VUV emission both below ($5.5 - 10$ eV) and within the range of electronic resonances ($10 - 14$ eV), thereby verifying the key features of the control schemes discussed in Fig. 5.1.

A spectrally equivalent but longer optical waveform in Fig. 5.3d precisely reproduced the predictions of Fig. 5.1i, i.e., it yielded asynchronous amplitude modulation of different parts of the emitted spectrum, thereby revealing the fragmentation of the dipole to several rather than 1-2 half-field cycles.

In close analogy, a pulse synthesized by our apparatus to entail approximately a single optical cycle by physically suppressing a part (> 3 eV) of the high-frequency spectrum of the optical attosecond pulse (Fig. 5.3f bottom right) with a comparable peak (non-ionizing) intensity failed to generate broadband nonlinear excitation or its control through variation of the global phase (Fig. 5.3f); this result agrees well with the predictions of our modelling, which are shown in Fig. 5.1c. These results highlight that in the absence of the extreme nonlinearities of ionizing fields, optical attosecond pulses are the key to manipulation of bound electrons on the natural sub-femtosecond time scale of their motion.

5.2 Theoretical description

5.2.1 Proof-of-concept simulations

To shed light into capabilities of optical attosecond pulses in controlling bound electrons and possibly explaining experimental data, we performed theoretical simulations of light matter interaction invoking 3D-TDSE [74] for Kr and an instantaneous model in which polarization response of a system under interaction with electric field is: $P(t) \propto A \cdot E(t)^3 + B \cdot E(t)^5$. The results of the simulations are shown in Fig. 5.4.

While the temporal profile of the calculated polarization responses (Fig. 5.4a) provides limited insight except absolute time difference of the responses, a time-frequency analysis (more details in chapter 6) as in Fig. 5.4b (left panel) can offer much more intuition. This technique is based on Gabor transformation or short time windowing and has been used by Yakovlev *et al.* [228]) or Muecke [45] to represent moments of generation of different harmonics in the HHG. In short, it is a trace composed of spectra at different time delays whose formula is written by:

$$S(\omega, \tau) = \left| \mathfrak{F}\big[E(t) \cdot G(t - \tau)\big] \right|^2 \tag{5.3}$$

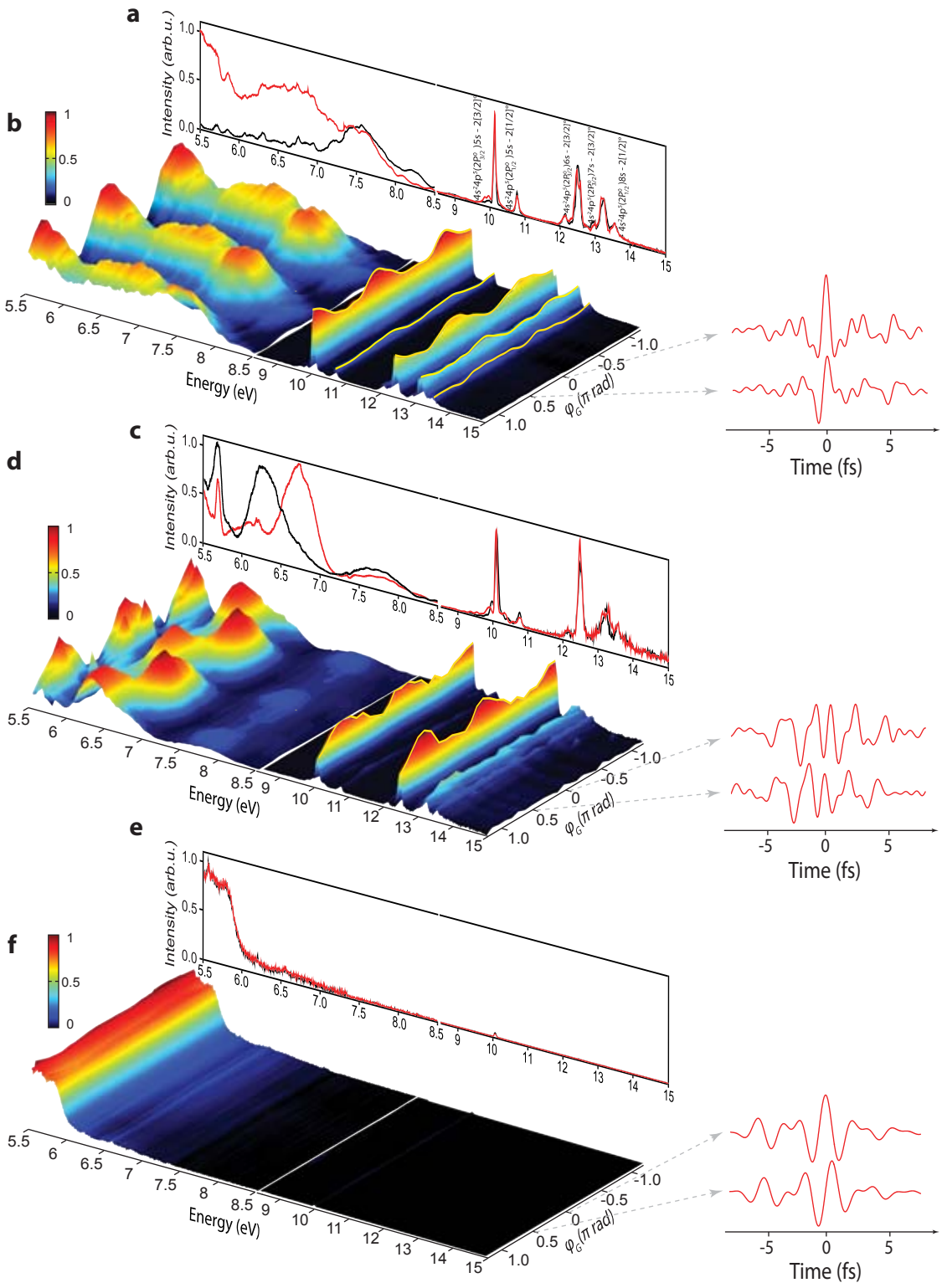

Figure 5.3: Attosecond control of bound electrons in Kr. a, VUV spectra generated in neutral krypton driven by an optical attosecond pulse, **c,** a spectrally equivalent but chirped waveform generated by a phase shift of the UV band by $\pi/2$ rad, and **e,** a single-cycle pulse. **b, d,** and **f,** Spectrograms composed of 22 VUV spectra ($5.5 - 15$ eV) recorded as a function of φ_G for the above waveforms. The spectrograms represent the average of four data sets recorded under identical conditions. Representative field waveforms for $\varphi_G = 0$ and $\varphi_G = \pi/2$ rad are displayed on the bottom right of each spectrogram. Adapted from [139].

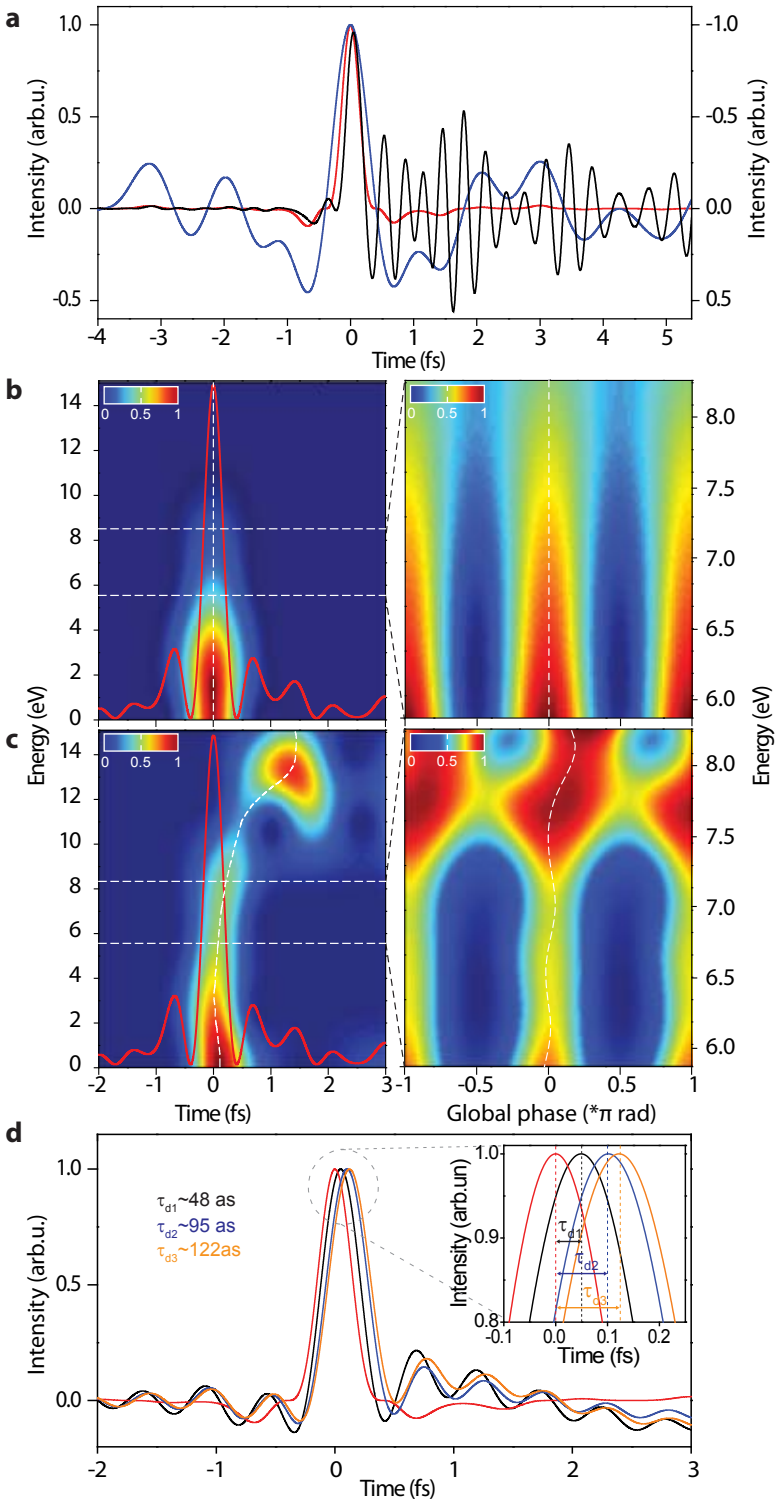

Figure 5.4: Delayed nonlinear response of bound electrons in Kr - Simulations. a, Electric field (blue line), polarization response calculated from 3D-TDSE simulation (black line), and adiabatic model (red line). **b,** Time-frequency analysis of the polarization calculated from adiabatic model (left panel) and global phase spectrogram of the same model (right panel). **c,** Same as **b** but for the polarization calculated from 3D-TDSE simulation. Instantaneous intensity of the electric fields (red lines) is plotted on top to show time reference. **d,** Filtered $(0-8\,\mathrm{eV})$ polarization responses calculated from 3D-TDSE for three intensities: $4\cdot10^{13}$, $6\cdot10^{13}$, and $8\cdot10^{13}$ W/cm^2 (black, blue, and yellow lines). Inset in d shows delays between adiabatic polarization response and 3D-TDSE polarization responses. Adapted from [139].

where $E(t)$ is the induced current, the gate function $G(t)$ is any filter function (a Gaussian is generally used).

Under the instantaneous model, synchronized emission of all frequencies can be observed for the entire range of the spectrum. Furthermore, there is a precise time synchronization between the generated emission and the incident electric field. However, time-frequency analysis of the calculated polarization response from the 3D-TDSE Fig. 5.4c (left panel) shows evidently asynchronous moments of emission of different spectral components. Clear retardation of more than 1 fs can be seen for emission in resonant range of Kr ($10 - 14$ eV).

Similar differences between the instantaneous model and 3D-TDSE simulation can be observed in the global phase spectrograms (Fig. 5.4b and c, right panels). Even though results in global phase spectrograms may not be interpreted as directly as in time-frequency analysis, asynchronous modulation of the global phase at maximum spectral intensities (white dashed line) in c (compared to straight line in b) still suggests time-related features of the nonlinear polarization responses from 3D-TDSE compared to instantaneous model.

In order to compare directly the polarization responses in time domain, we filtered out the high energy components (> 9 eV) and plotted the resultant nonlinear, non-resonant responses calculated from all the models as in Fig. 5.4d. Evidently, the nonlinear responses from 3D-TDSE are delayed with respect to their instantaneous counterpart. Furthermore, the delay increases as the intensity of incident electric field increases.

5.2.2 Benchmarking the simple model

Above consideration illustrates how the polarization responses from the 3D-TDSE differ from the instantaneous model. Although 3D-TDSE simulation can give a great deal of information as well as resemble reality, extracting physical processes out from it or fitting an experimental data can hardly be done. Therefore, by introducing a simple model as follows

$$P(t) \propto A \cdot E(t)^3 + B \cdot E(t)^5 + C \cdot E(t - dt)^5 \tag{5.4}$$

we attempt to reconstruct experimental data.

However, benchmarking this simple model by 3D-TDSE simulations is required before sustainable conclusions can be drawn from it.

Fig. 5.5a shows the spectrogram obtained from the 3D-TDSE simulation for optical attosecond pulses at the intensity of $\sim 4 \cdot 10^{13}$ W/cm^2 and the fitted spectrogram using the simple model is illustrated in Fig. 5.5b. It is evident that the fitted spectrogram reproduces most of the features of the simulated spectrogram: broadband and intense spectra at $\varphi = 0$, minimal and rising spectra (higher amplitude at higher photon energies) at $\varphi = \pi/2$ rad, asynchronous amplitude modulation as a function of the global phase, and furthermore, the relative spectral amplitude is also well captured. This reproducibility is additionally verified by comparison of the nonlinear polarization response from the 3D-TDSE and the response extracted from the fitting for the case of $\varphi = 0$ (Fig. 5.5c) and $\varphi = \pi/2$ rad (Fig. 5.5d).

As a result, the great agreement between the simulated and fitted spectrograms demonstrates a possibility that the experimental spectrograms 5.3 can be also analyzed

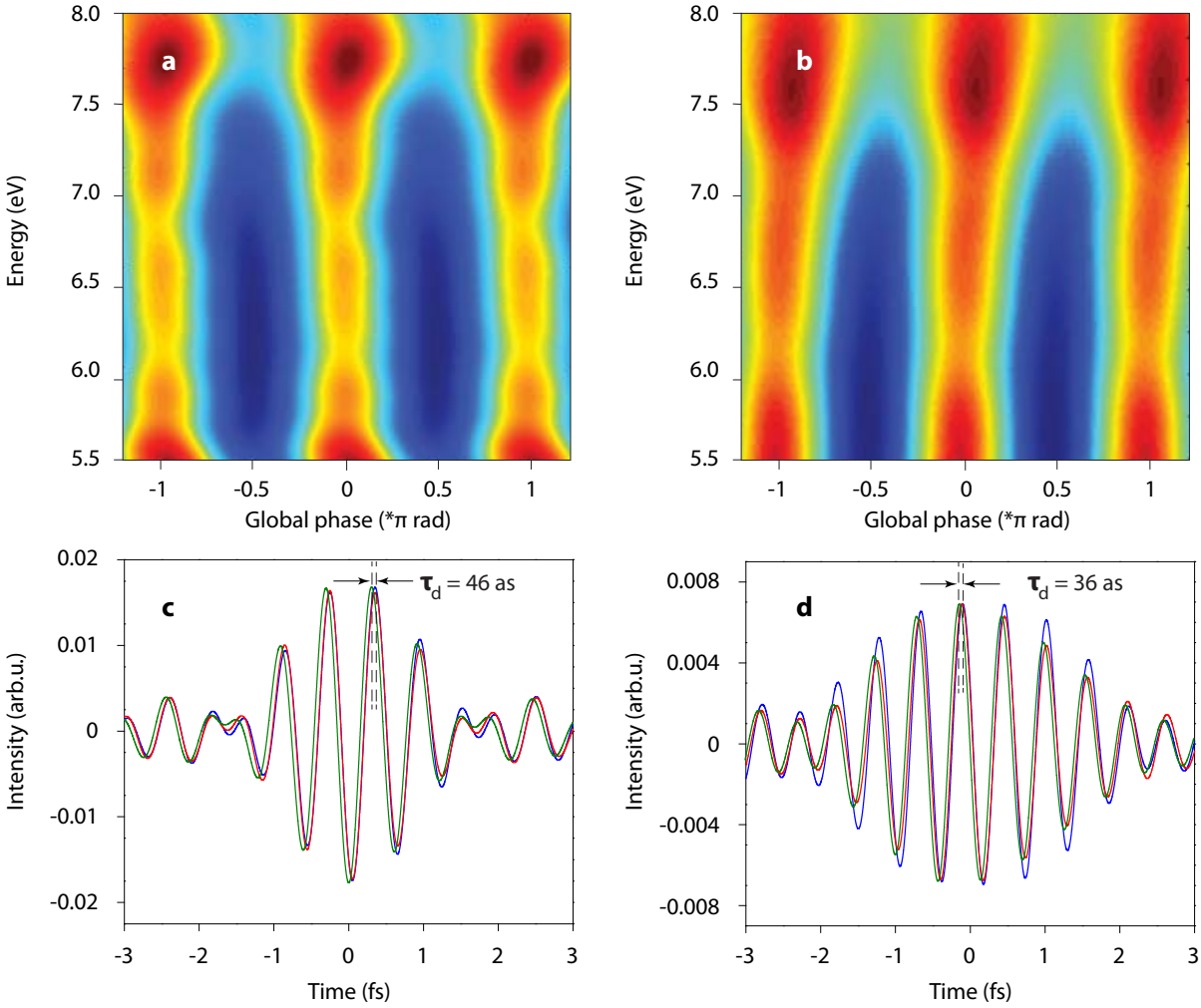

Figure 5.5: Reconstruction of the 3D-TDSE simulation of the polarization response of Kr atom. **a,** Series of nonlinear spectra ($5.5 - 8$ eV) calculated as a function of the global phase φ of the experimental optical attosecond pulse (Intensity $\sim 4 \cdot 10^{13}$ W/cm^2). **b,** Reconstructed spectrograms utilizing the simple model. The calculated polarizations through TDSE of the attosecond light transient for $\varphi = 0$ (**c**) and $\varphi = \pi/2$ rad (**d**) are band-pass-filtered ($5.5 - 8$ eV) and shown in blue lines together with the reconstructed polarizations (red curves), and the instantaneous polarizations (green curves). Adapted from [139].

to a great extent by the simple model.

5.2.3 Probing attosecond nonlinear delayed responses

Having confirmed the validity of the simple model to reconstruct the polarization response calculated from the 3D-TDSE model, we attempt reconstruction of the experimental data utilizing this model. The results are shown in Fig. 5.6.

Over the whole intensity range of our experiments, good agreement can be observed between the experimental spectrograms and the reconstructed ones. Main spectral modulations at global phase values ($-1, 0, 1 \cdot \pi$ rad) are precisely captured for all intensities. Furthermore, asynchronous modulation of the spectra as a function of the global phase

from $5 - 7$ eV are also reconstructed. Additionally, the small kink at the energy range ~ 7.5 eV is reproduced and more importantly the relative change in spectral amplitude (stronger at higher energies for high intensities) can be reliably reproduced for three intensities.

Above agreements between the experimental data and the reconstructed ones show the simple model as a reliable model to capture the experimental results. As a result, Fig. 5.6c shows filtered polarization responses of the instantaneous model and of the simple model utilizing reconstructed coefficients. Different electric field intensities result in different reconstructed delays with respect to the instantaneous polarization. Moreover, the reconstructed delays are in great agreement with the delays previously obtained from 3D-TDSE simulations (Fig. 5.4).

To conclude, the analysis presented here offers the first insights into attosecond nonlinear delayed response of bound electrons in Kr. We believe that extension of the current models with more sophisticated theories may soon enable further understanding into dynamics of electrons in bound systems, opening up new possibilities in attosecond physics and related technologies.

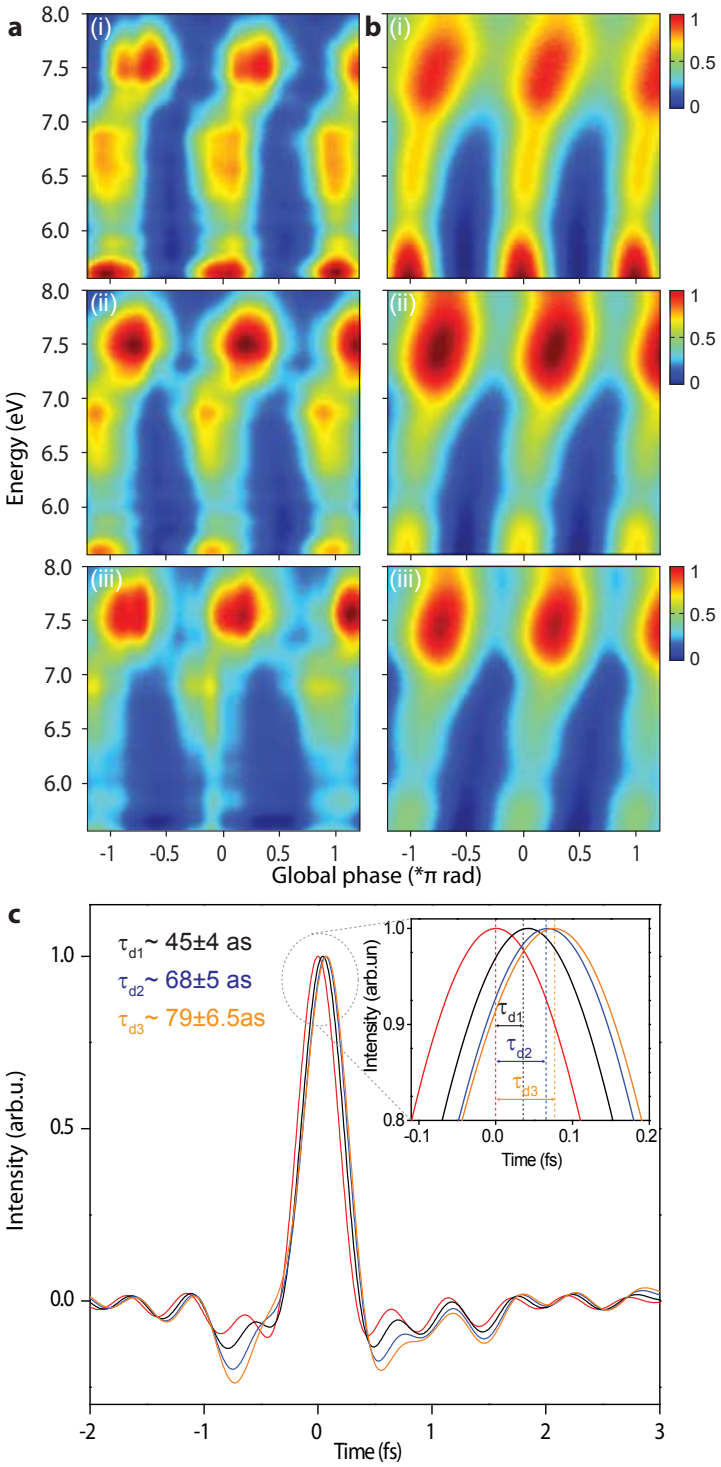

Figure 5.6: Delayed nonlinear response of bound electrons in Kr - Experiments. **a,** A portion (5.5-8 eV) of the measured global phase spectrogram at three different peak intensities (i, ii, iii). **b,** Corresponding reconstructed spectrograms by the simple model. c, Retrieved polarization responses at three intensities: $4 \cdot 10^{13}$, $6 \cdot 10^{13}$, and $8 \cdot 10^{13}$ W/cm^2 (black, blue, and yellow lines) in contrast with the adiabatic dipole in red line. The inset in **c** shows the delay between the adiabatic polarization response and the retrieved polarization responses. Adapted from [139].

Chapter 6

Conclusions

6.1 EUV high harmonic generation and spectroscopy in solids

I have shown that efforts in this thesis have lead to demonstration of coherent EUV generation from solids with photon energies extending up to 40 eV by exposing the samples to strong and ultrashort incident electric fields. The emitted radiation exhibit harmonic structure where all the peaks are associated with the odd harmonics of the fundamental incident electric field frequencies except for the case of single-cycle pulses and optical attosecond pulses. Knowledge from the comprehensive intensity scaling of the measured spectra as a function of the electric field strength gave us solid foundation for investigation of the underlying physics. The linear dependence of the cut off energy on electric field strength, the nonperturbative behavior of the spectral intensity scaling as a function of field strength at different harmonic orders validated the semiclassical picture representing the Bloch oscillations together with acceleration (deceleration) of the electron wavepacket under incident field as the main cause of the EUV radiation. Bragg scattering of the electrons from the high order spatial harmonics of the conduction band gave rise to the emitted EUV. Decomposition of the conduction band into its Fourier series and fitting the intensity scaling using semiclassical model supported the first direct measurement of the conduction band dispersion profile, making the very first step in EUV spectroscopy in solids. The resolution obtained using our technique already approaches that of the modern angular resolved photoemission spectroscopy (ARPES) [220].

Weak global phase dependence of the emitted spectra was observed for few cycle pulses, the dependence slightly increased as the pulses get shorter and ultimately half cycle pulses (optical attosecond pulses) change drastically the spectra from super continuum to harmonic like spectrum. This does not only show the capability of manipulating the emitted EUV but also offered means to understanding the physical mechanisms involved. The radiation emerged by driving the coherent nonlinear motion of electrons in bulk solids represents an extension of solid-state laser photonics and electronics to a new regime of great potential for scientific and technological inquiries. Attosecond control of electronic motion revealed by the emitted radiation opens up opportunities for both steering and tracing strong field processes in solids as they occur in real-time as well as the sub-femtosecond engineering of their transient dynamics.

6.2 Bound electron control and attosecond nonlinear delayed response

As the first application of optical attosecond pulses our experiments on Kr have shown for the first time, to the best of our knowledge, complete, broadband bound electron control as represented by its associated VUV emission. Further analysis of the spectrograms together with comparison to numerical solution of a 3D-TDSE in the non-resonant part of the emitted VUV spectra suggests first insights of delayed response as an intrinsic property of a multi-electron system being driven by optical attosecond pulses.

6.3 TW scale field synthesizer

I have illustrated the design of the TW field synthesizer, a new generation of synthesizer which aims at synthesizing much more sophisticated, more powerful optical attosecond pulses than the current tools [58]. The encouraging results hold promise for the future applicability of the device.

Appendix A

Simulations and additional experimental data

A.1 Nonlinear coupled wave equations for second order nonlinear interactions

We are going to follow conventional derivations to end up with the first order propagation equation, then the polarization terms will be put into effects (SHG) such as in [188].

From the Maxwell's equations in the form of differential equations, if we consider a case at which there are no free currents ($\mathbf{J} = 0$), no free charges ($\rho = 0$), we can write down the coupled Maxwell's equations into:

$$\nabla \times \nabla \times \mathbf{E} + \frac{1}{c^2}\frac{\partial^2}{\partial t^2}\mathbf{E} = -\frac{1}{\epsilon_0 c^2}\frac{\partial^2}{\partial t^2}\mathbf{P} \tag{A.1}$$

Where we already identify $c = {}^1/_{\sqrt{\mu_0 \epsilon_0}}$. And $\mathbf{P} = \mathbf{P}(\mathbf{r}, t)$ is the total polarization response of the system. Then we make use of the curl's identities:

$$\nabla \times \nabla \times \mathbf{E} = \nabla(\nabla \cdot \mathbf{E}) - \nabla^2 \mathbf{E} \tag{A.2}$$

If $\mathbf{E}$ is a transverse plane wave, the first term of the right hand side vanishes. In general, if we assume the first term to be negligible then we come toward the wave equation in time domain:

$$\nabla^2 \mathbf{E} - \frac{1}{c^2}\frac{\partial^2}{\partial t^2}\mathbf{E} = \frac{1}{\epsilon_0 c^2}\frac{\partial^2}{\partial t^2}\mathbf{P} \tag{A.3}$$

However solving this equation in time domain is a costly computational task. We can transform it to frequency domain using the Fourier identity for differentiation:

$$\frac{\partial}{\partial t}\mathbf{E}(t) = \mathfrak{F}^{-1}\Big[i\omega \mathfrak{F}\big(\mathbf{E}(t)\big)\Big] = \mathfrak{F}^{-1}\Big[i\omega \mathbf{E}(\omega)\Big] \tag{A.4}$$

Here $\mathfrak{F}$ and $\mathfrak{F}^{-1}$ are the *Fourier transform* and *inverse Fourier transform* respectively. Clearly by applying Fourier transform on both sides of the equation A.3 and using identity

A.4, we have:

$$\nabla^2\mathfrak{F}\Big[\mathbf{E}(\mathbf{r},t)\Big] - \frac{1}{c^2}\mathfrak{F}\Big[\frac{\partial^2}{\partial t^2}\mathbf{E}(\mathbf{r},t)\Big] = \frac{1}{\epsilon_0 c^2}\mathfrak{F}\Big[\frac{\partial^2}{\partial t^2}\mathbf{P}(\mathbf{r},t)\Big] \tag{A.5a}$$

$$\nabla^2\mathbf{E}(\mathbf{r},\omega) - \frac{1}{c^2}\mathfrak{F}\Big[\mathfrak{F}^{-1}\Big[i\omega\mathfrak{F}\Big[\mathfrak{F}^{-1}\Big[i\omega\mathfrak{F}\big[\mathbf{E}(\mathbf{r},t)\big]\Big]\Big]\Big]\Big] = \frac{1}{\epsilon_0 c^2}\mathfrak{F}\Big[\mathfrak{F}^{-1}\Big[i\omega\mathfrak{F}\Big[\mathfrak{F}^{-1}\Big[i\omega\mathfrak{F}\big[\mathbf{P}(\mathbf{r},t)\big]\Big]\Big]\Big]\Big] \tag{A.5b}$$

$$\nabla^2\mathbf{E}(\mathbf{r},\omega) + \frac{\omega^2}{c^2}\mathbf{E}(\mathbf{r},\omega) = -\frac{\omega^2}{\epsilon_0 c^2}\mathbf{P}(\mathbf{r},\omega) \tag{A.5c}$$

Equation A.5c is the wave equation in the frequency domain. However at this stage, we should note that $\mathbf{P} = \mathbf{P}^{\mathbf{total}} = \mathbf{P}^{\mathbf{Linear+Nonlinear}}$. If we write down $\mathbf{P}^{\mathbf{Linear}}(\omega) = \epsilon_0\chi^{(1)}(\omega)\mathbf{E}(\omega)$ and $\epsilon^{(1)}(\omega) = 1 + \chi^{(1)}, \epsilon^{(1)}(\omega)\omega^2/c^2 = k^2(\omega)$, the wave equation becomes:

$$\big(\nabla^2 + k^2(\omega)\big)\mathbf{E}(\mathbf{r},\omega) = -\frac{\omega^2}{\epsilon_0 c^2}\mathbf{P}^{\mathbf{NL}}(\mathbf{r},\omega) \tag{A.6}$$

By assuming [182, 183]:

$$\mathbf{E}(\mathbf{r},\omega) = \mathbf{U}(\mathbf{r},\omega)\cdot e^{ik(\omega)z} \tag{A.7}$$

where $\mathbf{U}(\mathbf{r},\omega)$ is an envelope function. After some expansion and utilizing (*slowly varying envelope approximation*):

$$\Big|\frac{\partial^2}{\partial z^2}\mathbf{U}(\mathbf{r},\omega)\Big| \ll 2k(\omega)\Big|\frac{\partial}{\partial z}\mathbf{U}(\mathbf{r},\omega)\Big| \tag{A.8}$$

and decomposing $\nabla^2 = \partial^2/\partial_z^2 + \nabla_\perp^2$, we get the *first order propagation equation in frequency domain*

$$\Big(\frac{\partial}{\partial z} - ik(\omega)\Big)\mathbf{E}(\mathbf{r},\omega) = \frac{i}{2k(\omega)}\nabla_\perp^2\mathbf{E}(\mathbf{r},\omega) + \frac{i\omega}{2\epsilon_0 n(\omega)c}\mathbf{P}^{\mathbf{NL}}(\mathbf{r},\omega) \tag{A.9}$$

In this equation, $ik(\omega)$ is the term responsible for the absorption, gain or dispersion of the wave in the medium. The first term on the right hand side is the diffraction term (with second derivative $\nabla_\perp^2$ on x, y), the second term on the right hand side is the nonlinear polarization expressed in frequency domain which is responsible for all the nonlinear effects happening in the medium. This equation in general provides huge advantage in solving numerical problems as compared to the full wave equation A.3. Nevertheless, from the derivation of the approximation, this first order propagation equation cannot be applied if there is backward propagating wave [184], the complex amplitude changes rapidly or the beam is focused, etc.

Now we want to consider the case of BBO type I *ooe* phase matching (i.e. the two input waves are in ordinary axis and the output second harmonic wave is in extraordinary axis). It is instructive to break down the first order propagation equation A.9 into two coupled

equations with x representing the *ordinary* axis and y representing *extraordinary* axis (neglecting the diffraction term):

$$\frac{\partial}{\partial z}\mathbf{E}_x(\omega) = ik_x(\omega)\mathbf{E}_x(\omega) + \frac{i\omega}{2\epsilon_0 n_x(\omega)c}\mathbf{P^{NL}}_x(\omega) \tag{A.10a}$$

$$\frac{\partial}{\partial z}\mathbf{E}_y(\omega) = ik_y(\omega)\mathbf{E}_y(\omega) + \frac{i\omega}{2\epsilon_0 n_y(\omega)c}\mathbf{P^{NL}}_y(\omega) \tag{A.10b}$$

Midwinter and Warner [229] described detailed progress in order to calculate the effective value for the susceptibility tensor for the polarization response. We can write down the result for the case of θ, ψ as input parameters, $d_{eff} = d_{31} \cdot \sin(\theta) - d_{22} \cdot \sin(3\psi) \cdot \cos(\theta)$ whereas $d_{22} = 2.2 \cdot 10^{-12} m/V$ taken from [75] and $d_{31} = 0.16 \cdot 10^{-12} m/V$ taken from [189]. If we take into account the degeneracy of all possible processes in second harmonic generation, we will have:

$$\mathbf{P^{NL}}_x(\omega) = 4\epsilon_0 d_{\text{eff}} \cdot \mathfrak{F}\Big[\mathfrak{F}^{-1}\big[\mathbf{E}_x(\omega)\big] \cdot \mathfrak{F}^{-1}\big[\mathbf{E}_y(\omega)\big]\Big] \tag{A.11a}$$

$$\mathbf{P^{NL}}_y(\omega) = 2\epsilon_0 d_{\text{eff}} \cdot \mathfrak{F}\left[\Big(\mathfrak{F}^{-1}\big[\mathbf{E}_x(\omega)\big]\Big)^2\right] \tag{A.11b}$$

As a result, we can write equation A.10 as:

$$\frac{\partial}{\partial z}\mathbf{E}_x(\omega) = ik_x(\omega)\mathbf{E}_x(\omega) + \frac{i2d_{\text{eff}}\omega}{n_x(\omega)c} \cdot \mathfrak{F}\Big[\mathfrak{F}^{-1}\big[\mathbf{E}_x(\omega)\big] \cdot \mathfrak{F}^{-1}\big[\mathbf{E}_y(\omega)\big]\Big] \tag{A.12a}$$

$$\frac{\partial}{\partial z}\mathbf{E}_y(\omega) = ik_y(\omega)\mathbf{E}_y(\omega) + \frac{id_{\text{eff}}\omega}{n_y(\omega)c} \cdot \mathfrak{F}\left[\Big(\mathfrak{F}^{-1}\big[\mathbf{E}_x(\omega)\big]\Big)^2\right] \tag{A.12b}$$

Eq. A.12 is the main coupled equations to be solved numerically for our given electric fields. It is almost identical to Eq. 22 in [188] except that their equation is more general for the different types of interaction (other than type I phase matching). Even though one can generalize these as in [230], we found out that a simple 1D propagation based on Eq. A.12 is sufficient to interpret our experimental data and provide valuable insights.

Additional notes

Usually one more step is done additionally to the Eq. A.12 that is to move the frame of reference to the moving frame (together with the carrier wave of the incident pulse, for example) [184, 186] with $\tau = t - \beta_1 \cdot z$ where β_1 is the first order dispersion term of the medium. We can apply this to Eq. A.12 by replacing the terms $k_{x,y}(\omega)$ and $n_{x,y}(\omega)$ by $k_{x,y}(\omega) - k_{x,y}(\omega_c)$ and $n_{x,y}(\omega) - n_{x,y}(\omega_c)$ where X_c denotes the values at the carrier wave. This moving frame suppresses the possibility of the electric field reaching the limited grid boundaries.

One should also take good care for the calculation of the refractive indexes. The values used in this consideration are taken from [231] then proper calculation of the *ordinary*

and *extraordinary* refractive indexes at θ angle is done based on Eq. 2.3.8 of [75]. This ensures the phase matching of the fundamental (o) and SH (e) pulses during propagation.

Similarly, this equation can be numerically integrated by standard time integrators. However, a careful inspection at the form of the formula suggests high applicability of the exponential Euler method: the first terms in the RHS of Eq. A.12 are the linear terms, the second terms are the nonlinear terms in the exponential Euler formula. As a result, integrating this equation using the exponential Euler method gains more than one order of magnitude in terms of speed with acceptable accuracy compared to the RK4, making the exponential Euler formula the most suitable method in this case.

It has been proven (Appendix A, [188]) that Eq. A.12 above as well as Eq. 22 in [188] nicely preserve the total energy of the electric fields during propagation inside the medium. Therefore this is a very good check for the numerical convergence (and/or accuracy) of the simulation. All the simulation results shown in chapter 3 satisfy the energy conservation tolerance of less than 1%.

A.2 One dimensional TDSE

A.2.1 Setting up the Hamiltonian

We are going to outline detailed procedure for a numerical solution of the one dimensional TDSE. The full TDSE 1.2 can be cast in the 1D form:

$$i\hbar\frac{\partial\Psi(x,t)}{\partial t} = \mathbf{H}\Psi(x,t) \tag{A.13}$$

where the Hamiltonian $\mathbf{H}$ can be written as:

$$\mathbf{H} = \mathbf{T} + \mathbf{V} = \frac{-\hbar^2}{2m}\frac{\partial^2}{\partial x^2} + V(x) \tag{A.14}$$

Here we should note that $\mathbf{V} = V(x) - x \cdot E(t) = V(x,t)$ under the influence of the incident electric field.

A.2.2 Choosing the potential

Since the form of the Coulombic potential is problematic at $x = 0$ hence for the 1DTDSE, a modified model potential (with deviation from the real Coulombic potential) is widely used. This is often called the *soft core potential* [80] and is written as:

$$V(x) = \frac{-q}{\sqrt{x^2 + a^2}} \tag{A.15}$$

where q and a^2 are chosen values such that the model potential provides similar ionization potential (or excited state energies) as the real atomic system of interest. If one chooses $(q; a^2) = (1; 2)$ then we get the $I_p = 13.6$ eV which is the real ionization potential of Hydrogen. $(q; a^2) = (1; 0.5)$ matches the Helium ionization potential of $I_p = 24.2$ eV.

In our case, we choose $(q; a^2) = (1; 1.1)$ as this combination provides similarly the first excited state energy of Kr ($\sim$ 10 eV) and the ionization potential is not very high ($\sim$ 17 eV).

A.2.3 Calculating the ground state

In order to start the time propagation, we would need the ground state of the model system. There are mainly two ways to calculate this:

Imaginary time propagation

If we assume that an arbitrary wavefunction $\psi(\mathbf{r}, t)$ can be expanded as from a basics E_n, $\psi_n(\mathbf{r})$ as: [232]

$$\psi(\mathbf{r}, t) = \sum_n c_n \cdot \exp(-iE_n t)\psi_n(\mathbf{r}) \tag{A.16}$$

then by replacing $\delta t = -i \cdot \delta t$, the above equation can be rewritten as:

$$\psi(\mathbf{r}, \delta t) = \sum_n c_n \cdot \exp(-E_n \delta t)\psi_n(\mathbf{r}) \tag{A.17}$$

Eq. A.17 means that after some propagation time, the newly calculated wavefunction will be mainly contributed by the ground state wavefunction (with minimum E_0) $\psi_0(\mathbf{r})$. Therefore, one has to implement the time propagation perfectly, then run the imaginary time propagation to get the ground state wavefunction. Only then one would be able to run the *real* time propagation.

Diagonalization of the Hamiltonian

The other method follows precisely the definition of the Schrödinger equation: the energies are the eigenvalues of the stationary Hamiltonian and the wavefunctions are its eigenvectors. We can write the Hamiltonian (Eq. A.14) in the matrix form:

$$\mathbf{H} = \frac{-\hbar^2}{2m} \begin{pmatrix} -2 & 1 & 0 & \cdots & 0 \\ 1 & -2 & 1 & \cdots & 0 \\ 0 & 1 & -2 & \cdots & 0 \\ \vdots & \vdots & \vdots & \ddots & \vdots \\ 0 & 0 & 0 & 1 & -2 \end{pmatrix} + \begin{pmatrix} V(x_0) & 0 & 0 & \cdots & 0 \\ 0 & V(x_1) & 0 & \cdots & 0 \\ 0 & 0 & V(x_2) & \cdots & 0 \\ \vdots & \vdots & \vdots & \ddots & \vdots \\ 0 & 0 & 0 & 0 & V(x_n) \end{pmatrix} \tag{A.18}$$

where the term $\frac{\partial^2}{\partial x^2}$ has been replaced by the corresponding matrix operator which can be easily proven (second order finite difference). $V(x)$ is purely a 1D potential that we have constructed using the soft-core model (without the electric field). Once the Hamiltonian is written in the matrix form, its eigenvalues and eigenvectors can be easily found using standard mathematical packages.

A.2.4 Time propagation: split operator method

Since the solution of the TDSE can be written as in Eq. 1.3, in order to get the numerical solution, we have to evaluate Eq. 1.3 at single time propagation steps. However, it is not straightforward to evaluate $\mathbf{H}$ because $\mathbf{H}$ involves both $\mathbf{V}$ - which can be directly evaluated in real space - and $\mathbf{T}$ which cannot be directly evaluated in real space. Fleck and Feit *et al.* [233, 234] have developed a novel propagation scheme that can be used both for solving the pulse propagation using the wave equation or to solve the TDSE (they are both hyperbolic type of PDE only with an exception that the TDSE has an imaginary i included). The technique involves switching the basis (or spaces) that we can directly evaluate the operators in combination with a symmetric splitting of the kinetic (or potential) operator [232, 235]:

$$\exp\left(\frac{-i\Delta t\mathbf{H}}{\hbar}\right) = \exp\left(\frac{-i\Delta t\mathbf{V}}{2\hbar}\right)\exp\left(\frac{-i\Delta t\mathbf{T}}{\hbar}\right)\exp\left(\frac{-i\Delta t\mathbf{V}}{2\hbar}\right) + O(\Delta t^3) \tag{A.19}$$

or equivalently:

$$\exp\left(\frac{-i\Delta t\mathbf{H}}{\hbar}\right) = \exp\left(\frac{-i\Delta t\mathbf{T}}{2\hbar}\right)\exp\left(\frac{-i\Delta t\mathbf{V}}{\hbar}\right)\exp\left(\frac{-i\Delta t\mathbf{T}}{2\hbar}\right) + O(\Delta t^3) \tag{A.20}$$

Since we represent our wavefunction $|\Psi(x,t)\rangle = |\Psi(\mathbf{r},t)\rangle$, the term $\exp\left(\frac{-i\Delta t\mathbf{V}}{2\hbar}\right)|\Psi(x,t)\rangle$ can be directly evaluated with $\mathbf{V} = V(x)$ as an array (not a matrix). However, the term $\frac{-\hbar^2}{2m}\frac{\partial^2}{\partial x^2}$ as the kinetic operator cannot be evaluated that easily. Nevertheless, as we have from Eq. A.4, the derivatives here can be evaluated through the Fourier transforms. More specifically, the kinetic operator acting on the wavefunction for a limited time step Δt can be solved as:

$$\exp\left(\frac{-i\Delta t\mathbf{T}}{\hbar}\right)|\Psi(x,0)\rangle = \mathfrak{F}^{-1}\left[\exp\left(\frac{-i\Delta t}{\hbar}\cdot -k^2\cdot\mathfrak{F}\Big[\Psi(x,0)\Big]\right)\right] \tag{A.21}$$

where k is the Fourier counterpart of the real-space coordinate x. Eventually, the wavefunction in the next time step can be fully calculated as:

$$|\Psi(x,\Delta t)\rangle = \exp\left(\frac{-i\Delta t V(x)}{2\hbar}\right)\cdot\mathfrak{F}^{-1}\left[\exp\left(\frac{-i\Delta t}{\hbar}\cdot -k^2\cdot\mathfrak{F}\Big[\exp\left(\frac{-i\Delta t V(x)}{2\hbar}\right)\cdot|\Psi(x,0)\rangle\Big]\right)\right] \tag{A.22}$$

A.2.5 Boundary condition

Usually we have to specify the grid in real space big enough such that the electron wavefunction is fully captured. However, there is always small part of the wavefunction extends to the boundary of the grid. If this is not treated carefully, it will be reflected back and the simulation will give inaccurate results.

There are mainly two ways to circumvent such an effect: use a smooth filter to cut down the amplitudes of the wavefunctions that are near the two edges; apply an imaginary potential (absorbing potential) as discussed in [235]. In our simulation, a simple hyper-Gaussian filter is used.

A.2.6 Extracting the polarization response

Once we have the full wavefunction as a function of time $|\Psi(x,t)\rangle$, an usual observable is the time dependent dipole moment that could be extracted as:

$$d(t) = \langle \Psi(x,t)| \, x \, |\Psi(x,t)\rangle \tag{A.23}$$

and the resultant emission spectrum can be evaluated routinely as $S(\omega) = \left|\mathfrak{F}\left[d(t)\right]\right|^2$.

Moreover, if we look at the form of A.23 which heavily weights the behavior of the electrons far from the center as opposed to the physical reality that the center and the edges should have equal contributions. Therefore, K. J. Schafer *et al.* [80] suggested that instead of evaluating the dipole moment as above, one can perform similar calculation but on the acceleration of the electrons:

$$a(t) = \frac{d^2}{dt^2}\langle x\rangle = -\langle [\mathbf{H}, [\mathbf{H}, x]]\rangle \tag{A.24}$$

and consequently the emitted spectrum can be calculated as: $S_2(\omega) = \left|\mathfrak{F}\left[a(t)\right]/\omega^2\right|^2$.

However, within the scope of our simulations, we have not found that the second method is superior to the original one. It only took more calculation time because of the evaluation of the commutators. Therefore we used the first method in all of our calculations.

A.2.7 Results

Figure A.1 shows a typical result calculated from the 1D TDSE for an attosecond light transient. Since we used the soft core potential thus the potential does not drop to $-\infty$ as we approach the center of the system (Fig. A.1b). The ground state wavefunction (Fig. A.1c) was calculated using both methods and they give consistent energy at a precision of $< 0.1\%$. The dipole response of the system (Fig. A.1d) exhibits a very strong linear response. All the nonlinear responses are too weak to be seen in this scale. The emitted spectrum shows, as a result, a very strong fundamental spectrum (spectrum of the incident laser) and resonant lines start to show up at ~ 10 eV and more. This is in agreement with experiments since at the same intensity of $1 \cdot 10^{13}$ W/cm^2, only some resonant emissions are recorded. In order to have HHG, the incident laser pulses have to have much higher peak intensity (of the order of 10^{14} W/cm^2 and more).

Finally, if we compare the global phase spectrogram in Fig. A.1f to the experimental results (Fig. 5.3) and simulated results using two level model (Fig. 5.1), a striking agreement can be reached: they both show strong emission of VUV radiation when the global phase is zero and drops strongly otherwise. Even though there are deviations of the 1D TDSE to the experimental results, this already gives us a powerful tool to validate other simpler simulations: optical Bloch equations or simple high order nonlinearities.

Improvement of the current 1D TDSE to the full 3D code could give a lot more reliability in terms of interpreting the experimental results.

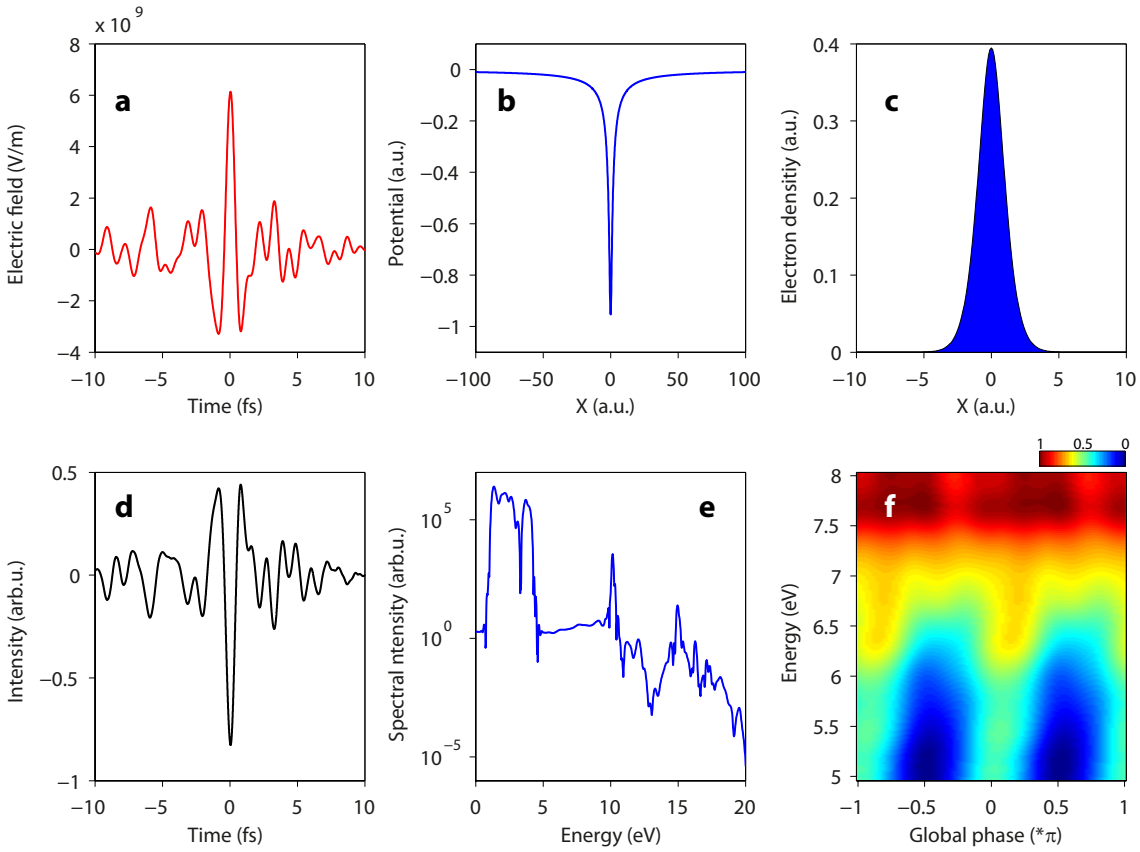

Figure A.1: One dimensional Time Dependent Schrödinger Equation. **a,** Electric field used in the simulation at $\varphi = 0$ and peak intensity $I = 1 \cdot 10^{13}$ W/cm^2. **b,** Soft core potential at (1;1.1). **c,** Normalized electron density (zoomed in). **d,** Dipole response. One cannot see the ripples after the peak of the pulses because they are too weak to be seen in this scale. **e,** Emitted spectrum. **f,** Spectrogram of the dipole response at different global phase settings of the electric field in **a,**.

A.3 Optical Bloch equations

Usually it is hard to separate different physical processes which are involved thus here we would like to turn to a simpler approach where instead of describing the complete electronic wave function, we represent the system using density operator. The equation governs the motion in this representation is then called *Optical Bloch Equation*.

A.3.1 Density matrix and its time evolution

The topic of density operator and its formalism was first pioneered by J. von Neumann in 1927 that could describe physical observables by a combination of pure and mix states. Later, it is covered in brief in quantum mechanics textbooks [236] and there is a full book devoted for it by Karl Blum [237]. However, here we will just derive its application for our experiments.

Consider a general case for a N-level system where we could write the Hamiltonian

as the sum of the system (field free) Hamiltonian $\mathbf{H_0}$ plus an interaction $\mathbf{H}(t)$ with an optical light field $\mathbf{E}(t)$:

$$\mathbf{H} = \mathbf{H_0} + \mathbf{H}(t) \tag{A.25}$$

with $\mathbf{H}(t) = -\mu \cdot \mathbf{E}(t)$ and the $\mathbf{H_0}$ is expressed by:

$$\mathbf{H_0} = \begin{pmatrix} \epsilon_1 & 0 & \cdots & 0 \\ 0 & \epsilon_2 & \cdots & 0 \\ \vdots & \vdots & \ddots & \vdots \\ 0 & 0 & \cdots & \epsilon_n \end{pmatrix} \tag{A.26}$$

Here, $\epsilon_1, \epsilon_2, \ldots \epsilon_n$ are the energies of the first (ground) and second (first excited), ... and n^{th} state. μ is the so-called transition dipole operator or dipole matrix element d_{ij}. Since the transition probability from i^{th} state to j^{th} state has to be equal to the transition from j^{th} state to i^{th} state. This means $\mu_{ij} = \mu_{ji}$

$$\mu = \begin{pmatrix} 0 & \mu_{12} & \cdots & \mu_{1n} \\ \mu_{21} & 0 & \cdots & \mu_{2n} \\ \vdots & \vdots & \ddots & \vdots \\ \mu_{n1} & \mu_{n2} & \cdots & 0 \end{pmatrix} \tag{A.27}$$

All the values of μ_{1j} or μ_{i1} are found based on the strength of those resonant lines. One can use to the great extent the database from NIST [238] which includes oscillator strengths for variety of systems. The other off-diagonal elements are hard to find because they depend strongly on the particular simulation we are aiming at. After taking these dipole matrix elements into account, we can rewrite A.25 as

$$\mathbf{H} = \begin{pmatrix} \epsilon_1 & -\mu_{12} \cdot E(t) & \cdots & -\mu_{1n} \cdot E(t) \\ -\mu_{21} \cdot E(t) & \epsilon_2 & \cdots & -\mu_{2n} \cdot E(t) \\ \vdots & \vdots & \ddots & \vdots \\ -\mu_{n1} \cdot E(t) & -\mu_{n2} \cdot E(t) & \cdots & \epsilon_n \end{pmatrix} \tag{A.28}$$

By changing the representation of the system to density matrix instead of wave function, we then come up to the *Liouville - von Neumann* equation instead of the Schrödinger equation 1.2:

$$\frac{d}{dt}\rho = \frac{1}{\mathrm{i}\hbar}[\mathbf{H}, \rho] \tag{A.29}$$

Here $\rho = \rho_{ij}$ is density matrix representing the system of interest. The diagonal terms are the population of the system in the ground state ρ_{11} and the excited states ρ_{ii}. All the off diagonal terms are representing the *polarization or coherence* of the transitions between the states.

At this step, the equation A.29 is practically coupled differential equations (ODEs). They can be ordinary of partial differential equations, depending on the choice of the EM field gauge. The total number of ODEs is n^2 where n is the number of energy levels taken into account in the simulation. We can effectively numerically integrate these in a matrix form using any of the time integrators (Runge-Kutta or multi-steps,...) to solve

these as a function of time. Practically in this case, a fourth order Runge-Kutta (RK4) provides acceptable precision.

Finally, after solving equation A.29 to find $\rho_{ij}(t)$, we can calculate the polarization response of the system using the quantum mechanical averaging of the transition dipole moment:

$$d(t) = \sum_{i,j} \mu_{ij} \cdot \big[\rho_{ij}(t) + \rho_{ji}(t)\big] = 2\mathfrak{Re}\big[\sum_{i,j} \mu_{ij} \cdot \rho_{i,j}(t)\big] \tag{A.30}$$

Dephasing or relaxation times

Nevertheless, the equation A.29 in this form by definition does not take into account the natural dephasing (relaxation) time of the states which results in the fact that the solution of this equation will give infinitely narrow spectral lines in principle. In practice, the linewidth of the resonant lines is defined by the propagation time (the time span at which we let the integrator run). We can practically cut this propagation time such that the simulated line-widths are similar to reality. However, there is a much more elegant way, which is to account for the natural line broadening of the states by adding the dephasing phenomenologically Γ_{ij} as ([239], eq. 62):

$$\frac{d}{dt}\rho = \frac{1}{\mathrm{i}\hbar}[\mathbf{H}, \rho] - \rho^{\Gamma} \tag{A.31}$$

where $\rho^{\Gamma} = \rho^{\Gamma}_{ij} = \Gamma_{ij} \cdot \rho_{ij}$.

However, in this case one should be very careful since Γ_{ij} is a *total effective dephasing rate*. This is by no means a complete description of the natural dephasing (relaxation) of the model system interacting with a thermal bath. Detailed consideration of the system in this interaction relaxing to the thermal equilibrium is treated in the excellent book of Mukamel ([240], Appendix 6A). Nonetheless, the for purpose of our thesis, this simple treatment turns out to be very useful and this applies to an open system (whereas the consideration in [240] deals with a closed system) where in reality the excited states naturally decay, specifying the openness of the system of interest.

Equation A.31 in general can provide great intuitive understanding of the system under the influence of the laser pulses. As long as the pulses does not contain several cycles (approximately one cycle and less in our case) and its peak electric field is weak enough (less than $\sim 1V/\text{Å} \leftrightarrow I_{\text{peak}}$ less than $4 \cdot 10^{13}\, W/cm^2$) the response of the N level system is close to the response calculated from the TDSE meaning that the description using pure and mixed states here is an accurate description of the system under weak fields. It does not only capture the resonant emissions (intrinsic properties) but also captures very well the perturbative behavior of the system. Furthermore, under influence of incoming electric field, the shift of the energy levels (AC Stark shift) is also described by diagonalizing the time dependent Hamiltonian of the system.

In conclusion, using the density matrix approach together with the inclusion of the relaxation time, one could possibly investigate the behavior of a quantum system under relatively weak electric fields.

A.4 Polarization expressed through nonlinear optical susceptibilities

Here, we attempt to deconvolute the response of the system even further by working in the perturbative picture. From the perturbation theory applied on the system under interaction with an external field [75] as in Chapter 1, Eq. 1.1, the polarization can be rewritten as:

$$\mathbf{P}(t) = \epsilon_0\big[\chi^{(1)}\mathbf{E}(t) + \chi^{(2)}\mathbf{E}(t)^2 + \chi^{(3)}\mathbf{E}(t)^3 + \chi^{(4)}\mathbf{E}(t)^4 + \chi^{(5)}\mathbf{E}(t)^5 + \dots\big] \tag{A.32}$$

Because the system of interest is Kr gas, its inversion symmetry destroys the even order terms as $\chi^{(2)}, \chi^{(4)}, \dots = 0$, leaving only the odd order terms to be effective. Therefore the total polarization of the system can be rewritten as $\mathbf{P}(t) = \epsilon_0\big[\chi^{(1)}\mathbf{E}(t) + \chi^{(3)}\mathbf{E}(t)^3 + \chi^{(5)}\mathbf{E}(t)^5 + \dots\big]$.

On the other hand, if we break down the incident electric field $E(t)$ assuming linear polarization $\mathbf{E}(t) = E(t)$ as:

$$E(t) = \frac{E_{\text{envelope}}(t)\cdot e^{i\varphi(t)} + E_{\text{envelope}}(t)\cdot e^{-i\varphi(t)}}{2} = \frac{E_H(t) + E_H(t)^*}{2}, \tag{A.33}$$

where $E_H(t) = \mathfrak{H}[E(t)]$ is the Hilbert transform of the real electric field, its envelope can be described as $E_{\text{envelope}}(t) = |E_H(t)|$, and its phase is $\varphi(t) = \tan^{-1}\big[\text{Im}[E_H(t)]/\text{Re}[E_H(t)]\big]$. Finally, using this decomposition, we can rewrite the total polarization, neglecting the linear part, as:

$$P(t) \propto \chi^{(3)}\cdot\left[\frac{\overbrace{E_H(t)^3}^{THG} + \overbrace{3E_H(t)^2E_H(t)^* + 3E_H(t)E_H(t)^{*2}}^{\text{SPM-like}} + \overbrace{E_H(t)^{*3}}^{THG}}{8}\right] \tag{A.34a}$$

$$+\chi^{(5)}\cdot\left[\frac{\overbrace{E_H(t)^5}^{FHG} + \overbrace{5E_H(t)^4E_H(t)^* + \dots + 5E_H(t)E_H(t)^{*4}}^{\text{other terms}} + \overbrace{E_H(t)^{*5}}^{FHG}}{32}\right] + \dots \tag{A.34b}$$

Fig. A.2 shows possible multi-photon pathways (a) as well as the effective spectral bandwidths associated to different nonlinear processes (b) for the case of optical attosecond pulses. One can easily see that all the spectrum of interest (5.5 → 14 e) can be well captured by the third and fifth order nonlinear susceptibilities. However, if one try to separate the third order processes into third harmonic generation (THG) and self-phase-modulation-like as suggested in Eq. A.34, each of them will contribute to a *different* final spectrum, Fig. A.2. From this point on, the physical picture describing the measured non-resonant VUV emission is almost transparent. From 5.5 to 8.0 eV, there are contributions from the THG as well as SPM processes. Each of these processes carry their intrinsically different phases ($3\varphi(t)$ and $\varphi(t)$) while the total third order susceptibility ($\chi^{(3)}$) takes all of them into account. As a result, their interference patterns change dynamically as a function of the amplitude and phase of each process.

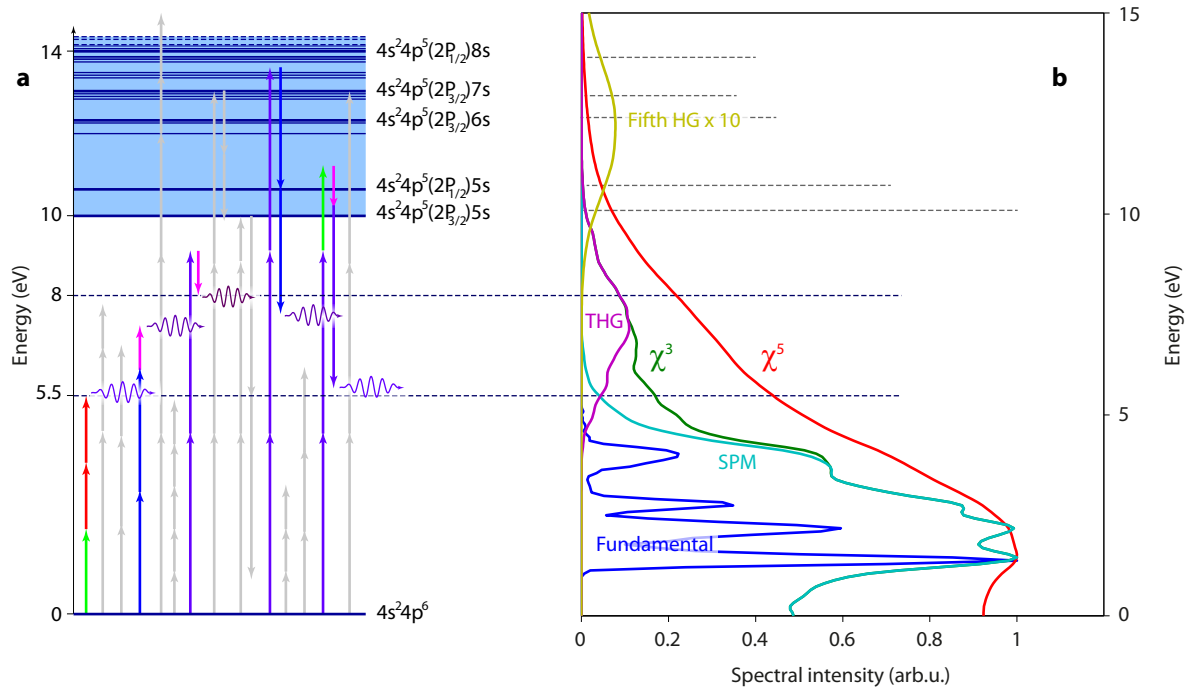

Figure A.2: Perturbative response - multi-photon picture. **a,** Representative multi-photon transitions on a Kr Jablonski diagram assuming third and fifth order nonlinearity. Representative resonant transitions are indicated as horizontal solid blue lines. Light gray arrows indicate few, out of infinite, possible transitions. **b,** Spectra corresponding to the fundamental incident light (solid blue curve), self-phase-modulation-like process (solid cyan curve), third harmonic generation (solid purple curve), third order nonlinearity (solid green curve), fifth order nonlinearity (solid red curve) and fifth order harmonic generation (solid yellow curve, multiplied by 10 times because it is very weak). Horizontal dashed gray lines on top left are representative resonant lines and their relative strength.

Evaluation of the Eq. A.34 in the non-resonant part of the VUV spectrum (not shown here) yields almost identical spectrograms as the ones calculated from the two level model for all the incident electric fields (single-cycle pulses, optical attosecond pulses and chirped optical attosecond pulses). Therefore, one can conclude that the main features recorded from the VUV spectrograms can be explained intuitively by the third order susceptibility (or related third order processes). However, more importantly, it imposes a condition at which such a strong global phase dependence as in Fig. 5.3b can exist, that the effective spectral bandwidth has to be sufficiently broad, the THG and the SPM terms expand strongly such that they have spectral overlap. It is this spectral overlap that significantly affects VUV spectral amplitude as a function of the global phase. It is without this critical condition that a single-cycle pulse (Fig. 5.3f) could not show any global phase dependence effect.

A.5 Supercontinuum generation in hollow core fiber

A.5.1 Pulse duration versus gas pressure

This is the measurement done with channel 3 of the TW synthesizer ($\lambda = 500 - 670$nm).

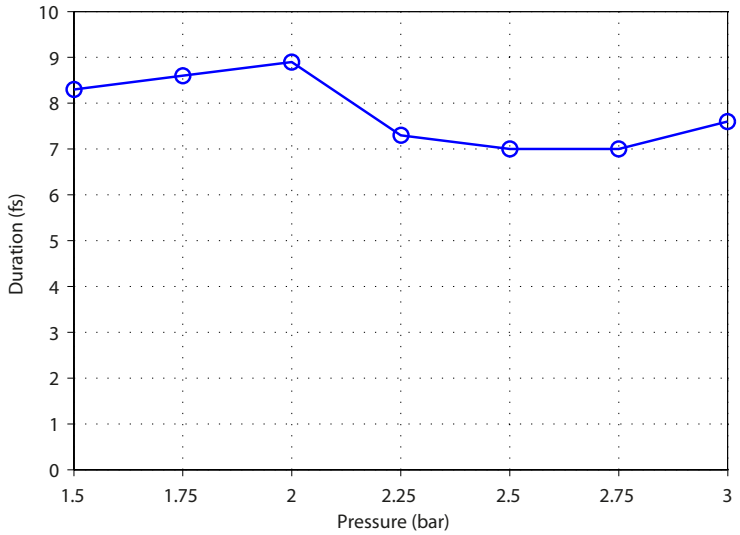

Figure A.3: Duration of the channel 3 in the TW synthesizer as a function of the hollow core fiber gas pressure.

From the figure A.3 we can see that in this particular case, the pulse duration or the second order of the chirp does not change so much. From an equal simulation (similar bandwidth or pulse duration), the change of chirp in this case is $\leq 200\,\mu m$ of Fused Silica. As a result, we could safely say that the nonlinearities causing the supercontinuum do not change so much the spectral phase within *each* individual channel. Thus the individual channels after the end of the fiber (not the fiber housing which includes the Brewster windows) are close to Fourier Limit (the dispersion induced by the gas itself is very small - theoretically expected).

One observation: an increase in the pressure goes a long with a very slight change in the chirp recorded in the FROG. We saw that the FROG traces get chirped toward negative direction (negatively chirped) once we increased the pressure inside the fiber housing. However, this change is very subtle as indicated by the pulse duration.

A.5.2 Output power versus gas pressure

Figure A.4 shows us the different measured powers with respect to pressure changes. So for this channel, the power drops around only $\sim 8\%$ when we increase the pressure by almost twice. This shows the insensitivity of the output power to the gas pressure, most likely due to the long carrier wave this channel posses.

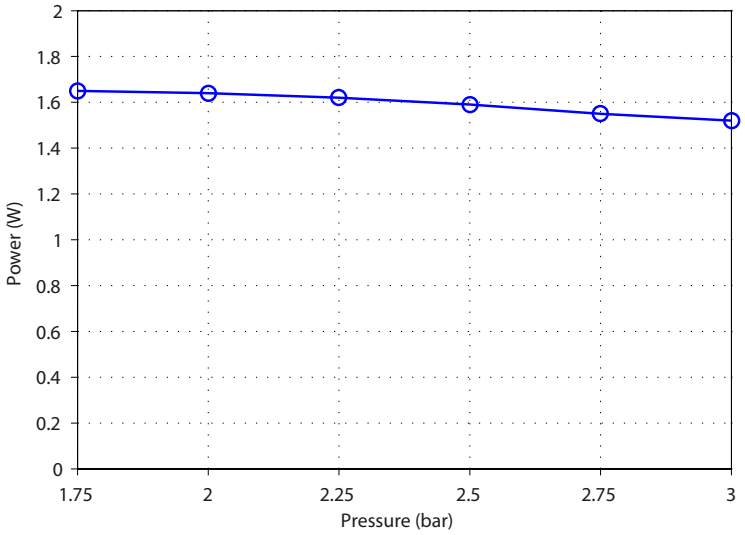

Figure A.4: Power throughput as a function of the gas pressure of the same channel 3.

Appendix B

Data Archiving

The experimental raw data, evaluation files, and original figures can be found on the Data Archive Server of the Laboratory for Attosecond Physics at the Max Planck Institute of Quantum Optics:
`/afs/rzg/mpq/lap/publication_archive`

The data are organized as follows:
\Chapter_X\Figs\X.X.X
with X is the number specifying the order of the chapters or figures.

Inside each chapter, there would be corresponding figures. All the raw experimental data, Matlab codes and .pdf figures are stored by the corresponding name in the corresponding figure folder.

List of Figures

List of Tables

Bibliography

[1] N. Kaiser and Hans K. Pulker. *Optical Interference Coatings*. Springer, Germany, 2003.

[2] T. H. Maiman. Stimulated optical radiation in ruby. *Nature*, 187(4736):493–494, 1960.

[3] P. A. Franken, G. Weinreich, C. W. Peters, and A. E. Hill. Generation of optical harmonics. *Physical Review Letters*, 7(4):118–, 1961.

[4] F. Krausz and M. Ivanov. Attosecond physics. *Reviews of Modern Physics*, 81(1):163–234, 2009.

[5] O. Svelto, S. De Silvestri, and G. Denardo. *Ultrafast Processes in Spectroscopy*. Springer, Germany, 1996.

[6] A. H. Zewail. Femtochemistry: atomic-scale dynamics of the chemical bond using ultrafast lasers (nobel lecture) copyright((c)) the nobel foundation 2000. we thank the nobel foundation, stockholm, for permission to print this lecture. *Angew Chem Int Ed Engl*, 39(15):2586–2631, 2000.

[7] T. Udem, R. Holzwarth, and T. W. Hansch. Optical frequency metrology. *Nature*, 416(6877):233–237, 2002.

[8] R. Sabella and P. Lugli. *High Speed Optical Communications*. Springer, Germany, 1999.

[9] D. Huang, E. A. Swanson, C. P. Lin, J. S. Schuman, W. G. Stinson, W. Chang, M. R. Hee, T. Flotte, K. Gregory, C. A. Puliafito, and J. G. Fujimoto. Optical coherence tomography. *Science*, 254(5035):1178–1181, 1991.

[10] J. R. V. de Aldana, P. Moreno, and L. Roso. Ultrafast lasers: A new frontier for optical materials processing. *Optical Materials*, 34(3):572–578, 2012.

[11] E. Goulielmakis, V. S. Yakovlev, A. L. Cavalieri, M. Uiberacker, V. Pervak, A. Apolonski, R. Kienberger, U. Kleineberg, and F. Krausz. Attosecond control and measurement: Lightwave electronics. *Science*, 317(5839):769–775, 2007.

[12] P. B. Corkum. Plasma perspective on strong-field multiphoton ionization. *Physical Review Letters*, 71(13):1994–1997, 1993.

[13] L. V. Keldysh. Ionization in field of a strong electromagnetic wave. *Soviet Physics Jetp-Ussr*, 20(5):1307, 1965.

[14] O. Smirnova, Y. Mairesse, S. Patchkovskii, N. Dudovich, D. Villeneuve, P. Corkum, and M. Y. Ivanov. High harmonic interferometry of multi-electron dynamics in molecules. *Nature*, 460(7258):972–977, 2009.

[15] N. Dudovich, O. Smirnova, J. Levesque, Y. Mairesse, M. Y. Ivanov, D. M. Villeneuve, and P. B. Corkum. Measuring and controlling the birth of attosecond xuv pulses. *Nature Physics*, 2(11):781–786, 2006.

[16] K. T. Kim, C. M. Zhang, A. D. Shiner, S. E. Kirkwood, E. Frumker, G. Gariepy, A. Naumov, D. M. Villeneuve, and P. B. Corkum. Manipulation of quantum paths for space-time characterization of attosecond pulses. *Nature Physics*, 9(3):159–163, 2013.

[17] M. T. Hassan. *Synthesis and control of attosecond light transients*. PhD thesis, 2013.

[18] R. Ulbricht, E. Hendry, J. Shan, T. F. Heinz, and M. Bonn. Carrier dynamics in semiconductors studied with time-resolved terahertz spectroscopy. *Reviews of Modern Physics*, 83(2):543–586, 2011.

[19] C. Chen, Z. Lin, and Z. Wang. The development of new borate-based uv nonlinear optical crystals. *Applied Physics B-Lasers and Optics*, 80(1):1–25, 2005.

[20] M. Ferray, A. Lhuillier, X. F. Li, L. A. Lompre, G. Mainfray, and C. Manus. Multiple-harmonic conversion of 1064-nm radiation in rare-gases. *Journal of Physics B-Atomic Molecular and Optical Physics*, 21(3):L31–L35, 1988.

[21] C. Spielmann, N. H. Burnett, S. Sartania, R. Koppitsch, M. Schnurer, C. Kan, M. Lenzner, P. Wobrauschek, and F. Krausz. Generation of coherent x-rays in the water window using 5-femtosecond laser pulses. *Science*, 278(5338):661–664, 1997.

[22] T. Popmintchev, M. C. Chen, D. Popmintchev, P. Arpin, S. Brown, S. Alisauskas, G. Andriukaitis, T. Balciunas, O. D. Mucke, A. Pugzlys, A. Baltuska, B. Shim, S. E. Schrauth, A. Gaeta, C. Hernandez-Garcia, L. Plaja, A. Becker, A. Jaron-Becker, M. M. Murnane, and H. C. Kapteyn. Bright coherent ultrahigh harmonics in the kev x-ray regime from mid-infrared femtosecond lasers. *Science*, 336(6086):1287–1291, 2012.

[23] M. Lewenstein, P. Balcou, M. Y. Ivanov, A. Lhuillier, and P. B. Corkum. Theory of high-harmonic generation by low-frequency laser fields. *Physical Review A*, 49(3):2117–2132, 1994.

[24] D. Vonderlinde, T. Engers, G. Jenke, P. Agostini, G. Grillon, E. Nibbering, A. Mysyrowicz, and A. Antonetti. Generation of high-order harmonics from solid-surfaces by intense femtosecond laser-pulses. *Physical Review A*, 52(1):R25–R27, 1995.

[25] G. D. Tsakiris, K. Eidmann, J. Meyer-ter Vehn, and F. Krausz. Route to intense single attosecond pulses. *New Journal of Physics*, 8, 2006.

[26] S. V. Bulanov, N. M. Naumova, and F. Pegoraro. Interaction of an ultrashort, relativistically strong laser-pulse with an overdense plasma. *Physics of Plasmas*, 1(3):745–757, 1994.

[27] R. Lichters, J. MeyerterVehn, and A. Pukhov. Short-pulse laser harmonics from oscillating plasma surfaces driven at relativistic intensity. *Physics of Plasmas*, 3(9):3425–3437, 1996.

[28] S. Gordienko, A. Pukhov, O. Shorokhov, and T. Baeva. Relativistic doppler effect: Universal spectra and zeptosecond pulses. *Physical Review Letters*, 93(11), 2004.

[29] A. Baltuska, T. Udem, M. Uiberacker, M. Hentschel, E. Goulielmakis, C. Gohle, R. Holzwarth, V. S. Yakovlev, A. Scrinzi, T. W. Hansch, and F. Krausz. Attosecond control of electronic processes by intense light fields. *Nature*, 421(6928):611–615, 2003.

[30] E. Goulielmakis, M. Schultze, M. Hofstetter, V. S. Yakovlev, J. Gagnon, M. Uiberacker, A. L. Aquila, E. M. Gullikson, D. T. Attwood, R. Kienberger, F. Krausz, and U. Kleineberg. Single-cycle nonlinear optics. *Science*, 320(5883):1614–1617, 2008.

[31] H. J. Worner, J. B. Bertrand, D. V. Kartashov, P. B. Corkum, and D. M. Villeneuve. Following a chemical reaction using high-harmonic interferometry. *Nature*, 466(7306):604–607, 2010.

[32] S. Baker, J. S. Robinson, C. A. Haworth, H. Teng, R. A. Smith, C. C. Chirila, M. Lein, J. W. G. Tisch, and J. P. Marangos. Probing proton dynamics in molecules on an attosecond time scale. *Science*, 312(5772):424–427, 2006.

[33] W. Denk, J. H. Strickler, and W. W. Webb. Two-photon laser scanning fluorescence microscopy. *Science*, 248(4951):73–6, 1990.

[34] M. Hentschel, R. Kienberger, C. Spielmann, G. A. Reider, N. Milosevic, T. Brabec, P. Corkum, U. Heinzmann, M. Drescher, and F. Krausz. Attosecond metrology. *Nature*, 414(6863):509–513, 2001.

[35] Y. Mairesse, A. de Bohan, L. J. Frasinski, H. Merdji, L. C. Dinu, P. Monchicourt, P. Breger, M. Kovacev, R. Taieb, B. Carre, H. G. Muller, P. Agostini, and P. Salieres. Attosecond synchronization of high-harmonic soft x-rays. *Science*, 302(5650):1540–1543, 2003.

[36] G. Sansone, E. Benedetti, F. Calegari, C. Vozzi, L. Avaldi, R. Flammini, L. Poletto, P. Villoresi, C. Altucci, R. Velotta, S. Stagira, S. De Silvestri, and M. Nisoli. Isolated single-cycle attosecond pulses. *Science*, 314(5798):443–446, 2006.

[37] P. Tzallas, E. Skantzakis, L. A. A. Nikolopoulos, G. D. Tsakiris, and D. Charalambidis. Extreme-ultraviolet pump-probe studies of one-femtosecond-scale electron dynamics. *Nature Physics*, 7(10):781–784, 2011.

[38] Rodrigo López-Martens, Katalin Varjú, Per Johnsson, Johan Mauritsson, Yann Mairesse, Pascal Salières, Mette B. Gaarde, Kenneth J. Schafer, Anders Persson, Sune Svanberg, Claes-Göran Wahlström, and Anne LHuillier. Amplitude and phase control of attosecond light pulses. *Physical Review Letters*, 94(3):033001, 2005.

[39] P. M. Paul, E. S. Toma, P. Breger, G. Mullot, F. Auge, P. Balcou, H. G. Muller, and P. Agostini. Observation of a train of attosecond pulses from high harmonic generation. *Science*, 292(5522):1689–1692, 2001.

[40] A. K. Gupta, O. E. Alon, and N. Moiseyev. Generation and control of high-order harmonics by the interaction of an infrared laser with a thin graphite layer. *Physical Review B*, 68(20), 2003.

[41] D. Golde, T. Meier, and S. W. Koch. High harmonics generated in semiconductor nanostructures by the coupled dynamics of optical inter- and intraband excitations. *Physical Review B*, 77(7), 2008.

[42] S. Ghimire, A. D. DiChiara, E. Sistrunk, P. Agostini, L. F. DiMauro, and D. A. Reis. Observation of high-order harmonic generation in a bulk crystal. *Nature Physics*, 7(2):138–141, 2011.

[43] O. Schubert, M. Hohenleutner, F. Langer, B. Urbanek, C. Lange, U. Huttner, D. Golde, T. Meier, M. Kira, S. W. Koch, and R. Huber. Sub-cycle control of terahertz high-harmonic generation by dynamical bloch oscillations. *Nature Photonics*, 8(2):119–123, 2014.

[44] M. W. Feise and D. S. Citrin. Semiclassical theory of terahertz multiple-harmonic generation in semiconductor superlattices. *Applied Physics Letters*, 75(22):3536–3538, 1999.

[45] Oliver D. Mücke. Isolated high-order harmonics pulse from two-color-driven bloch oscillations in bulk semiconductors. *Physical Review B*, 84:081202, 2011.

[46] S. Ghimire, A. D. DiChiara, E. Sistrunk, G. Ndabashimiye, U. B. Szafruga, A. Mohammad, P. Agostini, L. F. DiMauro, and D. A. Reis. Generation and propagation of high-order harmonics in crystals. *Physical Review A*, 85(4), 2012.

[47] P. G. Hawkins and M. Y. Ivanov. Role of subcycle transition dynamics in high-order-harmonic generation in periodic structures. *Physical Review A*, 87(6), 2013.

[48] A. F. Kemper, B. Moritz, J. K. Freericks, and T. P. Devereaux. Theoretical description of high-order harmonic generation in solids. *New Journal of Physics*, 15, 2013.

[49] D. Golde, M. Kira, T. Meier, and S. W. Koch. Microscopic theory of the extremely nonlinear terahertz response of semiconductors. *Physica Status Solidi B-Basic Solid State Physics*, 248(4):863–866, 2011.

[50] A. Assion, T. Baumert, M. Bergt, T. Brixner, B. Kiefer, V. Seyfried, M. Strehle, and G. Gerber. Control of chemical reactions by feedback-optimized phase-shaped femtosecond laser pulses. *Science*, 282(5390):919, 1998.

[51] A. M. Weiner, D. E. Leaird, Gary P. Wiederrecht, and Keith A. Nelson. Femtosecond pulse sequences used for optical manipulation of molecular motion. *Science*, 247(4948):1317–1319, 1990.

[52] S. R. Friberg, A. M. Weiner, Y. Silberberg, B. G. Sfez, and P. S. Smith. Femtosecond switching in a dual-core-fiber nonlinear coupler. *Optics Letters*, 13(10):904–906, 1988.

[53] S. E. Harris and A. V. Sokolov. Subfemtosecond pulse generation by molecular modulation. *Physical Review Letters*, 81(14):2894–2897, 1998.

[54] H. S. Chan, Z. M. Hsieh, W. H. Liang, A. H. Kung, C. K. Lee, C. J. Lai, R. P. Pan, and L. H. Peng. Synthesis and measurement of ultrafast waveforms from five discrete optical harmonics. *Science*, 331(6021):1165–1168, 2011.

[55] Moshe Shapiro and Paul Brumer. *Quantum control of molecular processes*. Wiley-VCH, Weinheim, 2012.

[56] S. T. Cundiff, M. Koch, W. H. Knox, J. Shah, and W. Stolz. Optical coherence in semiconductors: Strong emission mediated by nondegenerate interactions. *Physical Review Letters*, 77(6):1107, 1996.

[57] D. Meshulach and Y. Silberberg. Coherent quantum control of two-photon transitions by a femtosecond laser pulse. *Nature*, 396(6708):239, 1998.

[58] A. Wirth, M. T. Hassan, I. Grguras, J. Gagnon, A. Moulet, T. T. Luu, S. Pabst, R. Santra, Z. A. Alahmed, A. M. Azzeer, V. S. Yakovlev, V. Pervak, F. Krausz, and E. Goulielmakis. Synthesized light transients. *Science*, 334(6053):195–200, 2011.

[59] S. W. Huang, G. Cirmi, J. Moses, K. H. Hong, S. Bhardwaj, J. R. Birge, L. J. Chen, E. Li, B. J. Eggleton, G. Cerullo, and F. X. Kartner. High-energy pulse synthesis with sub-cycle waveform control for strong-field physics. *Nature Photonics*, 5(8):475, 2011.

[60] M. Ivanov, P. B. Corkum, T. Zuo, and A. Bandrauk. Routes to control of intense-field atomic polarizability. *Physical Review Letters*, 74(15):2933–2936, 1995.

[61] P. B. Corkum and F. Krausz. Attosecond science. *Nature Physics*, 3(6):381, 2007.

[62] A. Schiffrin, T. Paasch-Colberg, N. Karpowicz, V. Apalkov, D. Gerster, S. Muhlbrandt, M. Korbman, J. Reichert, M. Schultze, S. Holzner, J. V. Barth, R. Kienberger, R. Ernstorfer, V. S. Yakovlev, M. I. Stockman, and F. Krausz. Optical-field-induced current in dielectrics. *Nature*, 493(7430):70–74, 2013.

[63] E. Goulielmakis, Z. H. Loh, A. Wirth, R. Santra, N. Rohringer, V. S. Yakovlev, S. Zherebtsov, T. Pfeifer, A. M. Azzeer, M. F. Kling, S. R. Leone, and F. Krausz. Real-time observation of valence electron motion. *Nature*, 466(7307):739, 2010.

[64] M. F. Kling, C. Siedschlag, A. J. Verhoef, J. I. Khan, M. Schultze, T. Uphues, Y. Ni, M. Uiberacker, M. Drescher, F. Krausz, and M. J. J. Vrakking. Control of electron localization in molecular dissociation. *Science*, 312(5771):246–248, 2006.

[65] P. Eckle, A. N. Pfeiffer, C. Cirelli, A. Staudte, R. Dorner, H. G. Muller, M. Buttiker, and U. Keller. Attosecond ionization and tunneling delay time measurements in helium. *Science*, 322(5907):1525–1529, 2008.

[66] R. Kienberger, E. Goulielmakis, M. Uiberacker, A. Baltuska, V. Yakovlev, F. Bammer, A. Scrinzi, Th Westerwalbesloh, U. Kleineberg, U. Heinzmann, M. Drescher, and F. Krausz. Atomic transient recorder. *Nature*, 427(6977):817, 2004.

[67] Kun Zhao, Qi Zhang, Michael Chini, Yi Wu, Xiaowei Wang, and Zenghu Chang. Tailoring a 67 attosecond pulse through advantageous phase-mismatch. *Optics Letters*, 37(18):3891–3893, 2012.

[68] Hiroki Mashiko, M. Justine Bell, Annelise R. Beck, Mark J. Abel, Philip M. Nagel, Colby P. Steiner, Joseph Robinson, Daniel M. Neumark, and Stephen R. Leone. Tunable frequency-controlled isolated attosecond pulses characterized by either 750 nm or 400 nm wavelength streak fields. *Optics Express*, 18(25):25887–25895, 2010.

[69] M. Schultze, E. M. Bothschafter, A. Sommer, S. Holzner, W. Schweinberger, M. Fiess, M. Hofstetter, R. Kienberger, V. Apalkov, V. S. Yakovlev, M. I. Stockman, and F. Krausz. Controlling dielectrics with the electric field of light. *Nature*, 493(7430):75–78, 2013.

[70] Ch Neidel, J. Klei, C. H. Yang, A. Rouzée, M. J. J. Vrakking, K. Klünder, M. Miranda, C. L. Arnold, T. Fordell, A. LHuillier, M. Gisselbrecht, P. Johnsson, M. P. Dinh, E. Suraud, P. G. Reinhard, V. Despré, M. A. L. Marques, and F. Lépine. Probing time-dependent molecular dipoles on the attosecond time scale. *Physical Review Letters*, 111(3):033001, 2013.

[71] G. Sansone, F. Kelkensberg, J. F. Perez-Torres, F. Morales, M. F. Kling, W. Siu, O. Ghafur, P. Johnsson, M. Swoboda, E. Benedetti, F. Ferrari, F. Lepine, J. L. Sanz-Vicario, S. Zherebtsov, I. Znakovskaya, A. LHuillier, M. Yu Ivanov, M. Nisoli, F. Martin, and M. J. J. Vrakking. Electron localization following attosecond molecular photoionization. *Nature*, 465(7299):763–766, 2010.

[72] M. Schultze, M. Fiess, N. Karpowicz, J. Gagnon, M. Korbman, M. Hofstetter, S. Neppl, A. L. Cavalieri, Y. Komninos, Th. Mercouris, C. A. Nicolaides, R. Pazourek, S. Nagele, J. Feist, J. Burgdörfer, A. M. Azzeer, R. Ernstorfer, R. Kienberger, U. Kleineberg, E. Goulielmakis, F. Krausz, and V. S. Yakovlev. Delay in photoemission. *Science*, 328(5986):1658–1662, 2010.

[73] J. Mauritsson, T. Remetter, M. Swoboda, K. Klunder, A. L'Huillier, K. J. Schafer, O. Ghafur, F. Kelkensberg, W. Siu, P. Johnsson, M. J. J. Vrakking, I. Znakovskaya, T. Uphues, S. Zherebtsov, M. F. Kling, F. Lepine, E. Benedetti, F. Ferrari, G. Sansone, and M. Nisoli. Attosecond electron spectroscopy using a novel interferometric pump-probe technique. *Physical Review Letters*, 105(5):053001, 2010.

[74] N. E. Karpowicz. *Physics and Utilization of Therahertz Gas Photonics*. PhD thesis, 2009.

[75] R. W. Boyd. *Nonlinear Optics, Third Edition*. Academic Press, MA, United States, 2008.

[76] W. Becker, F. Grasbon, R. Kopold, D. B. Milosevic, G. G. Paulus, and H. Walther. Above-threshold ionization: From classical features to quantum effects. *Advances in Atomic, Molecular, and Optical Physics, Vol 48*, 48:35–98, 2002.

[77] M. Protopapas, C. H. Keitel, and P. L. Knight. Atomic physics with super-high intensity lasers. *Reports on Progress in Physics*, 60(4):389–, 1997.

[78] T. Brabec and F. Krausz. Intense few-cycle laser fields: Frontiers of nonlinear optics. *Reviews of Modern Physics*, 72(2):545–591, 2000.

[79] P. Salieres and M. Lewenstein. Generation of ultrashort coherent xuv pulses by harmonic conversion of intense laser pulses in gases: towards attosecond pulses. *Measurement Science & Technology*, 12(11):1818–1827, 2001.

[80] Thomas Brabec. *Strong field laser physics*. Springer series in optical sciences,. Springer, New York, 2008.

[81] S. Haessler, J. Caillat, and P. Salieres. Self-probing of molecules with high harmonic generation. *Journal of Physics B-Atomic Molecular and Optical Physics*, 44(20), 2011.

[82] A. Mcpherson, G. Gibson, H. Jara, U. Johann, T. S. Luk, I. A. Mcintyre, K. Boyer, and C. K. Rhodes. Studies of multiphoton production of vacuum ultraviolet-radiation in the rare-gases. *Journal of the Optical Society of America B-Optical Physics*, 4(4):595–601, 1987.

[83] J. L. Krause, K. J. Schafer, and K. C. Kulander. High-order harmonic-generation from atoms and ions in the high-intensity regime. *Physical Review Letters*, 68(24):3535–3538, 1992.

[84] J. L. Krause, K. J. Schafer, and K. C. Kulander. Calculation of photoemission from atoms subject to intense laser fields. *Physical Review A*, 45(7):4998–5010, 1992.

[85] P. B. Corkum, N. H. Burnett, and F. Brunel. Above-threshold ionization in the long-wavelength limit. *Physical Review Letters*, 62(11):1259–1262, 1989.

[86] A. Lhuillier, M. Lewenstein, P. Salieres, P. Balcou, M. Y. Ivanov, J. Larsson, and C. G. Wahlstrom. High-order harmonic-generation cutoff. *Physical Review A*, 48(5):R3433–R3436, 1993.

[87] K. S. Budil, P. Salieres, A. Lhuillier, T. Ditmire, and M. D. Perry. Influence of ellipticity on harmonic-generation. *Physical Review A*, 48(5):R3437–R3440, 1993.

[88] P. Antoine, A. LHuillier, M. Lewenstein, P. Salieres, and B. Carre. Theory of high-order harmonic generation by an elliptically polarized laser field. *Physical Review A*, 53(3):1725–1745, 1996.

[89] N. H. Burnett, H. A. Baldis, M. C. Richardson, and G. D. Enright. Harmonic-generation in co2-laser target interaction. *Applied Physics Letters*, 31(3):172–174, 1977.

[90] R. L. Carman, D. W. Forslund, and J. M. Kindel. Visible harmonic emission as a way of measuring profile steepening. *Physical Review Letters*, 46(1):29–32, 1981.

[91] R. L. Carman, C. K. Rhodes, and R. F. Benjamin. Observation of harmonics in the visible and ultraviolet created in co2-laser-produced plasmas. *Physical Review A*, 24(5):2649–2663, 1981.

[92] B. Bezzerides, R. D. Jones, and D. W. Forslund. Plasma mechanism for ultraviolet harmonic radiation due to intense co2 light. *Physical Review Letters*, 49(3):202–205, 1982.

[93] S. Kohlweyer, G. D. Tsakiris, C. G. Wahlstrom, C. Tillman, and I. Mercer. Harmonic-generation from solid-vacuum interface irradiated at high laser intensities. *Optics Communications*, 117(5-6):431–438, 1995.

[94] E. Goulielmakis, M. Uiberacker, R. Kienberger, A. Baltuska, V. Yakovlev, A. Scrinzi, T. Westerwalbesloh, U. Kleineberg, U. Heinzmann, M. Drescher, and F. Krausz. Direct measurement of light waves. *Science*, 305(5688):1267–1269, 2004.

[95] K. C. Kulander and T. N. Rescigno. Effective potentials for time-dependent calculations of multiphoton processes in atoms. *Computer Physics Communications*, 63(1-3):523–528, 1991.

[96] H. G. Muller. An efficient propagation scheme for the time-dependent schrodinger equation in the velocity gauge. *Laser Physics*, 9(1):138–148, 1999.

[97] E. Runge and E. K. U. Gross. Density-functional theory for time-dependent systems. *Physical Review Letters*, 52(12):997–1000, 1984.

[98] C. Fiolhais, F. Nogueira, and Miguel A. L. Marques. *A primer in density functional theory*. Lecture notes in physics,. Springer, Berlin ; New York, 2003.

[99] Miguel A. L. Marques. *Time-dependent density functional theory*. Lecture notes in physics,. Springer, Berlin ; New York, 2006.

[100] N. Bloembergen. From nanosecond to femtosecond science. *Reviews of Modern Physics*, 71(2):S283–S287, 1999.

[101] E. P. Ippen, C. V. Shank, and A. Dienes. Passive mode-locking of cw dye laser. *Applied Physics Letters*, 21(8):348–350, 1972.

[102] C. V. Shank and E. P. Ippen. Subpicosecond kilowatt pulses from a mode-locked cw dye laser. *Applied Physics Letters*, 24(8):373–375, 1974.

[103] C. Froehly, B. Colombeau, and M. Vampouille. Shaping and analysis of picosecond light-pulses. *Progress in Optics*, 20:65–153, 1983.

[104] A. M. Weiner. Femtosecond optical pulse shaping and processing. *Progress in Quantum Electronics*, 19(3):161–237, 1995.

[105] A. M. Weiner. Femtosecond pulse shaping using spatial light modulators. *Review of Scientific Instruments*, 71(5):1929–1960, 2000.

[106] O. E. Martinez. 3000 times grating compressor with positive group-velocity dispersion - application to fiber compensation in 1.3-1.6 μm region. *IEEE Journal of Quantum Electronics*, 23(1):59–64, 1987.

[107] A. M. Weiner, J. P. Heritage, and E. M. Kirschner. High-resolution femtosecond pulse shaping. *Journal of the Optical Society of America B-Optical Physics*, 5(8):1563–1572, 1988.

[108] A. M. Weiner, D. E. Leaird, J. S. Patel, and J. R. Wullert. Programmable femtosecond pulse shaping by use of a multielement liquid-crystal phase modulator. *Optics Letters*, 15(6):326–328, 1990.

[109] A. M. Weiner, D. E. Leaird, J. S. Patel, and J. R. Wullert. Programmable shaping of femtosecond optical pulses by use of 128-element liquid-crystal phase modulator. *IEEE Journal of Quantum Electronics*, 28(4):908–920, 1992.

[110] M. M. Wefers and K. A. Nelson. Programmable phase and amplitude femtosecond pulse shaping. *Optics Letters*, 18(23):2032–2034, 1993.

[111] C. W. Hillegas, J. X. Tull, D. Goswami, D. Strickland, and W. S. Warren. Femtosecond laser-pulse shaping by use of microsecond radiofrequency pulses. *Optics Letters*, 19(10):737–739, 1994.

[112] P. Tournois. Acousto-optic programmable dispersive filter for adaptive compensation of group delay time dispersion in laser systems. *Optics Communications*, 140(4-6):245–249, 1997.

[113] F. Verluise, V. Laude, J. P. Huignard, P. Tournois, and A. Migus. Arbitrary dispersion control of ultrashort optical pulses with acoustic waves. *Journal of the Optical Society of America B-Optical Physics*, 17(1):138–145, 2000.

[114] F. Verluise, V. Laude, Z. Cheng, C. Spielmann, and P. Tournois. Amplitude and phase control of ultrashort pulses by use of an acousto-optic programmable dispersive filter: pulse compression and shaping. *Optics Letters*, 25(8):575–577, 2000.

[115] T. W. Hänsch. A proposed sub-femtosecond pulse synthesizer using separate phase-locked laser-oscillators. *Optics Communications*, 80(1):71–75, 1990.

[116] T. Mukai, R. Wynands, and T. W. Hänsch. Optical pulse synthesis with 3 cw semiconductor-lasers using nonlinear phase-locking. *Optics Communications*, 95(1-3):71–76, 1993.

[117] M. T. Hassan, A. Wirth, I. Grguras, A. Moulet, T. T. Luu, J. Gagnon, V. Pervak, and E. Goulielmakis. Invited article: Attosecond photonics: Synthesis and control of light transients. *Review of Scientific Instruments*, 83(11), 2012.

[118] A. Wirth. *Attosecond transient absorption spectroscopy*. PhD thesis, 2011.

[119] P. Tournois and D. Kaplan. Ultrafast pulse measurement device - wizzler.

[120] A. Moulet. *Attosecond nonlinear spectroscopy of core-shell excitations in atomic and solid state systems*. PhD thesis, 2015.

[121] D. J. Jones, S. A. Diddams, J. K. Ranka, A. Stentz, R. S. Windeler, J. L. Hall, and S. T. Cundiff. Carrier-envelope phase control of femtosecond mode-locked lasers and direct optical frequency synthesis. *Science*, 288(5466):635–639, 2000.

[122] Y. S. Lee, J. H. Sung, C. H. Nam, T. J. Yu, and K. H. Hong. Novel method for carrier-envelope-phase stabilization of femtosecond laser pulses. *Optics Express*, 13(8):2969–2976, 2005.

[123] J. H. Lee, Y. S. Lee, J. Park, T. J. Yu, and C. H. Nam. Long-term carrier-envelope-phase stabilization of a femtosecond laser by the direct locking method. *Optics Express*, 16(17):12624–12631, 2008.

[124] T. Fuji, J. Rauschenberger, A. Apolonski, V. S. Yakovlev, G. Tempea, T. Udem, C. Gohle, T. W. Hansch, W. Lehnert, M. Scherer, and F. Krausz. Monolithic carrier-envelope phase-stabilization scheme. *Optics Letters*, 30(3):332–334, 2005.

[125] F. Lucking, A. Assion, A. Apolonski, F. Krausz, and G. Steinmeyer. Long-term carrier-envelope-phase-stable few-cycle pulses by use of the feed-forward method. *Optics Letters*, 37(11):2076–2078, 2012.

[126] M. Schultze, A. Wirth, I. Grguras, M. Uiberacker, T. Uphues, A. J. Verhoef, J. Gagnon, M. Hofstetter, U. Kleineberg, E. Goulielmakis, and F. Krausz. State-of-the-art attosecond metrology. *Journal of Electron Spectroscopy and Related Phenomena*, 184(3-6):68–77, 2011.

[127] R. Szipocs, K. Ferencz, C. Spielmann, and F. Krausz. Chirped multilayer coatings for broad-band dispersion control in femtosecond lasers. *Optics Letters*, 19(3):201–203, 1994.

[128] M. Nisoli, S. DeSilvestri, O. Svelto, R. Szipocs, K. Ferencz, C. Spielmann, S. Sartania, and F. Krausz. Compression of high-energy laser pulses below 5 fs. *Optics Letters*, 22(8):522–524, 1997.

[129] S. Sartania, Z. Cheng, M. Lenzner, G. Tempea, C. Spielmann, F. Krausz, and K. Ferencz. Generation of o.1-tw 5-fs optical pulses at a 1-khz repetition rate. *Optics Letters*, 22(20):1562–1564, 1997.

[130] D. J. Kane and R. Trebino. Characterization of arbitrary femtosecond pulses using frequency-resolved optical gating. *IEEE Journal of Quantum Electronics*, 29(2):571–579, 1993.

[131] R. Trebino and D. J. Kane. Using phase retrieval to measure the intensity and phase of ultrashort pulses - frequency-resolved optical gating. *Journal of the Optical Society of America A-Optics Image Science and Vision*, 10(5):1101–1111, 1993.

[132] J. N. Sweetser, D. N. Fittinghoff, and R. Trebino. Transient-grating frequency-resolved optical gating. *Optics Letters*, 22(8):519–521, 1997.

[133] C. Iaconis and I. A. Walmsley. Spectral phase interferometry for direct electric-field reconstruction of ultrashort optical pulses. *Optics Letters*, 23(10):792–794, 1998.

[134] J. Itatani, F. Quere, G. L. Yudin, M. Y. Ivanov, F. Krausz, and P. B. Corkum. Attosecond streak camera. *Physical Review Letters*, 88(17), 2002.

[135] M. Kitzler, N. Milosevic, A. Scrinzi, F. Krausz, and T. Brabec. Quantum theory of attosecond xuv pulse measurement by laser dressed photoionization. *Physical Review Letters*, 88(17), 2002.

[136] Y. Mairesse and F. Quere. Frequency-resolved optical gating for complete reconstruction of attosecond bursts. *Physical Review A*, 71(1), 2005.

[137] D. J. Kane. Real-time measurement of ultrashort laser pulses using principal component generalized projections. *Ieee Journal of Selected Topics in Quantum Electronics*, 4(2):278–284, 1998.

[138] J. Gagnon, E. Goulielmakis, and V. S. Yakovlev. The accurate frog characterization of attosecond pulses from streaking measurements. *Applied Physics B-Lasers and Optics*, 92(1):25–32, 2008.

[139] M. Th. Hassan, T. T. Luu, A. Moulet, O. Raskazovskaya, P. Zhokhov, M. Garg, N. Karpowicz, A. M. Zheltikov, P. Pervak, F. Krausz, and E. Goulielmakis. Optical attosecond pulses. *Submitted*, 2014.

[140] A. Moulet, V. Tosa, and E. Goulielmakis. Coherent kiloelectronvolt x-rays generated by subcycle optical drivers: a feasibility study. *Optics Letters*, 39(21):6189–6192, 2014.

[141] Robert R. Alfano. *The supercontinuum laser source : fundamentals with updated references*. Springer, New York, 2nd edition, 2006.

[142] J. M. Dudley, G. Genty, and S. Coen. Supercontinuum generation in photonic crystal fiber. *Reviews of Modern Physics*, 78(4):1135–1184, 2006.

[143] A. Couairon and A. Mysyrowicz. Femtosecond filamentation in transparent media. *Physics Reports-Review Section of Physics Letters*, 441(2-4):47–189, 2007.

[144] J. Darginavicius, D. Majus, V. Jukna, N. Garejev, G. Valiulis, A. Couairon, and A. Dubietis. Ultrabroadband supercontinuum and third-harmonic generation in bulk solids with two optical-cycle carrier-envelope phase-stable pulses at 2 mu m. *Optics Express*, 21(21):25210–25220, 2013.

[145] B. P. Stoicheff. Characteristics of stimulated raman radiation generated by coherent light. *Physics Letters*, 7(3):186–188, 1963.

[146] F. Shimizu. Frequency broadening in liquids by a short light pulse. *Physical Review Letters*, 19(19):1097–, 1967.

[147] R. R. Alfano and S. L. Shapiro. Emission in region 4000 to 7000 a via 4-photon coupling in glass. *Physical Review Letters*, 24(11):584–, 1970.

[148] R. R. Alfano and S. L. Shapiro. Observation of self-phase modulation and small-scale filaments in crystals and glasses. *Physical Review Letters*, 24(11):592–, 1970.

[149] N. Bloembergen. The influence of electron plasma formation on superbroadening in light filaments. *Optics Communications*, 8(4):285 – 288, 1973.

[150] J. E. Rothenberg. Space-time focusing - breakdown of the slowly varying envelope approximation in the self-focusing of femtosecond pulses. *Optics Letters*, 17(19):1340–1342, 1992.

[151] W. Werncke, A. Lau, M. Pfeiffer, K. Lenz, H.-J. Weigmann, and C.D. Thuy. An anomalous frequency broadening in water. *Optics Communications*, 4(6):413 – 415, 1972.

[152] A. L. Gaeta. Catastrophic collapse of ultrashort pulses. *Physical Review Letters*, 84(16):3582–3585, 2000.

[153] A. Braun, G. Korn, X. Liu, D. Du, J. Squier, and G. Mourou. Self-channeling of high-peak-power femtosecond laser pulses in air. *Opt Lett*, 20(1):73–5, 1995.

[154] E. T. Nibbering, P. F. Curley, G. Grillon, B. S. Prade, M. A. Franco, F. Salin, and A. Mysyrowicz. Conical emission from self-guided femtosecond pulses in air. *Opt Lett*, 21(1):62–5, 1996.

[155] C. Lin and R. H. Stolen. New nanosecond continuum for excited-state spectroscopy. *Applied Physics Letters*, 28(4):216–218, 1976.

[156] R. L. Fork, C. H. B. Cruz, P. C. Becker, and C. V. Shank. Compression of optical pulses to 6 femtoseconds by using cubic phase compensation. *Optics Letters*, 12(7):483–485, 1987.

[157] A. Baltuska, Z. Y. Wei, M. S. Pshenichnikov, and D. A. Wiersma. Optical pulse compression to 5 fs at a 1-mhz repetition rate. *Optics Letters*, 22(2):102–104, 1997.

[158] M. Nisoli, S. DeSilvestri, and O. Svelto. Generation of high energy 10 fs pulses by a new pulse compression technique. *Applied Physics Letters*, 68(20):2793–2795, 1996.

[159] C. Vozzi, M. Nisoli, G. Sansone, S. Stagira, and S. De Silvestri. Optimal spectral broadening in hollow-fiber compressor systems. *Applied Physics B-Lasers and Optics*, 80(3):285–289, 2005.

[160] A. Suda, M. Hatayama, K. Nagasaka, and K. Midorikawa. Generation of sub-10-fs, 5-mj-optical pulses using a hollow fiber with a pressure gradient. *Applied Physics Letters*, 86(11), 2005.

[161] J. Park, J. H. Lee, and C. H. Nam. Generation of 1.5 cycle 0.3 tw laser pulses using a hollow-fiber pulse compressor. *Optics Letters*, 34(15):2342–2344, 2009.

[162] P. A. Franken, G. Weinreich, C. W. Peters, and A. E. Hill. Generation of optical harmonics. *Physical Review Letters*, 7(4):118–, 1961.

[163] R. W. Terhune, P. D. Maker, and C. M. Savage. Optical harmonic generation in calcite. *Physical Review Letters*, 8(10):404–, 1962.

[164] Y. A. Matveets, D. N. Nikogosyan, V. Kabelka, and A. Piskarskas. Efficient 2nd-harmonic generation in kdp crystal pumped by picosecond pulses of nd3+-yag laser with repetition rate of 0.5 pps. *Kvantovaya Elektronika*, 5(3):664–666, 1978.

[165] R. C. Eckardt and J. Reintjes. Phase matching limitations of high-efficiency 2nd harmonic-generation. *IEEE Journal of Quantum Electronics*, 20(10):1178–1187, 1984.

[166] M. S. Webb, D. Eimerl, and S. P. Velsko. Wavelength insensitive phase-matched 2nd-harmonic generation in partially deuterated kdp. *Journal of the Optical Society of America B-Optical Physics*, 9(7):1118–1127, 1992.

[167] X. Liu, L. J. Qian, and F. W. Wise. Efficient generation of 50-fs red pulses by frequency doubling in lib3o5. *Optics Communications*, 144(4-6):265–268, 1997.

[168] L. E. Nelson, S. B. Fleischer, G. Lenz, and E. P. Ippen. Efficient frequency doubling of a femtosecond fiber laser. *Optics Letters*, 21(21):1759–1761, 1996.

[169] H. Y. Zhu, T. Wang, W. G. Zheng, P. Yuan, L. J. Qian, and D. Y. Fan. Efficient second harmonic generation of femtosecond laser at 1 μm. *Optics Express*, 12(10):2150–2155, 2004.

[170] G. Szabo and Z. Bor. Broad-band frequency doubler for femtosecond pulses. *Applied Physics B-Photophysics and Laser Chemistry*, 50(1):51–54, 1990.

[171] O. E. Martinez. Achromatic phase matching for second harmonic generation of femtosecond pulses. *IEEE Journal of Quantum Electronics*, 25(12):2464–2468, 1989.

[172] B. A. Richman, S. E. Bisson, R. Trebino, E. Sidick, and A. Jacobson. Efficient broadband second-harmonic generation by dispersive achromatic nonlinear conversion using only prisms. *Optics Letters*, 23(7):497–499, 1998.

[173] S. Ashihara, T. Shimura, and K. Kuroda. Group-velocity matched second-harmonic generation in tilted quasi-phase-matched gratings. *Journal of the Optical Society of America B-Optical Physics*, 20(5):853–856, 2003.

[174] M. Brown. Increased spectral bandwidths in nonlinear conversion processes by use of multicrystal designs. *Optics Letters*, 23(20):1591–1593, 1998.

[175] P. Baum, S. Lochbrunner, and E. Riedle. Tunable sub-10-fs ultraviolet pulses generated by achromatic frequency doubling. *Optics Letters*, 29(14):1686–1688, 2004.

[176] E. T. J. Nibbering, O. Duhr, and G. Korn. Generation of intense tunable 20-fs pulses near 400 nm by use of a gas-filled hollow waveguide. *Optics Letters*, 22(17):1335–1337, 1997.

[177] T. Kanai, X. Y. Zhou, T. T. Liu, A. Kosuge, T. Sekikawa, and S. Watanabe. Generation of terawatt 10-fs blue pulses by compensation for pulse-front distortion in broadband frequency doubling. *Optics Letters*, 29(24):2929–2931, 2004.

[178] O. Razskazovskaya, T. T. Luu, M. K. Trubetskov, E. Goulielmakis, and V. Pervak. Nonlinear absorption in dielectric multilayers. *In preparation*, 2015.

[179] R. G. Flesch, A. Pushkarev, and J. V. Moloney. Carrier wave shocking of femtosecond optical pulses. *Physical Review Letters*, 76(14):2488–2491, 1996.

[180] L. Gilles, J. V. Moloney, and L. Vazquez. Electromagnetic shocks on the optical cycle of ultrashort pulses in triple-resonance lorentz dielectric media with subfemtosecond nonlinear electronic debye relaxation. *Physical Review E*, 60(1):1051–1059, 1999.

[181] A. V. Tarasishin, S. A. Magnitskii, and A. M. Zheltikov. Propagation and amplification of ultrashort light pulses in a resonant two-level medium: finite-difference time-domain analysis. *Optics Communications*, 193(1-6):187–196, 2001.

[182] J. A. Armstrong, N. Bloembergen, J. Ducuing, and P. S. Pershan. Interactions between light waves in a nonlinear dielectric. *Physical Review*, 127(6):1918–, 1962.

[183] Y. R. Shen. *The principles of nonlinear optics*. Wiley classics library. Wiley-Interscience, Hoboken, N.J., wiley classics library edition, 2003.

[184] T. Brabec and F. Krausz. Nonlinear optical pulse propagation in the single-cycle regime. *Physical Review Letters*, 78(17):3282–3285, 1997.

[185] M. A. Porras. Propagation of single-cycle pulsed light beams in dispersive media. *Physical Review A*, 60(6):5069–5073, 1999.

[186] P. Kinsler and G. H. C. New. Few-cycle pulse propagation. *Physical Review A*, 67(2), 2003.

[187] A. Couairon, E. Brambilla, T. Corti, D. Majus, O. D. Ramirez-Gongora, and M. Kolesik. Practitioner's guide to laser pulse propagation models and simulation. *European Physical Journal-Special Topics*, 199(1):5–76, 2011.

[188] M. Conforti, F. Baronio, and C. De Angelis. Modeling of ultrabroadband and single-cycle phenomena in anisotropic quadratic crystals. *Journal of the Optical Society of America B-Optical Physics*, 28(5):1231–1237, 2011.

[189] V. G. Dmitriev, G. G. Gurzadyan, and D. N. Nikogosyan. *Handbook of Nonlinear Optical Crystals, Third Edition*. Springer, Germany, 1999.

[190] H. R. Philipp. Optical transitions in crystalline and fused quartz. *Solid State Communications*, 4(1), 1966.

[191] M. Schlüter. Electron states in α-quartz: A self-consistent pseudopotential calculation. *Physical Review B*, 15(8):4029, 1977.

[192] E. K. Chang, M. Rohlfing, and S. G. Louie. Excitons and optical properties of alpha-quartz. *Physical Review Letters*, 85(12):2613–2616, 2000.

[193] C. B. Schaffer, A. Brodeur, and E. Mazur. Laser-induced breakdown and damage in bulk transparent materials induced by tightly focused femtosecond laser pulses. *Measurement Science & Technology*, 12(11):1784–1794, 2001.

[194] E. Constant, D. Garzella, P. Breger, E. Mevel, C. Dorrer, C. Le Blanc, F. Salin, and P. Agostini. Optimizing high harmonic generation in absorbing gases: Model and experiment. *Physical Review Letters*, 82(8):1668–1671, 1999.

[195] B. L. Henke, E. M. Gullikson, and J. C. Davis. X-ray interactions - photoabsorption, scattering, transmission and reflection at e=50-30,000 ev, z=1-92 (vol 54, pg 181, 1993). *Atomic Data and Nuclear Data Tables*, 55(2):349–349, 1993.

[196] T. T. Luu, M. Garg, S. Y. Kruchinin, A. Moulet, M. T. Hassan, and E. Goulielmakis. Extreme ultraviolet high-harmonic spectroscopy of solids. *Nature*, 521(7553):498–502, 2015.

[197] J. J. Macklin, J. D. Kmetec, and C. L. Gordon. High-order harmonic-generation using intense femtosecond pulses. *Physical Review Letters*, 70(6):766–769, 1993.

[198] S. G. Preston, A. Sanpera, M. Zepf, W. J. Blyth, C. G. Smith, J. S. Wark, M. H. Key, K. Burnett, M. Nakai, D. Neely, and A. A. Offenberger. High-order harmonics of 248.6-nm krf laser from helium and neon ions. *Physical Review A*, 53(1):R31–R34, 1996.

[199] D. Golde, T. Meier, and S. W. Koch. Microscopic analysis of extreme nonlinear optics in semiconductor nanostructures. *Journal of the Optical Society of America B-Optical Physics*, 23(12):2559–2565, 2006.

[200] K. S. Virk and J. E. Sipe. Semiconductor optics in length gauge: A general numerical approach. *Physical Review B*, 76(3), 2007.

[201] Felix Bloch. Über die quantenmechanik der elektronen in kristallgittern. *Zeitschrift für Physik*, 52:555–600, 1929.

[202] Clarence Zener. A theory of the electrical breakdown of solid dielectrics. *Proceedings of the Royal Society A*, 145:523–529, 1934.

[203] Hartmut Haug and S. W. Koch. *Quantum theory of the optical and electronic properties of semiconductors*. World Scientific, NJ, United States, 5th edition, 2009.

[204] Mackillo Kira and S. W. Koch. *Semiconductor quantum optics*. Cambridge University Press, Cambridge ; New York, 2012.

[205] T. Meier, G. Vonplessen, P. Thomas, and S. W. Koch. Coherent electric-field effects in semiconductors. *Physical Review Letters*, 73(6):902–905, 1994.

[206] Wilfried Schäfer and Martin Wegener. *Semiconductor optics and transport phenomena*. Advanced texts in physics,. Springer, Berlin ; New York, 2002.

[207] M. Wegener. *Extreme Nonlinear Optics*. Advanced Texts in Physics. Springer, 2005.

[208] T. Tritschler, O. D. Mucke, M. Wegener, U. Morgner, and F. X. Kartner. Evidence for third-harmonic generation in disguise of second-harmonic generation in extreme nonlinear optics. *Physical Review Letters*, 90(21):217404, 2003.

[209] S. Y. Kruchinin, M. Korbman, and V. S. Yakovlev. Theory of strong-field injection and control of photocurrent in dielectrics and wide band gap semiconductors. *Physical Review B*, 87(11), 2013.

[210] T. Otobe, M. Yamagiwa, J. I. Iwata, K. Yabana, T. Nakatsukasa, and G. F. Bertsch. First-principles electron dynamics simulation for optical breakdown of dielectrics under an intense laser field. *Physical Review B*, 77(16), 2008.

[211] K. Yabana, T. Sugiyama, Y. Shinohara, T. Otobe, and G. F. Bertsch. Time-dependent density functional theory for strong electromagnetic fields in crystalline solids. *Physical Review B*, 85(4), 2012.

[212] P. Blaha, K. Schwarz, G. Madsen, D. Kvasnicka, and J. Luitz. Wien2k, an augmented plane wave + local orbitals program for calculating crystal properties. *Karlheinz Schwarz, Techn. UniversitÃ¤t Wien, Austria*, 2001.

[213] M. Brandbyge, J. L. Mozos, P. Ordejon, J. Taylor, and K. Stokbro. Density-functional method for nonequilibrium electron transport. *Physical Review B*, 65(16), 2002.

[214] D. K. Ferry. Electron-transport at high fields in a-sio2. *Applied Physics Letters*, 27(12):689–690, 1975.

[215] G. Vampa, C. R. McDonald, G. Orlando, D. D. Klug, P. B. Corkum, and T. Brabec. Theoretical analysis of high-harmonic generation in solids. *Physical Review Letters*, 113(7), 2014.

[216] M. V. Fischetti, D. J. Dimaria, S. D. Brorson, T. N. Theis, and J. R. Kirtley. Theory of high-field electron-transport in silicon dioxide. *Physical Review B*, 31(12):8124–8142, 1985.

[217] E. Ciancio, R. C. Iotti, and F. Rossi. Gauge-invariant formulation of high-field transport in semiconductors. *Physical Review B*, 69(16), 2004.

[218] F. Rossi. *Theory of semiconductor quantum devices: microscopic modeling and simulation strategies*. Springer, 2011.

[219] M. Kruger, M. Schenk, and P. Hommelhoff. Attosecond control of electrons emitted from a nanoscale metal tip. *Nature*, 475(7354):78–81, 2011.

[220] A. Damascelli, Z. Hussain, and Z. X. Shen. Angle-resolved photoemission studies of the cuprate superconductors. *Reviews of Modern Physics*, 75(2):473–541, 2003.

[221] K. T. Kim, C. M. Zhang, A. D. Shiner, B. E. Schmidt, F. Legare, D. M. Villeneuve, and P. B. Corkum. Petahertz optical oscilloscope. *Nature Photonics*, 7(12):958–962, 2013.

[222] T. Brabec and F. Krausz. Intense few-cycle laser fields: Frontiers of nonlinear optics. *Reviews of Modern Physics*, 72(2):545–591, 2000.

[223] Edward D. Palik and Gorachand Ghosh. *Handbook of optical constants of solids*. Academic Press, San Diego, 1998.

[224] G. R. Harp, D. K. Saldin, and B. P. Tonner. Finite-size effects and short-range crystalline order in si and sio2 studied by x-ray absorption fine-structure spectroscopy. *Journal of Physics-Condensed Matter*, 5(31):5377–5388, 1993.

[225] D. Li, G. M. Bancroft, M. Kasrai, M. E. Fleet, R. A. Secco, X. H. Feng, K. H. Tan, and B. X. Yang. X-ray absorption spectroscopy of silicon dioxide (sio2) polymorphs - the structural characterization of opal. *American Mineralogist*, 79(7-8):622–632, 1994.

[226] C. A. Haworth, L. E. Chipperfield, J. S. Robinson, P. L. Knight, J. P. Marangos, and J. W. G. Tisch. Half-cycle cutoffs in harmonic spectra and robust carrier-envelope phase retrieval. *Nature Physics*, 3(1):52–57, 2007.

[227] Misha Ivanov and Olga Smirnova. Opportunities for sub-laser-cycle spectroscopy in condensed phase. *Chemical Physics*, 414(0):3–9, 2013.

[228] V. S. Yakovlev and A. Scrinzi. High harmonic imaging of few-cycle laser pulses. *Physical Review Letters*, 91(15), 2003.

[229] J. E. Midwinter and J. Warner. The effects of phase matching method and of uniaxial crystal symmetry on polar distribution of second-order non-linear optical polarization. *British Journal of Applied Physics*, 16(8):1135–, 1965.

[230] G. Arisholm. General numerical methods for simulating second-order nonlinear interactions in birefringent media. *Journal of the Optical Society of America B-Optical Physics*, 14(10):2543–2549, 1997.

[231] M. N. Polyanskiy. Refractive index database.

[232] D. Bauer and P. Koval. Qprop: A schrodinger-solver for intense laser-atom interaction. *Computer Physics Communications*, 174(5):396–421, 2006. 019HC Times Cited:66 Cited References Count:58.

[233] J. A. Fleck, J. R. Morris, and M. D. Feit. Time-dependent propagation of high-energy laser-beams through atmosphere. *Applied Physics*, 10(2):129–160, 1976.

[234] M. D. Feit, J. A. Fleck, and A. Steiger. Solution of the schrodinger-equation by a spectral method. *Journal of Computational Physics*, 47(3):412–433, 1982.

[235] N. Balakrishnan, C. Kalyanaraman, and N. Sathyamurthy. Time-dependent quantum mechanical approach to reactive scattering and related processes. *Physics Reports-Review Section of Physics Letters*, 280(2):79–144, 1997. Wz003 Times Cited:194 Cited References Count:417.

[236] J. J. Sakurai and San Fu Tuan. *Modern quantum mechanics*. Addison-Wesley Pub. Co., Reading, Mass., rev. edition, 1994.

[237] Karl Blum. *Density matrix theory and applications*. Physics of atoms and molecules. Plenum Press, New York, 2nd edition, 1996.

[238] A. Kramida, Yu. Ralchenko, J. Reader, and and NIST ASD Team. NIST Atomic Spectra Database (ver. 5.1), [Online]. Available: `http://physics.nist.gov/asd` [2014, September 15]. National Institute of Standards and Technology, Gaithersburg, MD., 2013.

[239] S. Chang and V. Minogin. Density-matrix approach to dynamics of multilevel atoms in laser fields. *Physics Reports-Review Section of Physics Letters*, 365(2):65–143, 2002.

[240] S. Mukamel. *Principles of nonlinear optical spectroscopy*. Oxford series in optical and imaging sciences. Oxford University Press, New York, 1995.

Acknowledgements

PhD is a long journey, a significant part of life that each PhD holder would never forget. Certainly a PhD work in a modern society cannot be accomplished without the support from various people and mine is not an exception.

It was a great pleasure for me having an opportunity working here in an excellent team with extraordinary infrastructure at Laboratory for Attosecond Physics, Max Planck Institute of Quantum Optics. I would like to express my gratitude to Prof. Ferenc Krausz for providing me this unique chance building my professional career here.

Most importantly I am deeply grateful to Dr. Eleftherios Goulielmakis who is my advisor during these years in the Attoelectronics group. I have been in a great training and received invaluable advices from his extraordinary experimental skills as well as intuitively physical insights. I have received also constant support and encouragement from him throughout these years.

Accompanying with me through these exact four years is Antoine Moulet who is very smart, has a solid background in many branches of science. I benefited a lot from our discussions and I am sure that no matter what he is going to do in the future, he will do it very well.

I would like to thank Manish Garg who is never laugh at my stupid questions in quantum chemistry but always be patient enough to explain things. He supported me a lot during my last works and the 4^{th} chapter would not be in the current form without him. I want to thank also Mohammed Hassan who spent almost three years with me. Together we have built nice experimental setups, performed beautiful experiments, various simulations and analyses. We had a lot of joy and we will have a lot of joy in the near future, I believe.

Adrian Wirth, Julien Bertrand, Arohi Jain, Minjie Zhan, Harshit Lakhotia, Till Klostermann, Giovanni Resta, Hee-Yong Kim, and Jonathan Liu are my former and current colleagues. They all supported me in one way or the other during they stay here. Thank you for your kindness, sharing and all the fun we shared.

I am glad to have nice friends from other groups inside the LAP and on this occasion, I would like to thank Olga Razskazovskaya, Alexander Schwarz, Christoph Schrobol, Wolfgang Schweinberger, Sabine Keiber, Nicholas Karpowicz, Hanieh Fattahi, Michael Jobst, Matthias Kubel, Alexander Kessel, Elisabeth Bothschafter, Annkatrin Sommer, Vladimir Pervak, Laszlo Veisz, Martin Schultze, Clemens Jakubeit, Soo Hoon Chew, and Christian Spaeth. Thank you for your great support and being awesome. I also would like to thank Prof. Matthias Kling for occasional discussions and encouragement.

Theory team in LAP has supported me a lot in learning the theoretical concepts as well as building some simulations. I am grateful to Stanislav Kruchinin, Vladislav Yakovlev, Justin Gagnon, Michael Wismer, and Marcelo Ciappina.

A big part of my PhD funding comes from the European project - Marie Currie actions - Initial Training Network (ITN). It was a great honor for me to be part of this outstanding project and to have chances meeting excellent researchers in the field. I would like to thank Prof. Marc Vrakking, Dr. Thomas Schultz for their excellent organization and great support as well as the other ATTOFEL members: Christoph Heyl, Faruk Krecinic, Fabian Lueking, Piotr Rudawski and others. Furthermore, I am grateful to Prof. Anne L'Huillier for providing me an opportunity to perform a 2 week secondment in her group. Many thanks go to Dr. Cord Arnold, Miguel Miranda, Marija Kotur, Anne Harth, Esben Witting Larsen, and Maite Louisy for your help and the nice cultural sharing.

During my PhD years, I have applied and successfully received a scholarship from DAAD (German Academic Exchange Service) within the framework of RISE (Research Internships in Science and Engineering). I would like to thank DAAD for this scholarship, because of that we have an excellent internship student Alexandre Gauthier from University of Pittsburgh who came and supported our projects.

Last but not least, I would like to thank Frau Wild and people from the Einkauf, the technician team, the IT team as well as the machineshop team, especially to Carina Steinkrebs, Michael Bojus, Harald Haas, Alois Boeswald, Manfred Grote, Wolfgang Huber, Michael Rogg, and Thomas Strobl. They have made my life here a lot easier.

Tran Trung Luu

Curriculum Vitae

Personal information

Born:	February 16, 1986	Nationality: Vietnamese
Status:	Married, one child	
Language:	Vietnamese (native), English (fluent)	

Contact address:
Kraepelinstr. 63
D-80804 Munich
GERMANY

Phone: (+49) (0)89/32905-718
(+49) (0)176/64877938
Email: tran.trung.luu@mpq.mpg.de
trunghoa.fa@gmail.com

Research Experience / Education

Ph.D. in exp. physics — Oct 2010 - Apr 2015
Ph.D. advisor: Dr. E. Goulielmakis — MPI of Quantum Optics / LMU Munich, Germany
Dissertation: *Extreme ultraviolet high harmonic generation and spectroscopy in solids*

Post-master research — Mar 2010 - Sep 2010
Coherent X-ray Research Center — Korea Advanced Institute of Science and Technology, South Korea
Topic: *Optimization of femtosecond lasers*

M.A. (thesis) in Physics — Feb 2008 - Feb 2010
Advisor: Prof. Dr. C. H. Nam — Korea Advanced Institute of Science and Technology, South Korea
Thesis: *Real time characterization of femtosecond laser pulses by spectral phase interferometry for direct electric field reconstruction*

Bachelor in Physics — 2003 - 2007
Department of Physics — College of Science, Vietnam National Univeristy, Hanoi, Vietnam
Thesis: *Time resolved luminescence measurement of samples pumped by Nitrogen laser*

Honors and Awards (selected)

DAAD — 2013
German Academic Exchange Service — Germany
German Academic Exchange Service - Research in Science and Technology

Marie Currie Fellowship — 2011 - 2013
European Research Council — Germany
Initial Training Network research fellow

KAIST Master fellowship — 2008 - 2010
Korea Advanced Institute of Science and Technology — South Korea

Scientific conference 2007
Vietnam National University, Hanoi Vietnam
First prize - Excellent results in research

Physics Olympiad 2002 - 2005
Vietnam Minister of Education and Training Vietnam
First prize - student 2005, third prize - student 2004, third prize - high school pupil 2002

Publications

5 peer-reviewed publications and 3 contributed talks in international journals and conferences